

THEORETICAL AND EXPERIMENTAL STUDIES OF THE
2-DIMENSIONAL GRATING COUPLED STRUCTURES FOR
III-V QUANTUM WELL INFRARED PHOTODETECTORS

BY

YEONG-CHENG WANG

A DISSERTATION PRESENTED TO THE GRADUATE SCHOOL
OF THE UNIVERSITY OF FLORIDA IN
PARTIAL FULFILLMENT OF THE REQUIREMENTS
FOR THE DEGREE OF DOCTOR OF PHILOSOPHY

UNIVERSITY OF FLORIDA

1994

ACKNOWLEDGEMENTS

I would like to express my sincere gratitude to my advisor and the chairman of my committee, Professor Sheng S. Li, who gave me an opportunity to work as one of his graduate students. This research was completed under his guidance, encouragement, and support. I also wish to thank Professors Dorothea E. Burk, Gÿs Bosman, William R. Eisenstadt, and Chen-Chi Hsu for serving on my supervisory committee.

Thanks are extended to Dr. Larry S. Yu of National Semiconductor Corp. and Dr. Ping-Chang Yang of Fan-Chia University for their valuable discussions, Yenhwa Wang for his great help in semiconductor processing, and my friends Jung-chi Chiang, Chih-Hung Wu, Ming-Yeh Chuang, Daniel Wang, Zhiliang Chen and Yun-Shun Chang for their friendship.

I am greatly indebted to my wife and parents for their love, support, and encouragement during the arduous procedure of completing my Doctor of Philosophy degree.

Finally, the financial support of the Defense Advanced Research Project Agency (DARPA) is gratefully acknowledge.

TABLE OF CONTENTS

	Page
ACKNOWLEDGEMENTS	ii
ABSTRACT	vi
CHAPTER	
1 INTRODUCTION	1
1.1 Quantum Well Detectors	1
1.2 Quantum Well Intersubband Absorption	2
1.3 Grating Coupler	3
1.4 Synopsis of Chapters	6
2 A NUMERICAL ANALYSIS OF REFLECTION SQUARE DOT METAL GRATING FOR MULTIQUANTUM WELL INFRARED PHOTODETECTORS	19
2.1 Introduction	19
2.2 The Theoretical Formalism	21
2.3 Results and Discussion	24
2.4 Conclusion	28
3 DESIGN OF A TWO-DIMENSIONAL SQUARE APERTURE MESH METAL GRATING COUPLER FOR A MINIBAND TRANSPORT GaAs QUANTUM WELL INFRARED PHOTODETECTOR	37
3.1 Introduction	37
3.2 Basic Theory	39
3.3 Results and Discussion	43
3.4 Conclusion	46
4 GEOMETRY CONSIDERATIONS OF TWO-DIMENSIONAL GRATING COUPLER FOR GaAs QUANTUM WELL	

	INFRARED PHOTODETECTOR	55
	4.1 Introduction	55
	4.2 Theory and Illumination	57
	4.3 Conclusion	60
5	EXPERIMENTAL IMPLEMENTATIONS OF TWO DIMENSIONAL SQUARE APERTURE MESH METAL GRATING COUPLER	67
	5.1 Introduction	67
	5.2 Sample Preparation	68
	5.3 Grating Fabrication	69
	5.4 Theory	70
	5.5 Optical Measurement	71
	5.6 Results and Discussion	72
	5.7 Conclusion	74
6	DESIGN OF PLANAR 2-D CIRCULAR APERTURE METAL GRATING COUPLER FOR GaAs QUANTUM WELL INFRARED PHOTODETECTORS	78
	6.1 Introduction	78
	6.2 Basic Theory	80
	6.3 Results and Discussion	83
	6.3.1 Square Symmetry Grating Structure	83
	6.3.2 Hexagonal Symmetry Grating Structure	84
	6.3.3 Comparison between Experiment and Theory	85
	6.4 Conclusion	86
7	DESIGN OF AN OPTIMUM PERFORMANCE BTM QWIP	96
	7.1 Introduction	96
	7.2 General Consideration of a BTM QWIP	97
	7.2.1 Barrier Height and $\text{Al}_x\text{Ga}_{1-x}\text{As}$ Composition	98
	7.2.2 Superlattice Barrier Width	98
	7.2.3 Doping Concentration in the Quantum Well	99
	7.3 Quantum Well Period	99
	7.4 Blocking Barrier and Dark Current	102
	7.5 Waveguide Structure	103
	7.6 Conclusion	107

8	SUMMARY	117
	REFERENCES	119
	APPENDIX	128
	BIOGRAPHICAL SKETCH	130

Abstract of Dissertation Presented to the Graduate School
of the University of Florida in Partial Fulfillment of the
Requirements for the Degree of Doctor of Philosophy

THEORETICAL AND EXPERIMENTAL STUDIES OF THE
2-DIMENSIONAL GRATING COUPLED STRUCTURES FOR
III-V QUANTUM WELL INFRARED PHOTODETECTORS

By

Yeong-Cheng Wang

April 1994

Chairman: Sheng S. Li
Major Department: Electrical Engineering

This research mainly deals with the quantum efficiency enhancement of QWIPs (Quantum Well Infrared Photodetectors) by using the 2-dimensional (2-D) planar metal grating couplers. The motivation is originated from the intersubband selection rule of quantum well, which requires the polarization of incident infrared (IR) radiation to have a component perpendicular to the quantum well layers. The unique features of the 2-D planar metal grating coupler are that (a) it effectively scatters the normal incident radiation independent of light polarization and (b) it can be easily fabricated by using a simple metal lift-off technique. Three grating structures are developed to couple the normal incident IR light into the QWIPs. The first grating structure is the 2-D square dot reflection metal grating with a coupling efficiency of 20%. The coupling efficiency can be increased by employing its complementary geometry, the 2-D square aperture mesh metal grating. About 70% of the normal incident light is diffracted into TM waves available for QWIP absorption. To solve the corner

rounding effect observed in the square shape grating, a 2-D circular aperture metal grating coupler is developed, which has the same coupling efficiency of 70% and with a efficiency of 2.7 times higher than that of the 45° polished edge QWIP with corresponding quantum well parameters. In addition to the square symmetry arrangement required in the three grating designs, one more benefit from the hexagonal symmetry circular aperture grating is a wider coupling bandwidth. For each grating structure, several universal plots based on two normalized parameters λ/g and a/g were presented, where λ is the wavelength, g is the grating period, and a is the dimension of grating shape. The universal plots provide a convenient way for grating design.

Modal expansion and method of moments are two basic approaches used in the numerical analysis of grating couplers. The diffracted angle and diffracted power are drawn in universal plots, the diffracted angle determines the absorption constant, combining with the diffracted power the spectral quantum efficiency of QWIP can be calculated.

In addition to coupling enhancement by grating, the waveguide geometry QWIP shows a further improvement in IR absorption. The design of QWIP waveguide is carried out numerically. Together with the optimum period of multiquantum wells and the blocking layers to reduce the dark current, a high performance QWIP is proposed.

CHAPTER 1 INTRODUCTION

1.1 Quantum Well Detectors

There is a great need for high resolution, high sensitivity focal plane array detectors in the long wavelength infrared spectrum of the 8-14 μm atmospheric window for both the military and civilian regimes. The most widely used infrared detector materials are intrinsic Si and HgCdTe (MCT). Even with the rapid growth of the silicon-based new technologies and microelectronics industry, it is generally recognized that for long wavelength infrared detector applications III-V compound semiconductors are superior to Si [1]. This is due to different material properties, such as a wide range of available bandgaps, the direct bandgaps that facilitates efficient conversion from light to electricity, and carriers with very high mobility. The difficulties in materials growth, processing, and other details of these technologies of HgCdTe material have made it highly desirable to examine whether performance can be improved by other material systems [2]. Since the material and device technologies in III-V compound semiconductors are far more advanced than HgCdTe, it is natural to investigate these III-V compounds for possible applications in long wavelength infrared detection. Recently, III-V quantum well/superlattice structures have been used to construct long wavelength infrared photodetectors [3]. The quantum well is formed by using a layer of a narrow bandgap semiconductor (such as GaAs) sandwiched between two wider bandgap semiconductor layers (such $\text{Al}_x\text{Ga}_{1-x}\text{As}$). The motion of the electron perpendicular to the layers becomes quantized so that localized (in the direction transverse to the layers) two-dimensional (2-D) subbands of size-quantized states were formed inside the quantum well [4-6].

These multi-quantum well structures are usually grown by molecular beam epitaxy (MBE) technique, which allows the exact adjustment of the most important device parameters. By changing the well width and barrier height, detectors can be designed with response peaks from the mid- to the far- infrared wavelength regions. According to the electrons transport approaches, two fundamental structures of quantum well infrared photodetectors (QWIPs) are illustrated in Fig. 1.1. For the bound-to-continuous (BTC) QWIPs (Fig. 1(a)), the electrons photoexcited from the bound ground state by infrared (IR) radiation are transported through the extended continuum band above the barrier under an applied electric field [7], while for a bound-to-miniband (BTM) QWIP, as shown in Fig. 1(b), these electrons are transported through a global miniband formed by superlattice barriers.

1.2 Quantum Well Intersubband Absorption

The absorption in a QWIP is based on intersubband transition of n-type doped quantum well heterostructures. Upon illumination of IR radiation, electrons are excited from the ground state into the excited state [8]. Only in the excited state, electrons moving in the direction perpendicular to quantum wells becomes possible, which produce the electric signal under an applied electric field. Therefore, the basic operation of QWIPs is photoconductive type, and the schematic diagram of a detector pixel is shown in Figure 1.2. Careful optical design is needed since one of the major problems encountered in type-I (n-doped) QWIPs is that the polarization selection rule for intersubband transition requires one component of the electric field vector of the IR radiation to be polarized perpendicular to the quantum well layer planes [9-11]. This results in the detectors have no photo-response for radiation incident in the direction normal to the quantum well layers. For focal plane arrays (FPAs) applications, as shown in Fig. 1.3, a response to normal incident radiation is requisite. For this reason, special schemes of coupling to convert the transverse electromagnetic wave into a direction suitable for absorption are necessary. A variety of techniques

have been employed, such as a 45° angle polished facet in substrate of the detector sample as shown in Fig. 1.4(a), the illumination at Brewster's angle orientation (Fig. 1.4(b)), a prism coupler [12] in the detector surface (Fig. 1.4(c)), a lamellar grating coupler (Fig. 1.5(a)), and a double periodic metal grating on the detector surface (Figs. 1.5(b), (c)). The coupling of the incident intensity to the intersubband transitions is too weak to be used for sample oriented at Brewster's angle or coupled by prism. The light coupling through a 45° polished facet only allows incident light to access one edge of the detector, which is possible to form only one-dimensional (1-D) linear arrays. For imaging application in FPAs, it is necessary to couple light uniformly into the 2-D arrays of such detectors. A 1-D linear grating either by depositing metal lines onto the detector surface (Figs. 1.2 and 1.5(a)) or by chemical etching the detector surface into periodic profile (Fig. 1.6(a)) or followed by metal deposition (Fig. 1.6(b)) are potentially applicable to the fabrication of 2-D detector arrays. However, these approaches are polarization dependent, only couple transverse magnetic (TM) component of the incident light. To solve this, a double periodic cross grating coupler is used to effectively couple the normal incident IR radiation into the doped wells independent of light polarization.

The detector array consists of pixels of QWIPs arranged periodically on the detector substrate. To allow normal incidence illumination, the grating can be fabricated either on the substrate side (Fig. 1.7(a)) or on the top surface (Fig. 1.7(b)) of the detectors. It is worthy of noting that the latter has the advantage over the former in that it eliminates the undesirable pixel cross talk as shown in Fig. 1.7.

1.3 Grating Coupler

The above discussions suggest that diffraction grating is an effective optical coupling means for fabricating large area n-type QWIP arrays. This has been demonstrated in the early work [13,14] of intersubband resonances in electron inversion layer

of silicon. Goossen *et al.* [15-17] first employed the grating to couple a single quantum well and gave a brief grating analysis. Then, Hasnain *et al.* [18] used a etched triangular grating, Yu and Li [19,20] used a laminal metal grating, on QWIP cap layer to further study the grating coupling in multi-quantum wells. Hasnain obtained a coupling efficiency about 50% to that of the 45° edge detectors. Planar 1-D metal stripe gratings were first studied by Li *et al.* [21,22], who used a grating period approximately equal to that of the peak absorption wavelength in the detector medium for many layer QWIP. This type of grating is relatively simple in fabrication. Applying the metal gratings for light coupling based on the excitation and emission of surface plasmons to achieve high responsivity has been done by Köck *et al.* [23]. In this coupling mechanism, the detector polished backside was etched into a slot profile followed by a 250 Å gold film coating. The surface plasmons are excited at the Au-air interface and leak through the Au film to radiate into the doped quantum in several angles. In addition to these single period grating, a wider coupling bandwidth have been demonstrated by Lee *et al.* [11] by a bi-periodic grating arrangement.

In the study of 2-D grating, Andersson and Lundqvist [24-27] presented a detailed analysis and measurements on such a grating coupled QWIP. The calculated optimum period, cavity shape as well as the etching depth is only applicable in their special designed BTC QWIP. They found that for the 50 period QWIP with peak absorption wavelength at 9.5 μm an optimum grating consists of a 3 μm period, $\sim 2\mu\text{m}$ square cavity width and a 1 μm etching depth, which allows about 55% quantum efficiency for unpolarized incident radiation. Although several complicated equations were given, the grating coupling characteristics of their grating coupler have never been mentioned. Recently Levine [28] employed a random roughened reflecting surface to achieve a significant higher coupling by utilizing many more passes of infrared light through the detector active region. This idea is originated from the total internal reflection of light trapping on crystalline silicon by Yablonovitch and Cody [29]

based on a statistical mechanical view point.

In this dissertation we mainly deal with 2-D planar metal grating for QWIPs. The individual cells are equally spaced in the square symmetrically arranged grating. According to its operation, the 2-D square symmetry metal grating is categorized into two regions. The function of the grating is a qualitatively different one above and below $\lambda = g$. In the non-diffraction region, light wavelength ' λ ' is greater than grating period ' g ', the grating acts as a optical filter and waves propagate only in the incident and reflected directions, which are the zeroth order transmitted waves and zeroth order reflected waves, respectively (Fig. 1.8(a)). All energy that is not transmitted by the grating is reflected back. In the diffraction region, light wavelength ' λ ' is smaller than grating period ' g ' and the grating acts as scatters filters. In this wavelength region, part of the energy may be diffracted into various directions of space which is either the higher order transmitted waves or higher order reflected waves with propagating directions depending on λ as shown in Fig. 1.8 (b) and (c). For the application of grating on QWIPs, it is necessary to deflect normal incident IR radiation into a non-zero angle with respect to grating normal in order to match the absorption selection rule. Of course, the effective components for absorption are the higher order diffracted waves. The grating diffracted waves consist of transverse electric (TE) modes with electric field vector parallel to the quantum well layer planes as shown in Fig. 1.9 (a), and TM modes with one component of the electric field vector perpendicular to the quantum well layers as shown in Fig. 1.9 (b). Only TM modes obey the rule of intersubband transition and cause photo-signal. Two factors determine the strength of power absorption: (i) cosine of the angle ' γ ' enclosed by electric field vector of IR radiation and the motion vector of excited electrons, (ii) the power density of effective diffracted waves. It is preferable to design the 2-D metal grating for generating the higher order diffracted waves not only to travel in a large $\cos \gamma$ but also to carry a large amount of power.

The modeling of grating will be restricted to thin conducting screen, which implies the thickness of grating is much smaller than light wavelength ' λ '. The first step used is modal expansion, which expands the unknown electromagnetic (EM) waves near the grating by a complete set of plane waves. It is also a near-exact approach for calculating wave diffraction problem, which considers the vector characteristics of the electromagnetic field. Next, method of moments [30] is employed to reduce the functional equation of field theory to matrix equation. Truncation of expanding series is made carefully by examining the convergence of solution. These techniques offer a highly efficient approach for solving the grating diffraction problem provided the grating has special pixel profiles, e.g., rectangular or circular shape. With these shapes, an analytic expression of vector function inner products can be obtained by hand calculation.

1.4 Synopsis of Chapters

This dissertation contains eight chapters. Chapter 1 describes the problem we are studying and reviews ongoing work in this research. Chapter 2 discusses 2-D reflection square dot metal grating. Two normalized parameters (i.e., $s = \lambda/g$ and $h = a/g$, where g is the grating period and a is width of the square dot) are introduced to characterize the 2-D reflection metal grating coupler for QWIPs. The main advantage for such a grating structure is that the coupling of the normal incident IR radiation is independent of its polarization direction. Two universal graphs relating the higher order diffracted power and absorption angle to the normalized wavelength have been constructed for the design of 2-D reflection metal grating coupled QWIPs, which give a convenient overview of the grating characteristics and various design possibilities. By using a simple scaling rule, the characteristic curve of coupling and subsequent absorption spectrum was calculated.

Chapter 3 presents a detail discussion of 2-D square aperture mesh metal grating. Numerical analysis of a 2-D square aperture mesh metal grating coupled BTM

GaAs/AlGaAs QWIP has been carried out. The main advantages of this grating structure include (1) High coupling quantum efficiency in the quantum well absorption spectrum, and (2) coupling of normal incident IR radiation into the quantum wells is independent of light polarization. Two normalized parameters s and h (i.e., $s = \lambda/g$ and $h = a/g$, where a is the width of the aperture in the grating) are used in the simulation of the 2-D metal grating structure formed on GaAs BTM QWIPs. Using two universal plots displaying the total power and absorption angle of the higher order transmission and reflection diffracted waves, the optical absorption constant and coupling quantum efficiency of IR radiation can be calculated for different grating periods and aperture sizes in any wavelength range.

Chapter 4 studies the problems of aperture distortion observed in the grating fabrication. The effects of aperture size and shape variation on photoresponse of a 2-D square mesh metal grating coupler for a GaAs/AlGaAs QWIP has been analyzed. The grating pattern consists of tiny square dot distributed on the detector mesa. During the process of grating pattern photolithography, some distortion in the aperture's size and shape may occur by the use of contact-type mask aligner. This may lead to cell-to-cell nonuniformity in photo-response for QWIP arrays applications. The effect can be reduced by either selecting a relatively stable aperture size or using a larger grating period.

The experiment results of grating coupling were compared to theoretical calculations in Chapter 5. A study of the quantum efficiency and responsivity in a GaAs step-BTM QWIP enhanced by the planar 2-D square aperture mesh metal grating has been carried out. Different coupling schemes and grating parameters were included. The responsivity of grating coupled QWIP under back side normal incident illumination is 1.65 times higher than that under front side. A maximum responsivity of $R_I = 0.5$ A/W was obtained at peak response wavelength $\lambda_p = 10.4\mu\text{m}$ by employing a grating period, $g = 3.3\mu\text{m}$ and aperture width, $a = 2\mu\text{m}$ under substrate side normal incident

illumination. The ignoring of current loss on the metal grating surface results in a larger calculated quantum efficiency (32%) than that of the measured (29%). Combining the measured results of front side and back side illumination suggests a strong reflection occurring at the substrate-air interface after coating the metal grating on top of QWIP.

The coupling of 2-D circular aperture mesh metal grating coupler and intersubband absorption of $10\mu\text{m}$ GaAs BTC QWIP were demonstrated in Chapter 6. The inner products of Floquet modes and waveguide modes were derived in a simple analytic form. Employing normalized wavelength and normalized aperture radius, two sets of universal charts were drawn for elucidating the normalized total power and absorption angle of the higher-order TM diffracted waves of the grating. By the use of simple scaling rules, the optimum grating design for GaAs QWIP can be determined. The measured results show a 2.7 times enhancement on current responsivity at $\lambda_p = 10\mu\text{m}$ for grating coupled detector over that of a 45° angle edge detector. A further enhancement can be expected for an optimum grating coupled QWIP.

Chapter 7 develops a standard procedure for QWIP design. Analysis of the quantum well detector parameters for achieving the optimum performance in a BTM QWIP was made. The reduction of dark current is achieved by two simultaneous approaches; a larger barrier height and a selective blocking layer. To increase intersubband absorption in the quantum wells, a $4\mu\text{m}$ AlAs cladding layer beneath the detector active region is employed to form a waveguide geometry QWIP. This waveguide coupling scheme further enhances the QWIP absorption due to multi-pass of IR radiation along the wave propagating direction. The combination of $1.2\mu\text{m}$ cap layer and $0.5\mu\text{m}$ bottom GaAs contact layer ensures the maximum field intensity occurs in the QWIP active region. The optimum period for QWIPs waveguide deduced from the experimental study of step-BTM QWIPs was found to be 18λ . Finally, a summary of this research is given in Chapter 8.

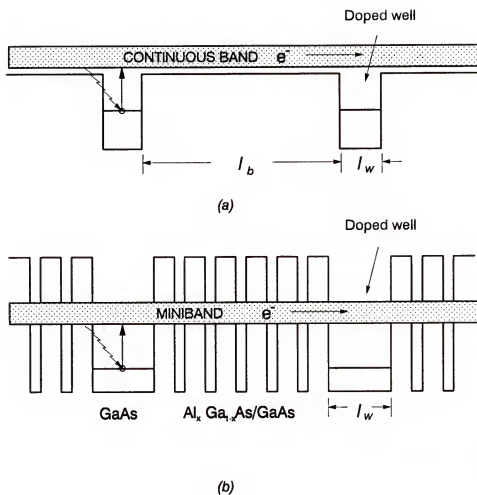


Figure 1.1 Conduction band diagram for (a) bound-to-continuous transport QWIPs, (b) bound-to-miniband transport QWIPs.

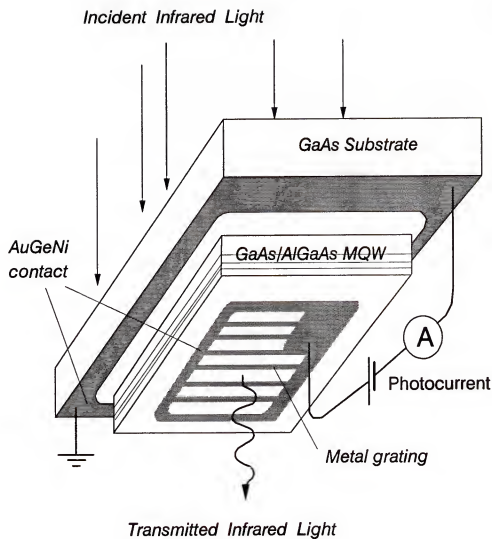


Figure 1.2 Schematic representation of a single detector cell.

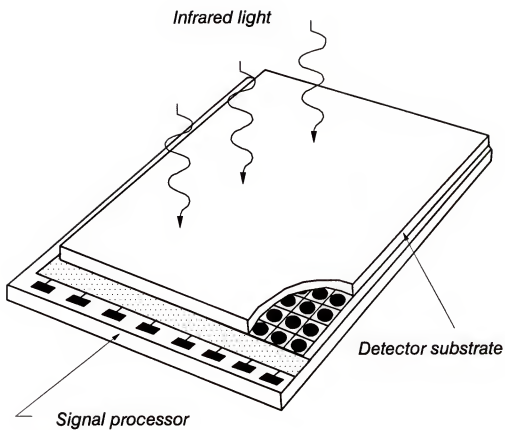


Figure 1.3 The architecture of a focal plane arrays.

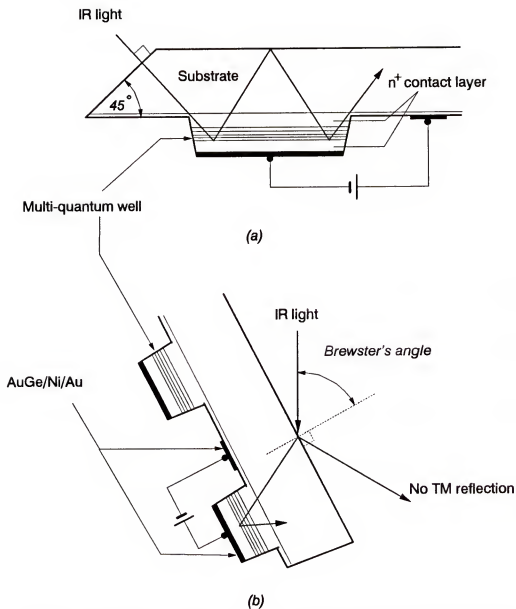


Figure 1.4 (a) Light coupling of QWIP through a 45° angle polished facet on one edge of the detector sample. (b) Brewster's angle illumination of the QWIPs.

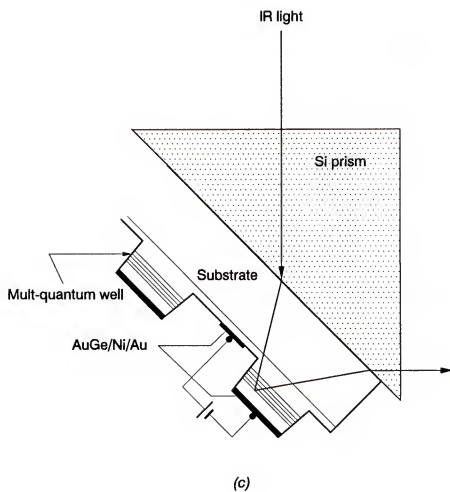


Figure 1.4(c) The scheme of the prism coupled quantum well infrared photodetectors

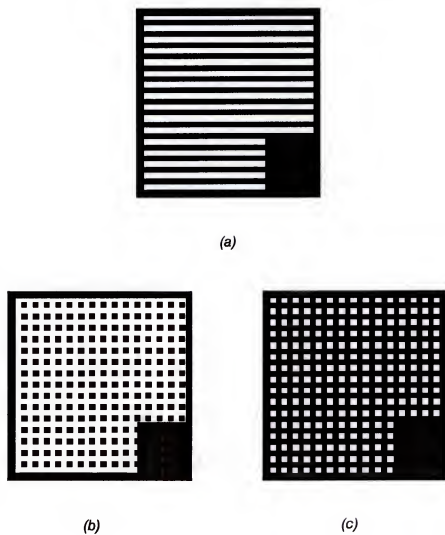


Figure 1.5 Three basic structures of planar metal grating. (a) 1-D strip metal grating, (b) square dot reflection metal grating, and (c) square aperture mesh metal grating, where the dark areas represent metal.

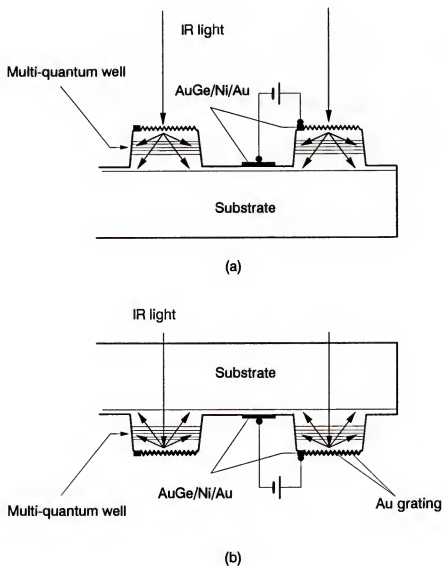


Figure 1.6 Side view of the detectors showing the scheme for illumination in normal incidence through (a) an etched top contact layer without metal deposition, (b) the substrate and then reflected by the etch-formed metal grating.

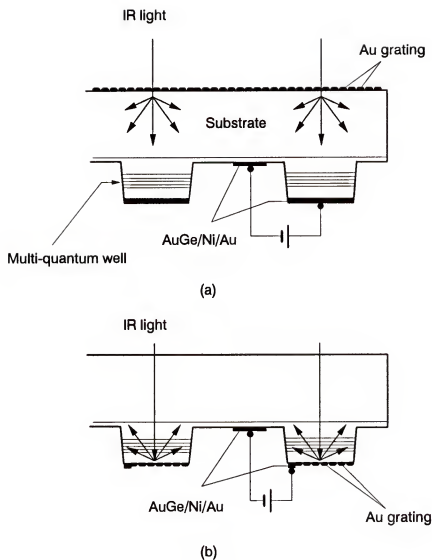


Figure 1.7 The metal grating formed on (a) substrate, (b) top contact layer of the quantum well detectors. The latter avoids the optical crosstalk.

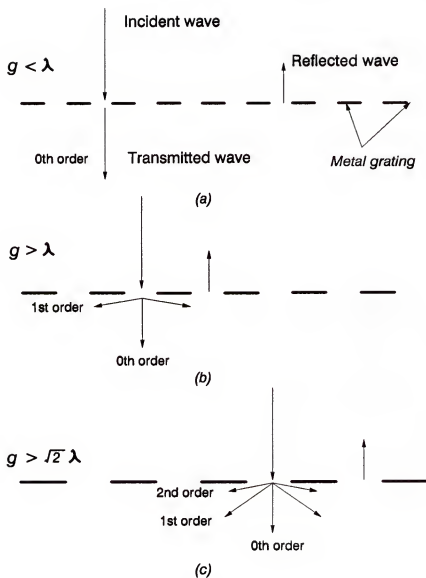


Figure 1.8 Operation of square symmetry metal grating in (a) non-diffraction region, (b) diffraction region with only one higher order diffracted waves, (c) diffraction region with two higher order diffracted waves under the normal incident irradiation at a fixed wavelength λ .

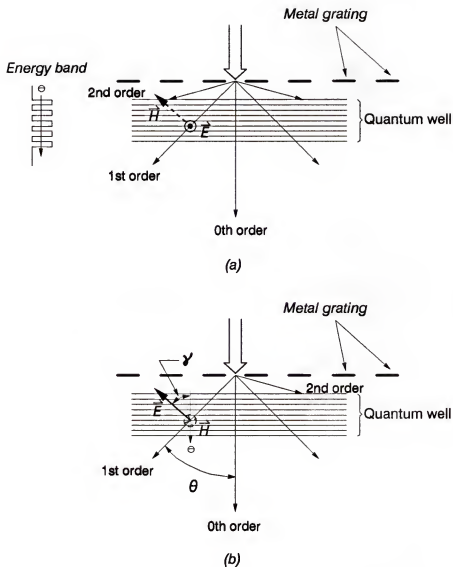


Figure 1.9 Cross section view showing the directions of grating diffracted waves for (a) TE diffracted waves with no electric field component in the carrier motion direction, (b) TM diffracted waves with an electric field component along the direction of electron motion.

CHAPTER 2

A NUMERICAL ANALYSIS OF REFLECTION SQUARE DOT METAL GRATING FOR MULTIQUANTUM WELL INFRARED PHOTODETECTORS

2.1 Introduction

Metal grating coupler operating in the diffraction region (i.e., $g > \lambda$) has drawn considerable interest in recent years since it can significantly improve the intersubband absorption in a multiple quantum well infrared photodetector (QWIP) [15-18] under normal incident illumination. A wide variety of QWIPs relying on intersubband transitions in the doped quantum wells have been demonstrated for operating in the atmospheric window of 8 to 14 μm spectral range at 77 K [31-35].

The main problem encountered in a type-I QWIP is that the electric field vector of the incident infrared (IR) radiation must have a component perpendicular to the quantum well (QW) layer planes to satisfy the selection rules of quantum mechanics intersubband absorption [36-41]. Therefore, the angle of incident light with respect to the QW layers must be non-zero in order to produce photo-response in the QWIP. One way to couple IR radiation into the QWIP is by back illumination through a 45° polished facet [42]. However, this scheme only allows incident light access to one edge of the detector, providing only one dimensional (1-D) linear array. For imaging applications in focal plane arrays (FPAs), it is necessary to be able to couple IR light uniformly into the 2-D arrays of such detectors. An alternative way of light coupling is to construct a 1-D lamellar grating to scatter light into a non-zero angle either by etching the QWIPs surface to deflect light [18] or by coating the devices with metal on one side [17,18,24] to reflect light. However, these approaches are

polarization sensitive, and only couple the transverse magnetic (TM) polarization components of the incident waves. In this chapter, we present a 2-D double periodic metal grating coupler formed on one face of the QWIP to efficiently couple the normal incident IR radiation into the QWs. This planar grating structure is independent of the polarization direction of the incident waves, and hence is suitable for FPA applications.

Radiation scattered by the grating consists of the transverse electric (TE) polarization with the electric field vector parallel to the QW planes and the TM polarization with one component of the electric field vector perpendicular to the planes. Only TM polarization leads to intersubband absorption in the QWs. Within the QWIP absorption region, the absorption constant depends on the angle between the electric field vector of the incident waves and the motion vector of free carriers (i.e., the direction perpendicular to the QW layer planes), which is defined as absorption angle. The relationship is the cosine of the angle enclosed by these two vectors [32,40]. For this reason, once the absorption constant of 45° incident angle is obtained, the power absorption ratio and quantum efficiency of the grating coupled detector can be determined by simply incorporating the power and angle of the grating scattered light into the 45° angle absorption spectrum. Therefore, large value of coupling efficiency is possible by a proper selection of grating parameters.

The analysis presented in this chapter is based on a planar double periodic reflection grating with metal dots in a square shape formed on top surface of a QWIP device. Here a normal incident electromagnetic (EM) wave impinging on the substrate side of the detector is considered. For simplicity, the power of the incident waves is assumed to be equal to unity, and the power of the higher order diffracted waves depends only on the 'normalized wavelength' s (where $s = \lambda/g$, g is the grating period and λ is the wavelength) and 'strip factor' h (where $h = a/g$, a is the width of the square dot). The absorption angle used to determine absorption constant also

depends on s . As a result, to design such a grating structure the number of parameters can be greatly reduced. Many valuable papers have been published that are concerned with the scattering of a plane wave by a cross grating [43-46], where the reflectivity of the grating is available, however, comparable normalized charts relating the higher order diffracted mode do not exist. The purpose of this chapter is to develop universal plots which relate the power of higher order diffracted waves and the diffracted angle to the normalized wavelength for a 2-D reflection square dot metal grating coupler. Using these universal plots, optimum grating sizes can be obtained for the 2-D reflection metal grating coupler in any spectral range.

2.2 The Theoretical Formalism

The diffracted EM waves in the reflection metal grating are modeled by using modal expansion technique [15,47]. The grating consists of arrays of perfect conducting square dots with infinitesimal thickness compared to the wavelength. These conducting dots are arranged periodically along two orthogonal coordinates \hat{x} and \hat{y} as shown in Fig. 2.1. In this figure we choose spherical coordinates; θ is the angle between the wave propagation vector \vec{k} and the normal to the plane of the grating, and ϕ is the angle between the x -axis and the projection of \vec{k} on the x - y plane. The distribution of electromagnetic field near the array is in the form of Floquet mode functions according to wave theory in a periodic structure. Under normal incidence, the solution of scalar wave equation is given by

$$U_{pq} = e^{-j(k_x^p x + k_y^q y)} \cdot e^{-jk_z^p z} \quad (2.1)$$

where the time dependence $e^{j\omega t}$ is omitted and the wave vectors k_x^p , k_y^q , and k_z^p in the x -, y - and z - axes are given, respectively, by

$$k_x^p = \frac{2\pi}{g} p = k \sin \theta_{pq} \cos \phi_{pq} \quad (2.2)$$

$$k_y^q = \frac{2\pi}{g} q = k \sin \theta_{pq} \sin \phi_{pq} \quad (2.3)$$

$$k_z^{pq} = \begin{cases} \sqrt{k^2 - [(k_x^p)^2 + (k_y^q)^2]} & \text{for } k^2 \geq (k_x^p)^2 + (k_y^q)^2 \\ -j\sqrt{(k_x^p)^2 + (k_y^q)^2 - k^2} & \text{for } k^2 \leq (k_x^p)^2 + (k_y^q)^2 \end{cases}$$

where k is the wavenumber in the incident side, ϕ_{pq} and θ_{pq} are the corresponding spherical coordinates for (p, q) order Floquet mode, and $p, q = 0, \pm 1, \pm 2, \dots, \pm \infty$. The z -direction wave vector k_z^{pq} depends on p and q , which is real for propagating modes, pure imaginary for evanescent modes. The orthonormal mode functions for the TE and TM Floquet modes transverse with respect to \hat{z} can be expressed as

$$\begin{aligned} \vec{\Phi}_{pq}^{TE} &= \frac{1}{g}(\sin \phi_{pq} \hat{x} - \cos \phi_{pq} \hat{y})U_{pq} & \text{for TE modes} \\ \vec{\Phi}_{pq}^{TM} &= \frac{1}{g}(\cos \phi_{pq} \hat{x} + \sin \phi_{pq} \hat{y})U_{pq} & \text{for TM modes} \end{aligned} \quad (2.4)$$

where g is the grating period in both directions and thus served as a normalized factor. The wave impedances in the z -direction are

$$\begin{aligned} \eta_{pq}^{TE} &= \frac{k}{k_z^{pq}} Z_0 \\ \eta_{pq}^{TM} &= \frac{k_z^{pq}}{k} Z_0 \end{aligned} \quad (2.5)$$

where $Z_0 = \sqrt{\frac{\mu_0}{\epsilon_0 \epsilon_r}}$ is the characteristic impedance. A plane wave with unit electric field intensity normal incidence in the ϕ plane can be expressed as the sum of TE and TM plane waves, that is,

$$\vec{E}^i = \sum_{r=1}^2 A_{00r} \vec{\Phi}_{00r} \quad (2.6)$$

where A_{00r} is the magnitude of incident field component which depends on the polarization direction. The third subscript $r = 1$ or 2 is used to designate, respectively, the TE and TM Floquet modes. Similarly, the scattered field can also be expressed in terms of the Floquet modes and reflection coefficients R_{pqr} as follows:

$$\vec{E}^s = \sum_p \sum_q \sum_{r=1}^2 R_{pqr} \vec{\Phi}_{pqr} \quad (2.7)$$

The boundary condition needs that the electric field on the conducting plate equals zero

$$\vec{E}^i + \vec{E}^s = 0 \quad \text{at } z = 0 \quad (2.8)$$

It has been shown that the current modes $\vec{\Pi}_{mnl}$ other than the Floquet modes $\vec{\Phi}_{pqr}$ were used to expand the induced current $-\hat{z} \times \vec{H}^s$ on the conducting dot in order to provide a faster convergence [47]. The $\vec{\Pi}_{mnl}$ are the dual field functions of the transverse electric field functions of the aperture spanned by the conducting dot, which satisfy the appropriate boundary conditions on the dot. For TE current modes

$$\begin{aligned} \vec{\Pi}_{mnl}(x, y) = F \left[m \sin\left(\frac{m\pi}{a}x - \frac{m\pi}{2}\right) \cos\left(\frac{n\pi}{a}y - \frac{n\pi}{2}\right) \hat{x} \right. \\ \left. + n \cos\left(\frac{m\pi}{a}x - \frac{m\pi}{2}\right) \sin\left(\frac{n\pi}{a}y - \frac{n\pi}{2}\right) \hat{y} \right] \end{aligned} \quad (2.9)$$

where

$$F = \frac{\sqrt{\epsilon_{0n}\epsilon_{0m}}}{g} \frac{1}{\sqrt{m^2 + n^2}}$$

is the normalized factor of the vector function $\vec{\Pi}_{mnl}$, ϵ_{0n} is the Newmann factor, ϵ_{0n} equals 1 for $n = 0$ and ϵ_{0n} equals 2 for $n \geq 1$, and a is the width of square conducting dot. The TM current modes $\vec{\Pi}_{mn2}$ can be derived in a similar way as Eq. (2.9). Employing ‘method of moments’, an equation in the following matrix expression can be obtained

$$[Z_{mnl}^{MNL}] [W_{mnl}] = [I_{mnl}] \quad (2.10)$$

where the unknowns W_{mnl} are the coefficients given in the current expression, the terms

$$Z_{mnl}^{MNL} = \sum_p \sum_q \sum_{r=1}^2 \eta_{pqr} C_{pqr}^{MNL*} C_{pqr}^{mnl}$$

depend on the grating geometry,

$$C_{pqr}^{mnl} = \int \int_{a/2 \leq x, y \leq a/2} \vec{\Phi}_{pqr}^* \cdot \vec{\Pi}_{mnl} dx dy \quad (2.11)$$

are the inner product of vector functions, and

$$I_{mnl} = A_{001}C_{001}^{mnl*} + A_{002}C_{002}^{mnl*} \quad (2.12)$$

is the matrix depending on incident polarization. The reflection coefficients are given by substituting current modes expansion $-\hat{z} \times \vec{H}^s = \sum_{m,n} \sum_l W_{mnl} \vec{\Pi}_{mnl}$ into Eq. (2.7). The result is

$$R_{pqr} = -\eta_{pqr} \sum_m \sum_n \sum_{l=1}^2 W_{mnl} C_{pqr}^{mnl} \quad (2.13)$$

The normalized power carried by (p, q) order TM propagating mode is written by

$$\mathcal{P}_{pq2} = \frac{|R_{pq2}|^2}{\cos \theta_{pq2}} \quad (2.14)$$

Since W_{mnl} varies with λ^2 and C_{pqr}^{mnl} is proportional to $1/\lambda^2$ for a given g , the reflection coefficient R_{pqr} in Eq. (2.13) is a function of λ/g . As a result, the normalized power \mathcal{P}_{pq2} is also a function of λ/g . The absorption angle between the electric field vector of the higher order TM diffracted mode $R_{pq2} \vec{\Phi}_{pq2}$ and the z -axis is designated as γ_{pq2} , and cosine of this angle depends on the order of diffraction and the normalized wavelength $s (= \lambda/g$, where λ is the wavelength in the detector medium) as given by

$$\cos \gamma_{pq2} = s \sqrt{p^2 + q^2} \quad (2.15)$$

2.3 Results and Discussion

As discussed above, the evanescent modes of the grating do not produce intersub-band absorption [17] in the quantum wells; neither do the TE modes. Therefore, the following discussion will focus only on the propagating TM modes. It is convenient to introduce two normalized parameters here for use in the universal plots for the square dot metal grating structure; these are the normalized wavelength $s = \lambda/g$ and the strip factor $h = a/g$. In the computer implementations, for reasons of available memory space (limited to about 20,000 double precision complex numbers), the series in Eqs. (2.13) and (2.7) were truncated so that up to forty current modes and 5000

Floquet modes were included. The numerical results presented below are sufficiently accurate by checking their convergence with increasing numbers of Floquet modes and current modes. For larger strip factors ($a/g > 0.85$), a much larger number of current modes is required to expand the induced current. Analysis of large strip factor are also unnecessary since it is more difficult to fabricate such grating on QWIP. The incident waves are plane waves that have an angle of zero degree with respect to the array normal. In order to interact with the doped quantum well, the effective coupling of the diffracted wave is due to TM Floquet modes. For grating period g less than wavelength λ , the grating is operated in non-diffraction region with only one (zeroth order) far field propagating mode $R_{00i}\vec{\Phi}_{00i}$, $i = 1, 2$. The approach used here to create effective coupling is to excite the higher order TM diffracted waves into the QWs. At $\lambda = g$ the four (1,0) diffracted waves $R_{012}\vec{\Phi}_{01}^{TM}$, $R_{0-12}\vec{\Phi}_{0-1}^{TM}$, $R_{-102}\vec{\Phi}_{-10}^{TM}$ and $R_{102}\vec{\Phi}_{10}^{TM}$ become propagating. At longer wavelength they are evanescent and their amplitude is attenuated to $1/e$ at a distance $(g/2\pi)(1 - g^2/\lambda^2)^{-1/2}$ on the grating dot matrix. For $g \approx \lambda$, this distance is larger than the spacings of the dot, and the evanescent waves can transfer substantial amounts of energy from one dot to the next. Therefore, at $\lambda = g$ the total power carried by propagating waves drops to a minimum value. Figure 2.2(a) shows the first universal plot, which illustrates that the total power of the first order TM diffracted waves as a function of the normalized wavelength for $s < 1$. For a square conducting dot grating, the total power of the first order TM diffracted waves varies with $s = \lambda/g$ but is independent of the polarization direction of the incident waves. This is due to the structure symmetry in the x and y directions under normal incidence. Figure 2.2(b) shows a plot of total diffracted power versus wavelength for a grating with $g = 4\mu\text{m}$ for different dot width a .

The absorption constant depends essentially on the angle between the electric field vector and the normal of the QW layers within the absorption band [32,40]. For a given QW structure, the total power absorbed by the detector can be easily

determined. Figure 2.2(a) shows that the total power of the first order TM diffracted waves will increase with increasing the value of h . Figure 2.3 illustrates the total power of the second order TM diffracted components $R_{-1\pm 12}\tilde{\Phi}_{-1\pm 12}$ and $R_{1\pm 12}\tilde{\Phi}_{1\pm 12}$ as a function of the normalized wavelength s for different values of h . A comparison of Figs. 2.2(a) and 2.3 reveals that the first order diffraction power is much larger than the second order diffraction power, particularly for larger values of h . The second order diffracted modes emerge for $s < 1/\sqrt{2}$ with total power about one eighth that of the first order diffracted modes.

Figure 2.4 shows an universal plot that relates $\cos \gamma_{pq2}$ to the normalized wavelength of the higher order diffracted waves, where γ is the angle enclosed by the electric field vector of the diffracted waves and the grating normal. The relationship for the first order diffracted waves (i.e. $|p| + |q| = 1$ in the notation of Floquet modes $\tilde{\Phi}_{pqr}$) is given by

$$\cos \gamma_{pq2} = \frac{\lambda}{g} \quad (2.16)$$

The relationship for the second order diffracted waves with $|p| = |q| = 1$ is

$$\cos \gamma_{pq2} = \sqrt{2}s \quad (2.17)$$

where λ is the wavelength in the detector medium.

Due to the dependence of the absorption constant on $\cos^2 \gamma_{pq2}$, we suggest that the metal grating period to be selected in the region where s varying between 0.7 and 1 when utilizes the first order diffracted waves. Referring to Fig. 2.2(a), it is noted that for $h = 0.8$ the coupling is relatively flat over a broad wavelength regime. Thus, $h = 0.8$ may be considered as a better selection for coupling IR light into the QWs. For example, for a GaAs QWIP with peak response λ_p at $10 \mu\text{m}$ wavelength, by choosing $s = \lambda_p/g = 0.77$ and $h = 0.8$, we obtain a relatively flat effective coupling spectrum covering the wavelength from 8 to $12 \mu\text{m}$ as shown in Fig. 2.2(b). Since the

refraction index n_r of GaAs contact layer is equal to 3.25 at 77K, the grating period and metal dot width are found to be $g = 4.0\mu\text{m}$ and $a = 3.2\mu\text{m}$, respectively.

According to Refs. 49 and 50, the absorption constant can be fit by a Lorentzian line shape in the following expression

$$\alpha(\nu, \gamma) \propto \frac{\Gamma(\nu)}{[(\nu - \nu_0)^2 + \Gamma^2(\nu)]} \cos^2 \gamma \quad (2.18)$$

where $\Gamma(\nu)$ is the line width, ν_0 is the peak absorption frequency and γ is the absorption angle. The $\Gamma(\nu)$ and ν_0 were used as two fitting parameters. The QWIP structure used here as an example of grating design is the extended long wavelength $\lambda = 11 \sim 15\mu\text{m}$ GaAs/AlGaAs QWIP based on a localized bound state -to- extended continuous band transition reported by Zussman *et al.* [50], which consists of 50 periods of GaAs quantum wells with well width $L_w = 60\text{\AA}$ (doped $n = 5 \times 10^{17} \text{ cm}^{-3}$) and $\text{Al}_{0.15}\text{Ga}_{0.85}\text{As}$ barriers of thickness $L_b = 500\text{\AA}$ (i.e., a superlattice length $l = 2.75\mu\text{m}$), sandwiched between $0.5\mu\text{m}$ top and $1\mu\text{m}$ bottom contact layers GaAs of $n = 1 \times 10^{18} \text{ cm}^{-3}$ GaAs. After comparing the 45° incident absorption constant given by Ref. 51, the Lorentzian fit is plotted in Fig. 2.5 as a broken line. In the figure, we also plot the absorption constant of the above detector sample coupled by a square dot metal grating under normal incident illumination, where $g = 5\mu\text{m}$ is the grating period and $a = 4\mu\text{m}$ is the square metal dot width. The quantum efficiency [51] corresponding to the absorption curve of Fig. 2.5 is illustrated in Fig. 2.6. The low quantum efficiency found in Fig. 2.6 is mainly due to the low doping density of the QWIP.

The recent results on a grating coupled QWIP shows a good agreement with the theoretical analysis. The QWIP used in our experiment was an InGaAs/InAlAs miniband transport QWIP [52] coupled by a square dot reflection metal grating with grating parameters $g = 4\mu\text{m}$ and $a = 3\mu\text{m}$ under normal incidence illumination. The refractive index n_r of the detector medium is equal to 3.7. A comparison between the theoretical calculations and the experimental data is illustrated in Fig. 2.7.

2.4 Conclusion

In conclusion, we have performed a numerical analysis of the normal incident 2-D reflection square dot metal grating coupler for the QWIP devices. The method of moments is used to implement the numerical calculations. The main advantage for such a grating structure is that the coupling of the normal incident IR radiation is independent of light polarization direction. It is shown that the total power and the angle of the higher order diffracted waves depend on two normalized parameters $s = \lambda/g$ and $h = a/g$ which are functions of wavelength and square dot dimensions. By using simple scaling rule in the universal plots shown in Figs. 2.2 to 2.4, the optimized grating period and metal dot width can be obtained for a specified infrared band detection in imaging applications.

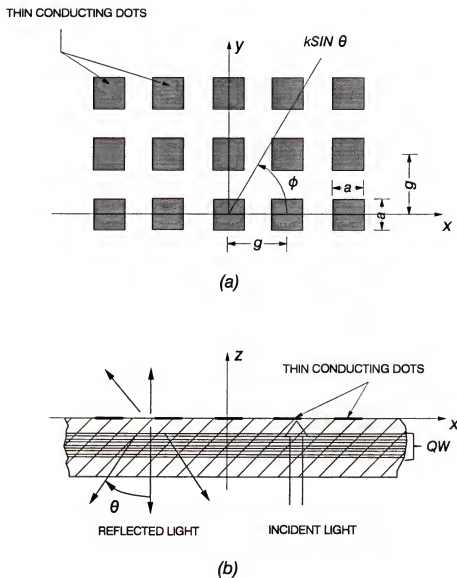


Figure 2.1 Schematic diagram showing the square dot reflection metal grating and the directions of incident and refracted waves.
 (a) Top view. (b) Side view.

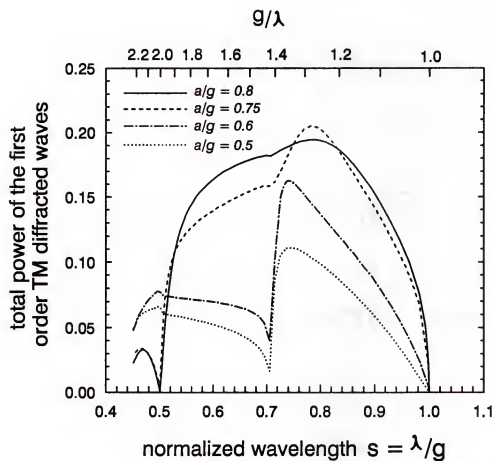


Figure 2.2(a) Total power of the first order diffracted waves versus $s = \lambda/g$ for different values of $h = a/g$, where g is grating period and a is metal dot width.

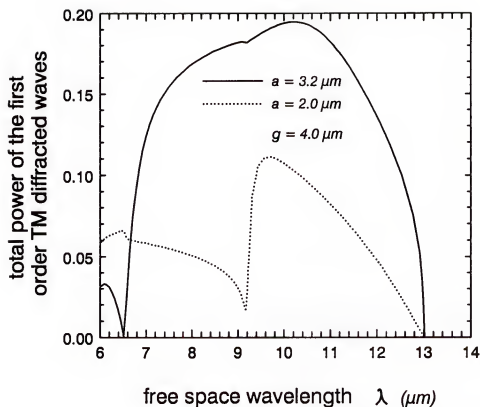


Figure 2.2(b) Replot of Fig. 2.2(a) versus wavelength for $g = 4.0 \mu\text{m}$ and $a = 2.0, 3.2 \mu\text{m}$. The refractive index of GaAs is 3.25 in 77K. Normal incident backside illumination of the grating is assumed.

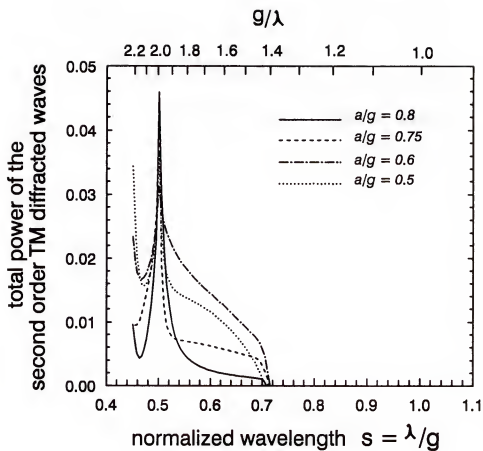


Figure 2.3 Total power of the second order diffracted wave as a function of $s = \lambda/g$ for different values of $h = a/g$. Normal incident backside illumination of the grating is assumed.

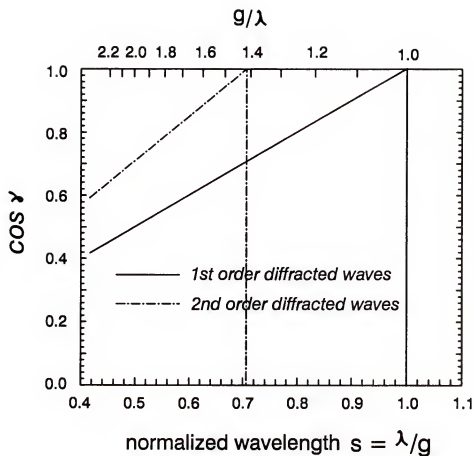


Figure 2.4 Cosine of the angle between the electric field vector of TM diffracted waves and the z-axis versus normalized wavelength.

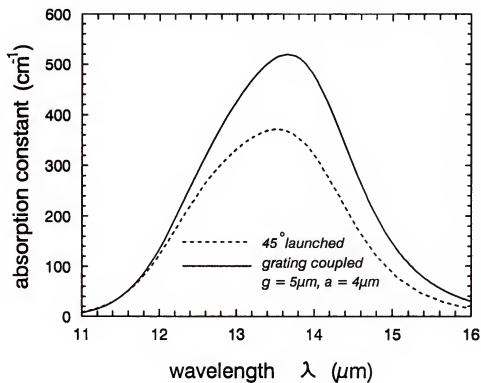


Figure 2.5 The absorption constant of an extended long wavelength QWIP [50] by both grating coupling and 45° light incidence. Where $g = 5\mu\text{m}$ is the grating period and $a = 4\mu\text{m}$ is the width of square dot in the metal grating.

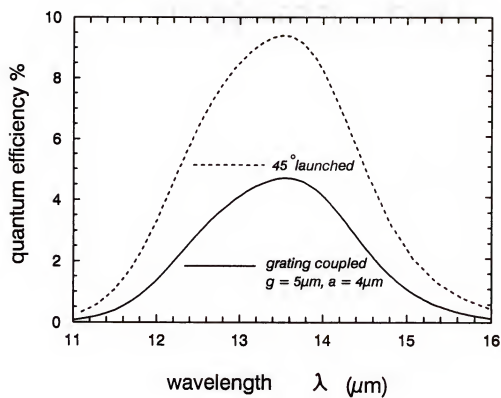


Figure 2.6 The corresponding coupling quantum efficiency of Fig. 2.5.

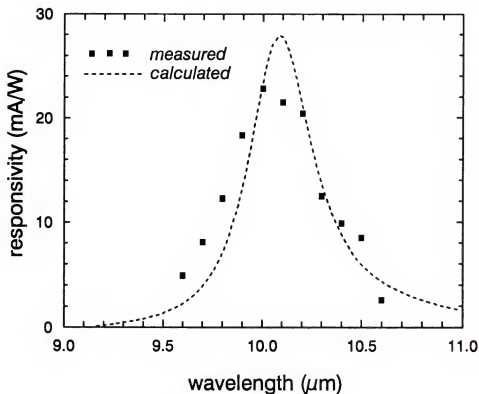


Figure 2.7 The responsivity of a 2-D square dot metal grating coupled BTM QWIP measured at 61 K. The QWIP consists of 20 periods of enlarged $\text{In}_{0.53}\text{Ga}_{0.47}\text{As}$ quantum wells with a well width of 110\AA and a dopant density $5 \times 10^{17} \text{ cm}^{-3}$. The barrier layers on each side of the QW consist of 6 periods of undoped $\text{In}_{0.52}\text{Al}_{0.48}\text{As}(35\text{\AA})/\text{In}_{0.53}\text{Ga}_{0.47}\text{As}(50\text{\AA})$ superlattice layers. The grating period $g = 4\mu\text{m}$ and dot width $a = 3\mu\text{m}$.

CHAPTER 3
DESIGN OF A TWO-DIMENSIONAL SQUARE APERTURE MESH
METAL GRATING COUPLER FOR A MINIBAND TRANSPORT
GaAs QUANTUM WELL INFRARED PHOTODETECTOR

3.1 Introduction

Recently, a considerable interest in the long wavelength intersubband quantum well infrared photodetectors (QWIPs) for operating in the 8 to 12 μ m atmospheric window region at 77K has been reported in the literature [53-56]. Most of these QWIPs were fabricated using a large bandgap III-V system semiconductor material such as GaAs/AlGaAs instead of the more difficult narrow bandgap material such as HgCdTe. The GaAs QWIP offers a very promising approach for the long wavelength infrared (IR) detection due to the matured GaAs growth and processing technology. Low cost and extremely uniform large area focal plane arrays (FPAs) can be fabricated using GaAs QWIPs for staring IR image sensor applications [57]. However, these intersubband transition QWIPs do not absorb normal incident IR radiation, since the electric field vector of the incident light must have a component perpendicular to the quantum well (QW) layers in order to induce intersubband transitions [39,58-59]. As a result, the angle of incidence with respect to the normal of QW layers must be different from zero in order to produce photo-signal. On the other hand, for the fabrication of FPAs, a response in normal incident light is required. A linear grating is candidate for applicant to 2-D detector array [17,21,22], nevertheless, it suffers from a low coupling efficiency due to its polarization selectivity. A double periodic metal grating formed on the top of a QWIP can be employed to deflect the normal incident light into an absorbable angle independent of light polarization. There are

two approaches to form a double periodic grating on a QWIP: one method is to deposit a metal grating directly onto the detector as shown in Fig. 3.1, and the other approach is to chemically etch the top surface layer of the detectors to a desired profile followed by metal deposition [25,26]. The former has the advantage over the latter in that it uses a simple planar metal grating structure which avoids the unwanted nonuniform etching on the detector surface and hence reduces the processing difficulties. In this chapter we report a numerical analysis of a planar 2-D square mesh metal grating by depositing metal grid directly onto the top cap layer of the GaAs bound-to-miniband (BTM) QWIP. The detector can be illuminated either on the front side or the back side. The results showed that coupling quantum efficiency of the detector under back side illumination is 2.34 times higher than that under the front illumination.

For practical applications, the electromagnetic (EM) waves impinge on a QWIP under normal incident illumination. The radiation scattered by the 2-D metal grating consists of the TE polarization with electric field vector parallel to the QW planes and the TM polarization with one component of the electric field vector perpendicular to the QW planes. Only TM components of the IR radiation will lead to intersubband absorption in the QWs. In the square mesh metal grating structure shown in Fig. 3.1, for a unit amplitude normal incident light, the total power of each order diffracted mode depends on the 'normalized wavelength' $s = \lambda/g$ (where g is the grating period and λ is the *free space wavelength*) and the 'strip factor' $h = a/g$ (where a is the width of the square aperture in the metal grating). Furthermore, the angle between each order of the diffracted waves and the grating normal defined by absorption angle is determined by the parameter s and the diffracted order. The intersubband absorption in the quantum well of a BTM QWIP is a function of the total power of the higher order TM diffracted waves and the diffracted angle [32]. The grating scattering problem has already been investigated by many authors [43-46]. The objective of this chapter is, however, not to present yet another solution to this scattering problem

but to generate the novel universal plots from which the total power of higher order TM diffracted waves and the absorption angle can be determined for different grating periods and aperture sizes of the 2-D square aperture mesh metal grating coupler on GaAs BTM QWIP. Together with the absorption constant of intersubband transition, these plots provide a convenient way for obtaining an optimum grating coupler for the BTM QWIPs structure.

3.2 Basic Theory

The basic theory used in deriving the unknown scattered waves of a 2-D square aperture mesh metal grating coupler is based on the modal expansion technique [59]. The grating consists of an infinitesimal thickness perfect conducting screen perforated with square apertures distributed periodically along two orthogonal coordinates \hat{x} and \hat{y} as shown in Fig. 3.1. The direction of scattered waves is specified by the spherical polar angles; θ is the angle of declination of the wave propagation vector \vec{k} measured from the $+z$ axis, and ϕ is the azimuthal angle measured with a counterclockwise sense from x axis of Fig. 3.1(a). The mesh metal grating is formed on top of the QWIP. The basic form of electromagnetic field near the grating array is Floquet mode functions, therefore, under normal incident illumination the solution of scalar wave equation with time dependence $e^{j\omega t}$ omitted is given by

$$U_{pq} = e^{-j(k_x^p x + k_y^q y + k_z^{pq} z)} \quad (3.1)$$

where the wave vectors k_x^p , k_y^q , and k_z^{pq} in the x -, y - and z - axes are given, respectively, by Eqs. (2.2) and (2.3) where k is the wavenumber in free space. The vector orthonormal mode functions for the TE and TM modes transverse with respect to \hat{z} can be expressed as Eq. (2.4). The wave admittances looking into the air region from $z = 0^+$ plane are

$$\zeta_{pq}^{TE} = \frac{k_z^{pq}}{k} \frac{1}{Z_0}$$

$$\zeta_{pq}^{TM} = \frac{k}{k_z^{pq}} \frac{1}{Z_0} \quad (3.2)$$

where $Z_0 = \sqrt{\mu_0/\epsilon_0}$ is the free space characteristic impedance. Assuming that the impedance between all the quantum well layers are perfectly matched and the inter-subband absorption is complete so that no waves are reflected from the transmitted end of the QWIP. Under this condition, the modal admittances for TE and TM waves looking into the QW region from $z = 0^+$ plane are obtained by replacing Z_0 in Eq. (3.2) by $Z_d = \sqrt{\mu_0/\epsilon_0\epsilon_r}$ for GaAs, which yields

$$\begin{aligned} \zeta_{pq}^{dTE} &= \frac{k_z^{pq}}{k} \frac{1}{Z_d} \\ \zeta_{pq}^{dTM} &= \frac{k}{k_z^{pq}} \frac{1}{Z_d} \end{aligned} \quad (3.3)$$

A plane wave with unit electric field intensity normal incident in the ϕ plane can be expressed as the sum of TE and TM plane waves as described in Eq. (2.6), $\vec{E}^i = \sum_{r=1}^2 A_{00r} \vec{\Phi}_{00r}$, where the third subscript $r = 1$ or 2 is used to designate the TE and TM Floquet modes, respectively. In fact, the wave expansion consists of both upward and downward waves; in a similar way, the reflected waves and transmitted waves can also be expressed in terms of the Floquet modes with reflection coefficient R_{pqr} and transmission coefficient T_{pqr} as following

$$\begin{aligned} \vec{E}^t &= \sum_{r=1}^2 A_{00r} \vec{\Phi}_{00r} + \sum_p \sum_q \sum_{r=1}^2 R_{pqr} \vec{\Phi}_{pqr} \\ &= \sum_p \sum_q \sum_{r=1}^2 T_{pqr} \vec{\Phi}_{pqr} \end{aligned} \quad (3.4)$$

Equation (3.4) includes the boundary condition that the tangential component of electric field vector in the aperture is continuous. The orthonormal waveguide modes $\vec{\Pi}_{mnl}$ of the square aperture itself other than the Floquet modes $\vec{\Phi}_{pqr}$ were used to expand the unknown electric field distribution in the aperture in order to satisfy the boundary condition, which has been shown to provide a faster convergence [59]. For

TE waveguide modes

$$\begin{aligned} \vec{\Pi}_{mnl}(x, y) = G \left[\frac{n\pi}{b} \cos\left(\frac{m\pi}{a}x - \frac{m\pi}{2}\right) \sin\left(\frac{n\pi}{b}y - \frac{n\pi}{2}\right) \hat{x} \right. \\ \left. - \frac{m\pi}{a} \sin\left(\frac{m\pi}{a}x - \frac{m\pi}{2}\right) \cos\left(\frac{n\pi}{b}y - \frac{n\pi}{2}\right) \hat{y} \right] \end{aligned} \quad (3.5)$$

where

$$G = \frac{\sqrt{\epsilon_{0n}\epsilon_{0m}}}{g} \left[\sqrt{\left(\frac{m\pi}{a}\right)^2 + \left(\frac{n\pi}{b}\right)^2} \right]^{-1}$$

is the normalized factor of the vector function $\vec{\Pi}_{mnl}$, and ϵ_{0n} is the Newmann factor, ϵ_{0n} equals 1 for $n = 0$ and ϵ_{0n} equals 2 for $n \geq 1$, a and b are the width of the square aperture in the direction \hat{x} and \hat{y} , respectively, here $b = a$. The TM waveguide modes $\vec{\Pi}_{mn2}$ are derived in a similar way. As a result, \vec{E}^t can be expressed by

$$\vec{E}^t = \sum_m \sum_n \sum_{l=1}^2 W_{mnl} \vec{\Pi}_{mnl} \quad (3.6)$$

where the unknowns W_{mnl} are the coefficients given in the waveguide mode expression. After substituting Eq. (3.6) into (3.4) followed by taking inner product of vector functions $\vec{\Pi}_{mnl}$ and $\vec{\Phi}_{pqr}$, a matrix equation is obtained by

$$[Y_{mnl}^{MNL}] [W_{mnl}] = [I_{mnl}] \quad (3.7)$$

where

$$\begin{aligned} Y_{mnl}^{MNL} = \sum_p \sum_q \sum_{r=1}^2 (\xi_{pqr} + \xi_{pqr}^d) C_{pqr}^{MNL*} C_{pqr}^{mnl}, \\ C_{pqr}^{mnl} = \int \int_{\text{aperture}} \vec{\Phi}_{pqr}^* \cdot \vec{\Pi}_{mnl} dx dy, \end{aligned} \quad (3.8)$$

and the incidence depending on matrix

$$I_{mnl} = 2 \sum_{r=1}^2 A_{00r} \epsilon_{00r}^d C_{00r}^{mnl*} \quad (3.9)$$

The higher order transmission coefficient and reflection coefficient are given, respectively, by

$$T_{pqr} = \sum_m \sum_n \sum_{l=1}^2 W_{mnl} C_{pqr}^{mnl} \quad p, q \neq 0, 0 \quad (3.10)$$

and

$$R_{pqr} = \sum_m \sum_n \sum_{l=1}^2 W_{mnl} C_{pqr}^{mnl} \quad p, q \neq 0, 0 \quad (3.11)$$

Since W_{mnl} is proportional to λ^2 and C_{pqr}^{mnl} varies as $1/\lambda^2$ for a given g , the transmission coefficient T_{pqr} and reflection coefficient R_{pqr} are a function of λ/g . The normalized diffracted power of (p, q) order TM propagating mode is given as Eq. (2.14). The absorption angle between the electric field of the higher order TM diffracted modes $T_{pq2}\vec{\Phi}_{pq2}$ or $R_{pq2}\vec{\Phi}_{pq2}$ and the \hat{z} direction is designated as γ_{pq2} , and the cosine of this angle depends on the diffracted order and normalized wavelength s ($= \lambda/g$) as given by

$$\cos \gamma_{pq2} = \frac{s}{n_r} \sqrt{p^2 + q^2} \quad (3.12)$$

where n_r is the refractive index of the medium in which the EM waves propagate.

The 2-D square mesh grating coupled GaAs/AlGaAs BTM QWIP structure used in the present analysis is based on the transition from the ground bound state in the enlarged well to the global miniband in the superlattice barrier [19] as shown in Fig. 3.2. In this QWIP the 2-D electrons in the miniband can move freely in the direction perpendicular to the QW layers and may give rise to an electrical current through the QWIP. The intersubband absorption constant can be expressed by [32]

$$\alpha = \left(\frac{e^2 \hbar^3}{m^* n_r \epsilon_0 c} \right) \frac{n_e \cos^2 \gamma T_i^2 \sqrt{(E - E_{min})(E_{max} - E)}}{\hbar \omega (U + S_1)^2 - S_1(E_{max} - E)} \quad (3.13)$$

where e is the electronic charge, m^* is the effective mass, c is the speed of light, n_e is the electron density in the wells, ω is the angular frequency of the EM waves, γ is the angle between the electric field vector of the IR radiation and the motion vector of electrons, E_{max} and E_{min} are the two extreme edge of the miniband as shown in Fig. 3.2. All other parameters, T_i , U and S_1 in Eq. (3.13) depend on the specific quantum well structure and wavelength of the incident IR radiation. Substituting Eq. (3.12) into (3.13), the absorption constant of the QWIP in the spectral range of interest can be readily calculated.

3.3 Results and Discussion

The evanescent modes excited by the grating produce no photoresponse in quantum well intersubband transition; neither do TE modes [17,60]. Therefore, the following discussion will be focused on the propagating TM modes in the QW region. It is convenient to use two normalized parameters, namely, ' $s = \lambda/g$ ' and ' $h = a/g$ ' to illustrate the universal plots for the square aperture mesh metal grating. Rigorous calculations were made by using the lowest 40 waveguide modes, the addition of more higher order modes made no noticeable change in the transmission and reflection coefficients. When analyzing the mesh grating with larger strip factor ($a/g > 0.85$), a much larger number of waveguide modes is required to simulate the wave distribution at the metal edge. Large strip factor is also undesirable for the practical QWIP, since it is more difficult to deposit such a fine metal line (i.e. less than $1 \mu\text{m}$) on the detector surface.

An EM wave with unit power density impinging on the mesh metal grating at zero degree angle with respect to the grating normal is considered. Besides, the following discussion is mainly based on the back side illumination as shown in Fig. 3.1(b). The effective coupling is due to non-zeroth order reflected TM Floquet modes, since the TE Floquet modes have an angle $\gamma = 90^\circ$ in Eq. (3.13). Figure 3 shows the first universal plot, which illustrates the normalized total power of the first order TM diffracted waves $R_{012}\vec{\Phi}_{012}$, $R_{0-12}\vec{\Phi}_{0-12}$, $R_{-102}\vec{\Phi}_{-102}$ and $R_{102}\vec{\Phi}_{102}$ as a function of the normalized wavelength $s = \lambda/g$ for different values of h . We can also obtain the power of the transmitted Floquet modes under front illumination shown in Fig. 3.1(c) by dividing the normalized power in Fig. 3.3 by a factor 2.34, which includes a modification factor 0.72 to account for the power reflection owing to the impedance mismatch between air ($n_r = 1$) and GaAs ($n_r = 3.25$ at 77K). The first order diffracted waves become propagating when the wavelength of the light in GaAs is smaller than the grating period, that is, $s = \lambda/g < 3.25$. For the same reason, within the spectral

range in Fig. 3.3, only zeroth order far field transmitted waves $T_{00i}\tilde{\Phi}_{00i}$ ($i = 1, 2$) in the free space might be found, and all other higher order transmitted waves were cut-off. This is due to the fact that free space wavelength λ is greater than the grating period g and thus makes the grating operating in the non-diffraction region on the air side. In addition, the square mesh grating is indistinguishable between x and y directions. The total normalized power of the first order diffracted waves generated by x and y components of the incident waves remain the same for different input polarizations. In other words, the coupling of the grating is polarization independent. A rather flat coupling curve for $h = a/g = 0.5$ in Fig. 3.3 may be treated as a better choice for coupling the IR radiation more efficiently into the QWIP. Figure 3.4 illustrates the normalized total power of the second order TM diffracted components $R_{\pm 112}\tilde{\Phi}_{\pm 112}$ and $R_{1\pm 12}\tilde{\Phi}_{1\pm 12}$ as a function of the normalized wavelength s for various values of h . Similarly, the second order transmitted TM components under front illumination (Fig. 3.1(c)) is obtained by dividing the coupling power in Fig. 3.4 by a factor of 2.34 if the reflective effect at the air-GaAs interface is modified. A comparison of Figs. 3.3 and 3.4 reveals that those gratings exciting larger power of the first order diffracted waves will excite larger power of the second order diffracted waves too. The second order diffracted waves emerge for $s < 2.298$ with a total power about 50% smaller than that of the first order diffracted waves.

Figure 3.5 shows a universal plot that relates $\cos \gamma_{pq2}$ to the normalized wavelength of the higher order diffracted waves, where γ is the absorption angle. The relationship for the first order diffracted waves (i.e. $|p| + |q| = 1$ in the notation of Floquet modes $\tilde{\Phi}_{pqr}$) is given by

$$\cos \gamma_{pq2} = \frac{\lambda/n_r}{g} \quad (3.14)$$

The relationship for the second order diffracted waves with $|p| + |q| = 1$ is

$$\cos \gamma_{pq2} = \frac{\lambda/n_r}{g} \sqrt{2} \quad (3.15)$$

We next calculate the absorption constant versus wavelength in a 2-D square mesh metal grating coupled GaAs BTM QWIP. The mesh grating period is selected in the region where $2.298 < s < 3.25$ falls in the QWIP absorption band by using the first order TM diffracted waves. In this case, $\cos^2 \gamma$ is greater than $1/2$ which corresponds to the light launching at a 45° angle. If we select the curve with $h = 0.5$ in Fig. 3.3, then by multiplying the grating period $g = 4\mu\text{m}$ to the coordinate, a rather flat curve of the coupling efficiency over a broad wavelength regime $9\text{--}13\mu\text{m}$ can be obtained, as shown in Fig. 3.6(a). By substituting the corresponding $\cos \gamma$ in Fig. 3.6(a) and using the QWIP parameters given in Fig. 3.2 into Eq. (3.13), we obtain the absorption constant versus wavelength for the GaAs BTM QWIP as shown in Fig. 3.7(a). Note that, the dot line represents the absorption constant of the QWIP with IR launched at a 45° polished facet and the electron interactive effect [61,62] has been considered. The aperture width of the mesh metal grating in the above example was found to be $a = (4\mu\text{m}) \times 0.5 = 2\mu\text{m}$. The coupling quantum efficiency η for the QWIP [32,51] can be calculated by using the expression

$$\eta = \mathcal{P}_{eff}(1 - e^{-\alpha l}) \quad (3.16)$$

where \mathcal{P}_{eff} is the effective coupling power of the light and l is the total length of the doped quantum wells. In the present case, \mathcal{P}_{eff} is the normalized total power of the first order diffracted waves, $l = (88\text{\AA}) \times (40 \text{ periods}) = 3520\text{\AA}$, and η is shown as a broken line in Fig. 3.7(b).

The optimum square aperture mesh metal grating used for the above BTM QWIP is $g = 3.3\mu\text{m}$ and $a = 2\mu\text{m}$, corresponding to the curve with $h/g = 0.6$ in Fig. 3.3. Following the same procedure, the characteristic curve of the first order TM diffracted waves for such a grating under back illumination was plotted in Fig. 3.6(b), which

shows that the cut-off wavelength of the grating is $10.725\mu\text{m}$. The solid line in Fig. 3.7(a) illustrates the absorption constant of the optimum grating design. Figure 3.7(b) shows the quantum efficiency of the GaAs BTM QWIP under different light coupling schemes. The results show that the coupling quantum efficiency of a 2-D square mesh metal grating under back illumination is superior to that under front illumination. Furthermore, the optimum grating has a coupling efficiency larger than that of a 45° angle light coupling.

3.4 Conclusion

In conclusion, we have performed a detailed analysis of a GaAs BTM QWIP coupled with a 2-D square aperture mesh metal grating. It is shown that for a given QWIP the total power and the diffracted angle of the higher order TM diffracted waves depend on two normalized parameters $s = \lambda/g$ and $h = a/g$, which are functions of wavelength and grating parameters. By scaling the universal plots shown in Fig. 3.3 and Fig. 3.5, the optimum grating period and aperture width can be obtained for any specific infrared spectrum. Moreover, the absorption constant and the coupling quantum efficiency for a 2-D metal grating coupled QWIP can be calculated from these universal plots.

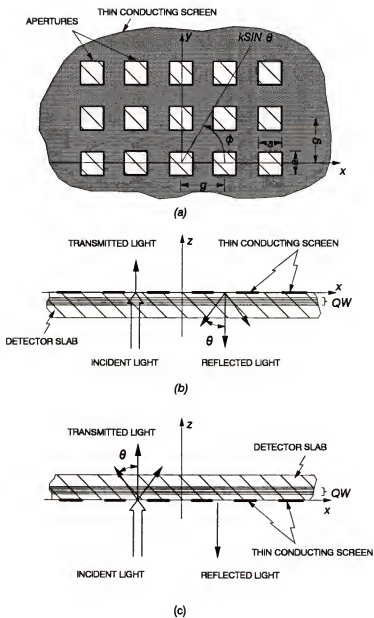


Figure 3.1 Schematic diagram for a 2-D square aperture mesh metal grating coupler. (a) Top view. (b) Side view under back illumination. (c) Side view under front illumination.

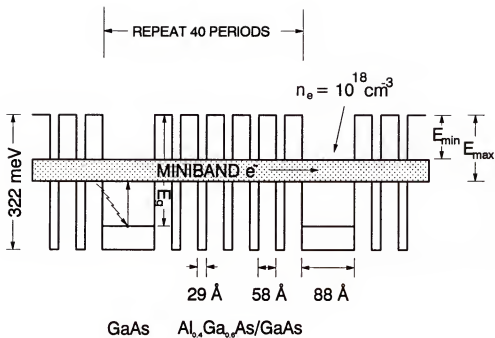


Figure 3.2 The energy band diagram for a bound-to-miniband transition GaAs/AlGaAs QWIP. The ground state E_g is calculated to be 290meV after taking the exchange energy [61,62] into consideration.

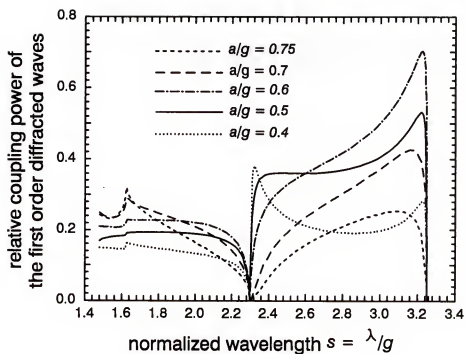


Figure 3.3 Total power of the first order diffracted waves versus normalized wavelength s for different values of h . Normal incidence and back illumination are assumed.

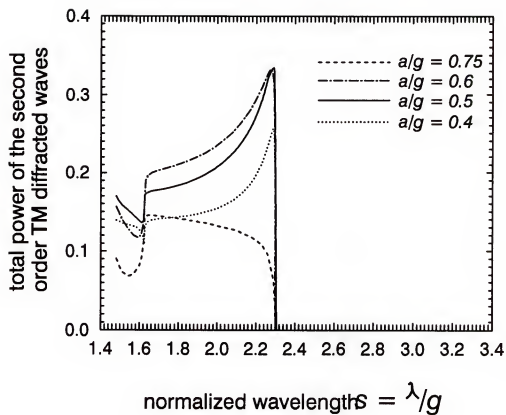


Figure 3.4 Total power of the second order diffracted waves as a function of s for different values of h . Normal incidence and back illumination are assumed.

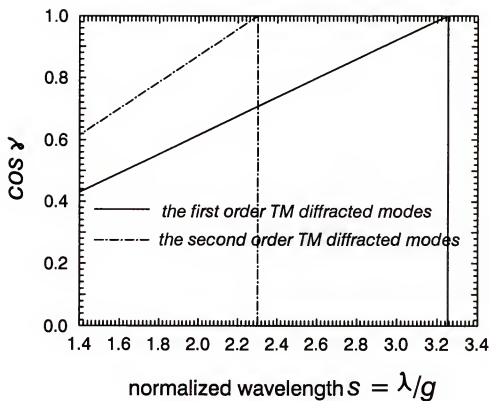


Figure 3.5 Cosine of the angle between the electric field vector of diffracted waves in the quantum well region and the normal of the quantum well layers \hat{z} versus normalized wavelength.

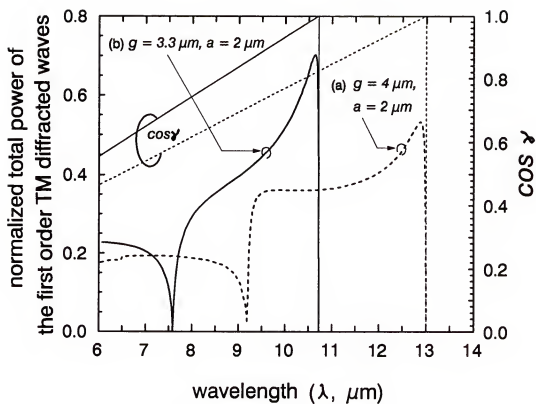


Figure 3.6 Coupling characteristic curve for the square aperture mesh metal grating with (a) $g = 4.0 \mu\text{m}$, $a = 2.0 \mu\text{m}$., and (b) $g = 3.3 \mu\text{m}$, $a = 2.0 \mu\text{m}$.

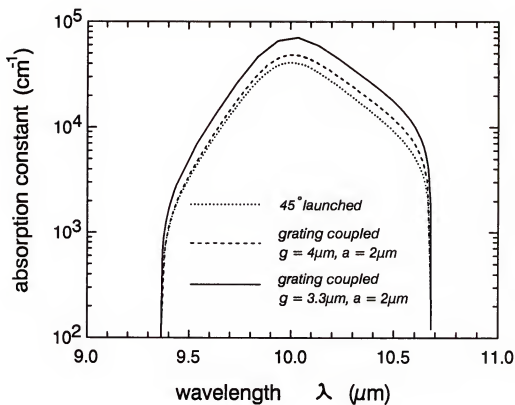


Figure 3.7(a) Absorption constant versus wavelength for a 2-D square aperture mesh metal grating coupled BTM QWIP for two different grating periods and aperture sizes and for a 45° incident illumination.

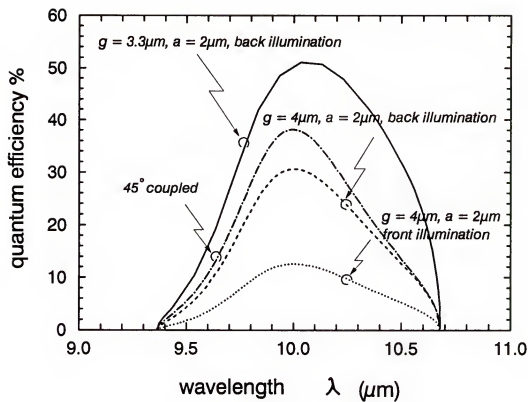


Figure 3.7(b) Corresponding coupling quantum efficiency for the BTM QWIP shown in Fig. 3.7(a).

CHAPTER 4

GEOMETRY CONSIDERATIONS OF TWO-DIMENSIONAL GRATING COUPLER FOR GaAs QUANTUM WELL INFRARED PHOTODETECTOR

4.1 Introduction

Various new types of photodetector have been demonstrated by GaAs/AlGaAs doped quantum well [63-65] structure, which rely on photodetection involving electronic transitions between two different quantum states of the quantum wells. The operation of these detectors based on so called 'intersubband' absorption of infrared radiation is preferable to other types of detectors such as narrow band gap or Schottky barrier detectors in the wavelength range of 8-12 μm . Due to the excellent large area uniformity [66] of GaAs/AlGaAs, multiple quantum well infrared photodetectors (QWIPs) show a significant promise in the manufacture of 2-D high performance focal plane arrays (FPAs).

In an intersubband absorption QWIP, the electrons are excited from bound ground state to a higher energy level miniband [19,32] or continuous band [67,68], in which the electrons can move under an applied electric field perpendicular to the plane of the quantum wells and thus produce photocurrent. The corresponding transitions are allowed only when one of the electric field components of incident IR radiation is polarized in the direction of the electron motion [69-72]. The IR light normally irradiates on the surface of detectors will not be absorbed for n-type QWIPs. Therefore, some special coupling techniques have to be employed, such as 45° angle polished facet on one edge of the detectors, Brewster's angle illumination, 1-D linear grating [21,24] and 2-D cross grating [25,26]. Input coupling through an angle pol-

ished facet increases the absorption via multiple-pass total internal reflection [42], but severely limits device geometry for detector applications. For a simple Brewster's angle incidence a relatively large number of quantum wells is required in order to achieve efficient absorption. The formation of FPA is possible in 1-D linear grating coupler, but the coupling is polarization dependent. To improve the coupling efficiency, we use a planar square aperture mesh metal grating. In our design, the top contact surface of the detector is covered with a conducting screen perforated periodically with square apertures formed by standard photolithography and lift-off techniques. The grating scatters the incident IR light into new electromagnetic waves which obey the absorption rules as described above.

However, the fabrication of extremely small grating structure inevitably involves cell-to-cell photoresponse nonuniformity of a FPAs, i.e., individual detector may exhibit differences in spectral response, which in turn could introduce spatial noise [72] and limit the sensitivity of IR imaging camera. Performance models for infrared detectors such as detectivity (D^*) or responsivity (R_I) are based on the implicit assumption that all the detectors in an IR image system are exactly the same. Unfortunately, these models fail to explain the dominant one—spatial noise in high background environments (8 to 12 μm image of practical IR staring sensors). As a result, the predict performance of system sensitivity is usually optimistic. Since the size of the square apertures in the metal grating is around one micrometers, some variation in the width and shape of the grating aperture pattern can be expected. The effect on grating performance by the variations in aperture width and shape must be considered during the QWIP FPA design.

In this chapter we performed a numerical analysis of the effects in the coupling efficiency by grating size and shape variation for a square aperture mesh metal grating coupler on GaAs QWIP. The coupling stability in grating aperture dimension was discussed. Finally, an aperture dimension which can avoid inducing uncorrected

spatial noise was also determined.

4.2 Theory and Illumination

The 2-D square aperture mesh metal grating with aperture width a and periodicity parameter or grating constant g deposited on top surface of a GaAs QWIP is illustrated in Fig. 3.1. The whole grating arrangement looks like two groups of equally spaced parallel metal lines intersect one another in rectangular angle. When a plane wave light strikes the grating under normal incidence illumination, the light is scattered into several order diffracted waves whose wave vectors have parallel components equal to integer multiples of the reciprocal lattice vector of the grating

$$k_x^p = \frac{2\pi}{g}p \quad (4.1)$$

$$k_y^q = \frac{2\pi}{g}q \quad (4.2)$$

where (p, q) is the diffracted order, and $p, q = -\infty, \dots, -2, -1, 0, 1, 2, \dots, \infty$. The total wave vector of each order diffracted waves; including evanescent waves, obeys

$$(k_x^p)^2 + (k_y^q)^2 + (k_z^{pq})^2 = (2\pi/\lambda)^2 \quad (4.3)$$

where k_z^{pq} is the perpendicular wave vector of the diffracted waves which is real for propagating waves and pure imaginary for evanescent waves, and λ is the wavelength of the incident wave. For back side illumination as shown in Fig. 3.1(b), the wave solution in the quantum well region consists of the incident wave plus a superposition of reflected diffracted waves. The wave solution in the air region consists of a superposition of transmitted diffracted waves. The incident, reflected and transmitted waves are expressed, respectively, by

$$\vec{E}^i = A_{001}\vec{\Phi}_{001} + A_{002}\vec{\Phi}_{002} \quad (4.4)$$

$$\vec{E}^r = \sum_{p,q} \sum_{r=1}^2 R_{pqr} \vec{\Phi}_{pqr} \quad (4.5)$$

$$\vec{E}^t = \sum_{p,q} \sum_{r=1}^2 T_{pqr} \vec{\Phi}_{pqr} \quad (4.6)$$

where $\vec{\Phi}_{pqr}$ are the orthonormal Floquet modes, A_{00r} , R_{pqr} and T_{pqr} are incidence, reflection and transmission coefficients, and $r = 1$ or 2 is designated as TE or TM Floquet modes, respectively. By matching the tangential electric field of each wave at the grating-air interface and elaborating the method of moments [30,59], the final equation system is transformed to a matrix expression to be solved numerically with the aid of digit computer. The coefficients of the diffracted waves are obtained in terms of the power of incident wave. The normalized power carried by (p, q) order TM reflected wave is given by

$$\mathcal{P}_{pq2} = \frac{|R_{pq2}|^2}{\cos \theta_{pq2}} \quad (4.7)$$

where θ_{pq2} is the angle between the diffracted ray and the grating normal. Figure 3.3 shows the normalized power of the first order TM diffracted waves plotted in the normalized scales λ/g and a/g . The second order diffracted waves will not appear until λ/g is smaller than 2.298 (using $n_r = 3.25$ for GaAs at 77K). The coupling efficiency of the grating depends not only on the power of each higher order TM propagating mode but also on the absorption angle enclosed by the electric field vector of the mode and the free carrier motion vector \hat{z} , which is denoted by γ

$$\cos \gamma_{pq2} = \frac{\lambda/n_r}{g} \sqrt{p^2 + q^2} \quad (4.8)$$

where n_r is the refractive index of the medium in which the wave propagates. Note that the power absorption ratio of quantum wells varies directly with the $\cos^2 \gamma$ and the diffracted power [32,73,74].

Grating period g remains constant during the photolithography procedure, the aperture width may, however, be changed. Figure 4.1 shows the coupling power of the first-order TM diffracted waves varying with normalized aperture width a/g within the most effective coupling regime $2.8 < \lambda/g < 3.2$. The results clearly show that $a/g = 0.6$ not only maximizes the coupling power but also is insensitive to the variation of aperture width. This means that $a/g = 0.6$ is a stable ratio for the

aperture width to grating period. For example, the grating $g = 3.3\mu\text{m}$, $a = 2\mu\text{m}$ used as an optimum grating in Chapter 3 is a relative stable design.

Other than the width variation, the shape of the aperture may also be distorted during the formation of grating pattern by using a contact-type mask aligner. Figure 4.2 illustrates the shape distortion of the grating aperture. In the extreme case, the square aperture becomes a circular hole with a radius r equal to one half of the square aperture width, a . Under this situation, the grating consists of metal film perforated with circular aperture. The characteristic curve of such a grating is plotted in Fig. 4.3. Almost invariant coupling curve is obtained for varying $a/g = 0.6$ to $r/g = 0.3$, which implies that the square aperture mesh metal grating with a normalized aperture width $a/g = 0.6$ is insensitive to the shape distortion even if grating pattern is not properly processed.

Another approach to avoid the deformation of grating aperture is to use a larger grating geometry which certainly has a lower coupling efficiency. For example, a square mesh grating coupler with $g = 6\mu\text{m}$ and $a = 3\mu\text{m}$ instead of $g = 4\mu\text{m}$, $a = 2\mu\text{m}$ can be chosen to couple a GaAs/AlGaAs QWIP for $9\text{--}11\mu\text{m}$ detection. Figure 4.4 illustrates the characteristic curve of the first three order diffracted waves for the $g = 6\mu\text{m}/a = 3\mu\text{m}$ grating coupler. This larger scale grating has larger aperture size, and hence is easier to fabricate within the same error tolerance limits. By using the equation given in Equation (3.13), the optical absorption constant and coupling quantum efficiency of a miniband transport QWIP (Ref 19, Fig. 3.2) is shown in Figs. 4.5(a) and (b). In these figures, two sets of grating parameters were included to facilitate the comparison. The quantum efficiency η is calculated by [51]

$$\eta = \sum_i \mathcal{P}_i (1 - e^{-\alpha_i l}) \quad (4.9)$$

where α_i is the absorption constant of i th diffracted mode, l is the total length of quantum wells (in present case, $l = (88\text{\AA}/\text{period}) \times (40 \text{ periods}) = 3520\text{\AA}$), and \mathcal{P}_i is the relative coupling power carried by the effective i th order diffracted waves.

4.3 Conclusion

In conclusion, the difficulty in the fabrication of small size square aperture mesh metal grating for 8-12 μm GaAs/AlGaAs QWIP makes the consideration in grating generated cell-to-cell nonuniformity becoming important. A detailed analysis of the effects of grating size variation and shape distortion on the coupling efficiency for a 2-D square aperture mesh metal grating coupler have been carried out. It is shown that grating generated spatial noise can be reduced either by using a relative stable aperture width or a larger grating dimension. The optimum grating has parameters of the ratio $a/g = 0.6$.

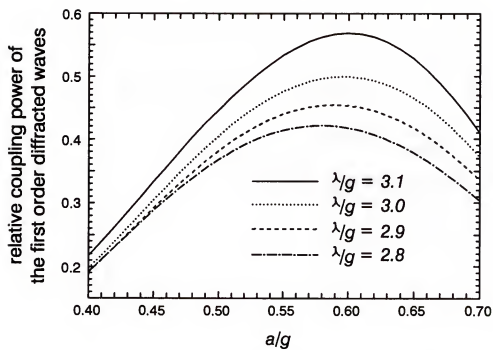


Figure 4.1 Relative coupling power of the first order TM diffracted waves versus a/g within the most significant coupling region $2.8 < s = \lambda/g < 3.1$.

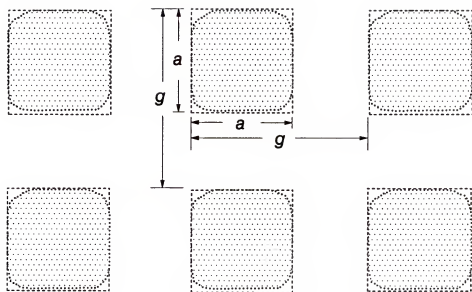


Figure 4.2 Top view of the distorted grating pattern for a 2-D square aperture mesh metal grating coupler.

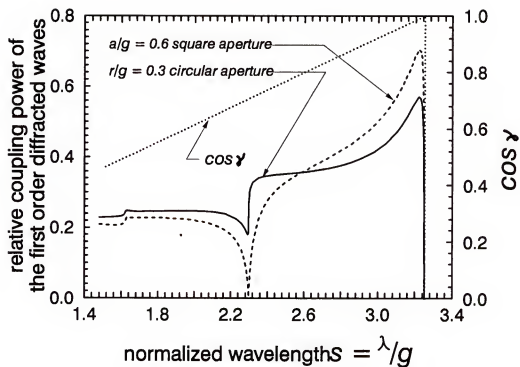


Figure 4.3 The coupling characteristic curve for the square aperture grating with $a/g = 0.6$ and circular aperture grating with $r/g = 0.3$, where $r/a = 1/2$.

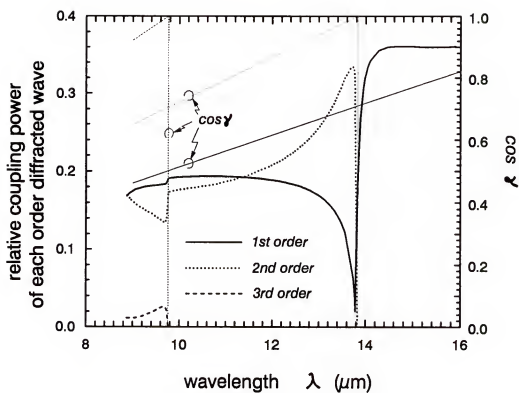


Figure 4.4 The relative coupling power of the 1st, 2nd and 3rd order TM diffracted waves versus wavelength for a 2-D square aperture metal grating with $a = 3\mu\text{m}$ and $g = 6\mu\text{m}$.

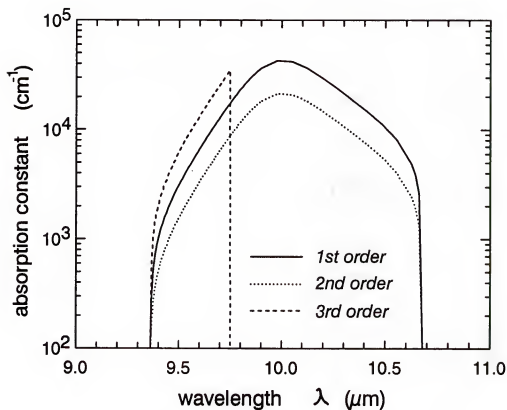


Figure 4.5(a) Spectral absorption constant of the 1st, 2nd and 3rd order TM diffracted waves for a miniband transport QWIP (Ref. 19, Fig. 3.2) coupled by the grating with coupling characteristic curve shown in Fig. 4.4.

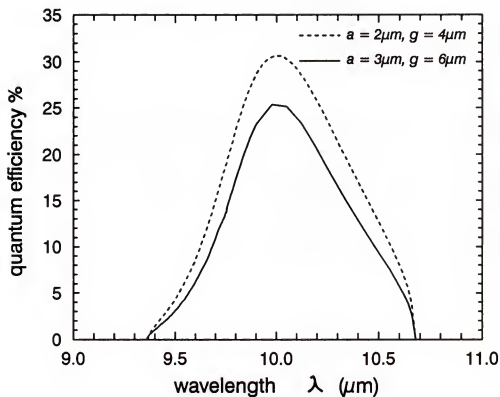


Figure 4.5(b) The coupling quantum efficiency corresponding to Fig. 4.5(a).

CHAPTER 5

EXPERIMENTAL IMPLEMENTATIONS OF TWO DIMENSIONAL SQUARE APERTURE MESH METAL GRATING COUPLER

5.1 Introduction

Intersubband quantum well detectors have recently been the subject of a considerable research effort [74-77]; properties important for many applications are a wide spectral response [8], preferably over the atmospheric window 8-12 μm and tunability of the peak wavelength. From material viewpoint, this type of detector is simpler than the narrow band gap semiconductors and thus has been widely investigated for 10 μm detection. However, quantum well absorption takes place only if the electric field vector of the IR radiation has a component perpendicular to the quantum well layers [39,78,79]. This makes the detector insensitive to radiation entering in the direction normal to the detector surface plane. In contrast, a response in large area normal incident illumination is necessary for the fabrication of focal plane arrays. Therefore, varieties of coupling techniques have been employed, such as incorporating a 1-D linear grating coupler [15], a 2-D metal cross grating coupler [25], or polishing a 45° facet in one edge of the detector substrate [42]. A 2-D double period planar mesh metal grating possesses exclusive advantages over other techniques, which include (i) It effectively scatters the normal incident IR radiation with transverse electric field into a longitudinal electric field to improve the quantum well absorption independent of light polarization, (ii) It is easy to fabricate such a planar structure by metal deposition on the QWIP surface and thus avoids costly etching process.

In the grating design, the square aperture width ' a ' and grating period ' g ' are two key parameters which govern the coupling efficiency of the grating. It has been theoretically shown in Chapter 4 that the power coupling for such a planar grating structure is a function of the ratio of ' a ' to ' g ', which is so called 'strip factor'. Figure 4.1 shows that for an effective coupling, the value of strip factor ($h = a/g$) for a square aperture mesh metal grating must fall between 0.58 and 0.62. In this chapter, a study of experimental details in GaAs BTM QWIP optically enhanced by using the square aperture mesh metal grating couplers with parameters $g = 3.3\mu\text{m}$, $a = 2\mu\text{m}$ and $g = 4\mu\text{m}$, $a = 2\mu\text{m}$ under front and back side normal incidence illumination has been performed.

5.2 Sample Preparation

The detector device sample was grown by molecular beam epitaxy (MBE) technique. A $1\text{-}\mu\text{m}$ -thick highly n^+ -doped ($1.4 \times 10^{18} \text{ cm}^{-3}$) GaAs bottom contact layer was first grown on a lattice matched semi-insulating GaAs substrate. This is followed by the growth of 20 periods of enlarged $\text{In}_{0.07}\text{Ga}_{0.93}\text{As}$ quantum wells with a well width of 101\AA and a dopant density of $1.4 \times 10^{18} \text{ cm}^{-3}$. The barrier layers on each side of the quantum well consist of 5 periods of undoped $\text{Al}_{0.4}\text{Ga}_{0.6}\text{As}(24\text{\AA})/\text{GaAs}(55\text{\AA})$ superlattice layers which were grown alternatively with the InGaAs quantum wells. Finally, a second highly n^+ -doped ($1.4 \times 10^{18} \text{ cm}^{-3}$) GaAs cap layer of $0.4\mu\text{m}$ was grown on top of the QWIP to complete the structure and facilitate ohmic contact. The wafer was polished in SI GaAs substrate side. Arrays of square mesas of area $216 \times 216 \mu\text{m}^2$ were formed by etching device sample through the active layers down to the bottom contact layer. Following this, a square ring-shaped metal contact with $9\mu\text{m}$ width of AuGe/Ni/Au was deposited around the periphery of the mesa and alloyed for ohmic contact formation as shown Fig. 5.1.

The contact lithography utilizing a Suss MJB3 G-line mask aligner with 320-nm exposure and commercially produced photomask was employed for pattern definition.

The postexposure thickness $1.6\mu\text{m}$ positive polarity photoresist Shipley AZ-1450J was applied according to manufacturer's specifications. The undiluted Shipley MFI 319 was chosen as the developer. The first mask used to generate the detector mesas is transparent except for the align marker and mesa area. After developing and postbaking, the sample with mesa pattern was immersed in an $\text{H}_2\text{O}-\text{H}_3\text{PO}_4-\text{H}_2\text{O}_2$ solution for mesa etching. The second mask used for forming the detector metal contact is opaque except the top ring-shape contact and bottom common ground contact area. The $500\text{\AA}-\text{Au}_{0.88}\text{Ge}_{0.12}$, $150\text{\AA}-\text{Ni}$ and 850\AA , 99.99%-purity Au are in turn evaporated direct onto the contact pattern formed sample. A 3.5 minutes, 450°C thermal annealing was finally applied to the detector sample.

5.3 Grating Fabrication

In this section, we describe the photolithographic fabrication of the gold film grating. The grating grid is designed to have $2\mu\text{m}$ by $2\mu\text{m}$ aperture dimension on a $3.3\mu\text{m}$ double periodicity. The photomask is made of Chromium patterns on glass with fifty four periods of grating grids in each detector cell. The metal grating were located within the interior of the ring-shaped contact by pure gold deposition on the Si-doped GaAs top contact surface followed by the metal lift-off technique. High resolution Shipley System 812 photoresist is adopted for generating grating pattern. Since the dots in the grating pattern are really tiny, maximum adhesion is required, which can be achieved only on a clean, dry sample surface. Typically, the wafer was coated with photoresist within 30 minutes following a dehydration bake of greater than 125°C . Before priming the 812 photoresist, a standard adhesion promoter hexamethyldisilane (HMDS) was coated on the wafer by a Headway Research spinner in a 3750 rpm spin speed. The photoresist was dispensed on the wafer and spun in a 4400 rpm speed to achieve $1.2\mu\text{m}$ nominal coating thickness. Eight minutes softbake was applied in a convection oven set at 105°C to reduce the casting solvent content and to promote adhesion. After this softbaking, photoresist film was exposed

with the UV light source in the complementary pattern photomask. For optimum performance, the Shipley MFI 321 diluted by deionized water in the ratio of three to one was adopted as the developer. The 99.99% purity gold film of $850\text{-}\text{\AA}$ was then evaporated onto the the well-collimated grating pattern by an electron beam gun. The gold film covered sample was finally immersed in acetone in an ultrasonic cleaner to stripe the remaining resist, unwanted metal and leave the desired grid geometry delineated. Subtracting the area of contact ring and bonding pad, the grating active area of the detector is $26400\text{ }\mu\text{m}^2$.

5.4 Theory

Figure 5.1 shows the 2-D square aperture mesh metal grating on top surface of a GaAs step-BTM (SBTM) QWIP. The grating is characterized by the parameters of square aperture width $a = 2\mu\text{m}$ and grating period $g = 3.3\mu\text{m}$. The IR radiation is incident normally on the grating coupled QWIP. The square apertures are arranged in a square symmetry geometry. The combination of normal incidence and square symmetry ensures that the grating coupling are independent of polarization. To model the unknown electromagnetic waves near the grating, two sets of orthonormal functions, Floquet mode $\vec{\Phi}_{pqr}$ and waveguide mode $\vec{\Pi}_m$ spanned by the square aperture, were employed [59] as linear independent bases as described in Chapter 3 and 4. The absorption constant α of a QWIP depends on $\cos^2 \gamma$ [80], where γ is the absorption angle. In accordance with this, only propagating TM Floquet modes of the grating scattered field is eligible for the intersubband absorption [15]. A larger value of $\cos^2 \gamma$ implies a larger absorption constant. Besides, the coupling quantum efficiency of the grating coupled QWIP depends not only on γ but also on the power of effective propagating waves (namely, higher order TM Floquet modes) which can be expressed by

$$\eta = \sum_i \mathcal{P}_i (1 - e^{-\alpha_i l}) \quad (5.1)$$

where \mathcal{P}_i is the normalized power of the i th order propagating TM mode, α_i is the corresponding absorption constant and l is the total length of doped QWs. In the present sample, $l = (101\text{\AA}) \times (20 \text{ periods}) = 2020\text{\AA}$. The relative power and absorption angle of the first two order diffracted waves varying with wavelength λ are plotted in Fig. 3.6. The second order diffracted waves begin to propagate while λ is smaller than $9.2\mu\text{m}$ (using refractive index $n_r = 3.25$ for GaAs at 77 K). In the figure, the i th order absorption angle γ_i is the quantity used to calculate the absorption constant α_i . By substituting the diffracted power \mathcal{P}_i in Fig. 3.6 and the corresponding α_i into Eq. (5.1), the absorption constant is plotted in Fig. 5.2. A coupling quantum efficiency of 29% is obtained at $\lambda = 10.4\mu\text{m}$ under backside normal incident illumination for the GaAs BTM QWIP coupled with $g = 3.3\mu\text{m}$, $a = 2\mu\text{m}$ square aperture mesh metal grating. It is worthy of noting that the coupling quantum efficiency can be further improved by choosing a smaller grating period. According to the numerical analysis in Chapter 4, the optimum grating coupler has the normalized parameters $\frac{\lambda_p/n_r}{g} \approx 1$, > 1 , and $a/g = 0.6$, where λ_p is the peak absorption wavelength. Therefore, a grating with parameters $g = 3\mu\text{m}$ and $a = 1.8\mu\text{m}$ should yield a maximum coupling quantum efficiency for this GaAs SBTM QWIP.

5.5 Optical Measurement

The photocurrent measurement was carried out by a global source, a ORIEL 77250 single grating monochromator, a current preamplifier and a chopped lock-in amplifier combination. This lock-in chopper technique is employed to enhance the signal and block out the noise for narrow band detection, which greatly improve the sensitivity of the measurement system. In addition, the single grating monochromator is used to pass the desired wavelength of the IR source. In order to eliminate the background radiation, the IR light source is modulated by a chopper at certain frequency and the detected modulated signal is sent to the lock-in amplifier with the chopper's phase. The lock-in amplifier functions as both a phase sensitive detector and a narrow

bandwidth amplifier which amplifies only the signal at chopper's frequency and filters out the unmodulated signal. Higher frequency will lower the incident power accessing to the detector.

A bias voltage is required for the photoconductive operation QWIPs. On the other hand, noise is the limit of small signal detection in the applications of long wavelength QWIPs. The noise current from the TTL power supply may be too large to dominate the total noise current. To solve this, the battery will be a much better choice for voltage source because of its low noise level in comparison with that of a TTL power supply. To supply the desired bias voltage an operation amplifier circuit of OPAMP LF356 including a variable resistance is employed. The QWIP was connected to the invert terminal, and the bias voltage is fed into the noninvert input of the OP AMP through a voltage divider. The invert input will show up the same bias voltage as the noninvert input because of the virtual ground between both the OP AMP inputs.

The sample was mounted in the cold head by specially machined sample holder inside a liquid helium closed-cycle cryogenic system. The dewar temperature was measured with a Si thermocouple beneath the cold head. From this photocurrent measurement, together with the measurements of the incident light intensity on the sample position by using a calibrated pyroelectric detector, the responsivity varying with wavelength is obtained.

5.6 Results and Discussion

The intensity of light source in long wavelength becomes smaller, as a result, the measured photocurrent of the detector becomes noisier. A slight wavelength shift of the experimental data with respect to the theoretical calculation is found in Fig. 5.3, since that the theory used to calculate the absorption constant α deals with the zero-biased quantum wells. The internal responsivity of the QWIP was calculated

by substituting the coupling quantum efficiency given in Eq. (5.1) into the following expression

$$R_I = \eta g_o \frac{\lambda}{1.24} \quad (5.2)$$

where the optical gain $g_o = 0.2$ was obtained from the noise gain measured at 77K by the assumptions that these two gains are equal. The bias voltage $V_b = -2.5V$ in Fig. 5.3 implies the top contact is connected to the negative polarity of the battery. Operation at a higher bias voltage is unnecessary in order to avoid a large dark current. The grating coupler with parameter $g = 3.3\mu m$, $a = 2\mu m$ shows a larger responsivity than that of 45° angle edge detector. The measured responsivity $R_p = 490 mA/W$ at peak response wavelength $\lambda_p = 10.4\mu m$ is slightly smaller than that of calculated value. This may be attributed to the fact that the conductivity of the metal grating (Au) in QWIP device is smaller than the theoretical value of infinity. The current loss in conducting mesh metal grating will certainly lower the value of responsivity R_I measured in real QWIP device.

In order to illustrate the effect of grating period in the light coupling, the responsivity of a QWIP coupled with $g = 4\mu m$, $a = 2\mu m$ grating is also shown in Fig. 5.3. For this set of grating parameters the coupling characteristic curve is drawn in Fig. 3.6(a), a peak coupling strength occurred at $\lambda = 12.7\mu m$ and fading out in the shorter wavelength. Therefore the responsivity of QWIP coupled with $g = 3.3\mu m$, $a = 2\mu m$ is larger than that with $g = 4\mu m$, $a = 2\mu m$. The measured data shown in Fig. 5.3 verify the effect in responsivity by grating parameters predicted in Fig 3.6.

According to our previous calculations in Chapter 3, the responsivity of a GaAs QWIP under back side illumination is 2.34 times higher than that under front side illumination. This calculations are based on the assumptions that the impedance Z_{sub} looking from the detector substrate surface into the quantum well region is equal to $Z_0/3.25$ making the reflectivity at the substrate-air interface is equal to

0.28. However, the adding of the 2-D square aperture metal grating on top of the SBTM QWIP changes Z_{sub} drastically and exacerbates the light coupling. From the experimental results, an estimated reflectivity at the substrate-air interface is equal to 0.5, that is, 50% of the incident power will be reflected back to the air for a back side illuminated SBTM QWIP with a 2-D metal grating on top. As a result, a designed coating layer is suggested here to improve the back side light coupling for this grating coupled QWIP.

5.7 Conclusion

In conclusion, we have performed a experimental study of the coupling quantum efficiency and spectral responsivity in a 2-D square aperture mesh metal grating coupled GaAs SBTM QWIP under normal incident illumination. The coupling efficiency depends on the grating period g and square aperture width a . The measured coupling quantum efficiency for a GaAs BTM QWIP was found to be 29% with grating parameters $g = 3.3\mu\text{m}$ and $a = 2\mu\text{m}$. A further improvement in the responsivity can be achieved by using a grating with $g = 3\mu\text{m}$ and $a = 1.8\mu\text{m}$. To solve the strong reflection in back shining of the grating coupled QWIP, a suitable coating material is needed, which is expected to enhance the responsivity significant.

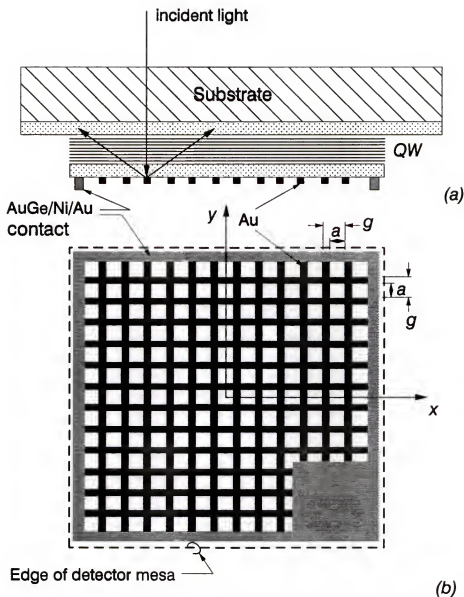


Figure 5.1 (a) Side view, and (b) top view show the grating diffraction, and the coordinates of a 2-D square aperture mesh metal grating coupler formed on top of a GaAs SBTM detector mesa.

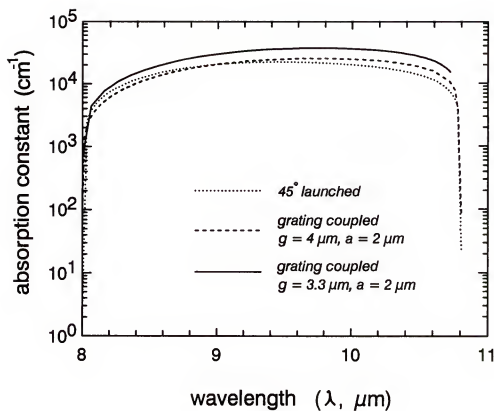


Figure 5.2 Absorption constant versus wavelength for a 2-D square aperture mesh metal grating coupled SBTM QWIP for two different grating periods and aperture sizes and for a 45° incident illumination. Where the absorption constant of the second order diffracted waves is not shown.

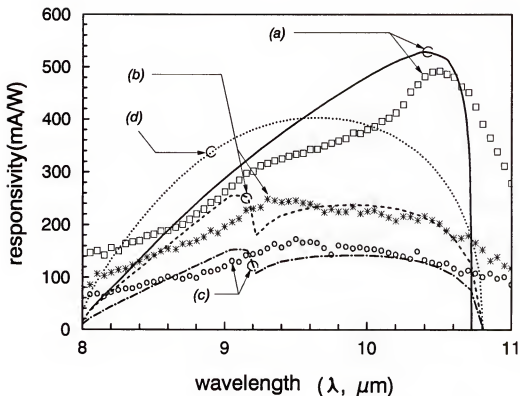


Figure 5.3 The responsivity of the 2D square aperture mesh metal grating coupled SBTM QWIPs measured at 77 K with an applied bias voltage $V_{bias} = -2.5V$. The curves represent (a) $g = 3.3\mu\text{m}$ and $a = 2\mu\text{m}$ under back side illumination, (b) $g = 4\mu\text{m}$ and $a = 2\mu\text{m}$ under back side illumination, (c) $g = 4\mu\text{m}$ and $a = 2\mu\text{m}$ under front illumination, and (d) launching at 45° polished facet, respectively. The discrete points are the measured data.

CHAPTER 6
DESIGN OF PLANAR 2-D CIRCULAR APERTURE
METAL GRATING COUPLER FOR GaAs
QUANTUM WELL INFRARED PHOTODETECTORS

6.1 Introduction

Long wavelength infrared detection by using intersubband optical absorption of semiconductor quantum well has been intensively studied in the last several years [81-84]. The excellent large area uniformity of GaAs/AlGaAs makes quantum well infrared photodetectors (QWIPs) ideal for 8 - 12 μm long wavelength infrared focal plane arrays (FPAs) applications. Recently, 128 by 128 large area preliminary detector arrays for 10 μm infrared imaging have also been demonstrated [85]. However, for n-type QWIPs the electric field vector of the incident light must have a component perpendicular to the quantum well layers in order to induce intersubband absorption [86,87]. Most works to date have been performed by shining light through a 45° polished facet on edge of the detector substrate [42], nevertheless, this coupling scheme allows only 1-D linear array. For image applications, planar arrangement of detectors and large area illumination are required. Coupling through a 1-D linear grating [18,21] on the QWIP may serve this purpose, however suffer from a low coupling efficiency due to its polarization selectivity. A double period 2-D metal grating [25,26,88,89] or random scattering roughened surface [28] on top of the QWIP can be employed to deflect the normal incident light into an absorbable angle independent of light polarization. In Chaps. 2 and 3 we have reported the design of 2-D square dot reflection metal grating [88] and 2-D square aperture mesh metal grating

[89] for n-type QWIP. The unique feature of these two metal grating coupler lies in the simplicity of its planar structure, which can be fabricated by simple lithography and metal deposition techniques. The possible nonuniformity in the dielectric etching for grating generating on the detector surface is thus eliminated, which greatly reduces the processing cost. From a fabrication viewpoint, the rectangular corners of the square apertures frequently turn smooth in grating pattern formation, which results in the grating structure distortion. On the other hand, no corner rounding will be observed in circular apertures. In this chapter we present a numerical and experimental study of planar 2-D circular aperture metal grating coupler on GaAs QWIPs. From the results shown in Chap. 3 that the grating coupled detector by back illumination performs better than that by front illumination. In the following discussions we consider the electromagnetic (EM) waves impinging on a QWIP under normal incident back illumination.

Light coupling is polarization independent for the circular aperture metal grating in either square symmetry (Fig. 6.1(a)) or hexagonal symmetry (Fig. 6.1(b)) arrangement. This is due to a high symmetry exists in the individual unit cell and cell arrangement of both grating structures. It has been shown that only TM components of the grating diffracted waves result in the intersubband transition in the quantum wells [17,60]. In addition, the quantum efficiency of a QWIP is a function of the total power and absorption angle of the higher-order TM diffracted waves. As shown in Fig. 6.1, under normal incident illumination, the normalized total power of each order diffracted waves depends on the 'normalized wavelength' $s = \lambda/g$ and the 'normalized aperture radius' $h = a/g$, where g is the grating period, λ is the *free space wavelength*, and a is the radius of the circular aperture. The absorption angle used in determining the absorption constant depends on the parameter ' s ' and the order of diffraction. From our numerical simulations, several universal plots of total power and absorption angle of higher-order TM diffracted waves versus s and h

are developed, which provide a convenient tools for designing circular aperture metal grating coupler on GaAs QWIPs.

6.2 Basic Theory

The periodicity of the grating scattering problems leads to a description of the fields in terms of the decomposition of their 2-D Floquet mode. Two integers p and q are denoted for the x and y spatial harmonics of the Floquet mode $\vec{\Phi}_{pq,r}$, and a third subscript r is used to denote TE or TM modes [90,91]. A unit power density EM wave is normally incident on the infinitesimally thin perfect conducting grating as shown in Fig. 6.1(c). The vector orthonormal mode functions for the TE and TM Floquet modes transverse with respect to \hat{z} can be expressed by

$$\begin{aligned}\vec{\Phi}_{pq1} &= G(\sin \phi_{pq}\hat{x} - \cos \phi_{pq}\hat{y})e^{-j(k_x^p x + k_y^{pq} y)} && \text{for TE modes} \\ \vec{\Phi}_{pq2} &= G(\cos \phi_{pq}\hat{x} + \sin \phi_{pq}\hat{y})e^{-j(k_x^p x + k_y^{pq} y)} && \text{for TM modes}\end{aligned}\quad (6.1)$$

where the normalized factor G can be written in terms of grating period g

$$\begin{aligned}G &= \frac{1}{g} && \text{for square symmetry} \\ &= \sqrt{\frac{2}{\sqrt{3}}}\frac{1}{g} && \text{for hexagonal symmetry}\end{aligned}\quad (6.2)$$

Besides, all field quantities are taken to have a time varying part of the form $e^{j\omega t}$, and the wave vectors k_x^p and k_y^{pq} in the x and y axes are given, respectively, by

$$\begin{aligned}k_x^p &= k \sin \theta_{pq} \cos \phi_{pq} = \frac{2\pi}{g}p \\ k_y^{pq} &= k \sin \theta_{pq} \sin \phi_{pq} = \frac{2\pi}{g}q && \text{for square symmetry} \\ &= \frac{2\pi}{\sqrt{3}g}(2q - p) && \text{for hexagonal symmetry}\end{aligned}\quad (6.3)$$

where θ_{pq} and ϕ_{pq} are the corresponding spherical coordinates for the wave propagating vector \vec{k} of (p, q) -order Floquet mode, and $p, q = 0, \pm 1, \pm 2, \dots, \pm \infty$. The z -direction wave vector k_z^{pq} depends on p and q , which is real for propagating modes, pure imaginary for evanescent modes. The boundary condition needs the tangential electric field vectors to be continuous within the circular aperture located at $z = 0$, that is

$$\sum_{r=1}^2 A_{00r} \vec{\Phi}_{00r} + \sum_{p,q} \sum_{r=1}^2 R_{pqr} \vec{\Phi}_{pqr} = \sum_{p,q} \sum_{r=1}^2 T_{pqr} \vec{\Phi}_{pqr} \quad \text{within the aperture} \quad (6.4)$$

where the first summation on the left-hand side is the expansion of the incident wave, A_{00r} is the magnitude of incident field component which depends on the polarization direction, R_{pqr} and T_{pqr} is the reflection coefficient and transmission coefficient of the Floquet mode, respectively.

The orthonormal waveguide modes $\vec{\Pi}_{mnl}$ that satisfy the aperture boundary condition on the circular aperture itself other than the Floquet modes $\vec{\Phi}_{pqr}$ are selected as the second set of linear independent basis to represent the unknown electric field distribution in the aperture. As a result, the transverse electric field vector is written as

$$\sum_{p,q} \sum_r T_{pqr} \vec{\Phi}_{pqr} = \sum_{m,n} \sum_l W_{mnl} \vec{\Pi}_{mnl}$$

with [92]

$$\vec{\Pi}_{mn1}(\rho, \psi) = \sqrt{\frac{2 - \delta_{0n}}{\pi}} \frac{1}{J_m(x'_{mn}) \sqrt{(x'_{mn})^2 - m^2}} \frac{x'_{mn}}{a} \left[\hat{\rho} \frac{m}{\frac{x'_{mn}}{a} \rho} J_m \left(\frac{x'_{mn}}{a} \rho \right) \begin{Bmatrix} \sin m\psi \\ -\cos m\psi \end{Bmatrix} + \hat{\psi} J'_m \left(\frac{x'_{mn}}{a} \rho \right) \begin{Bmatrix} \cos m\psi \\ \sin m\psi \end{Bmatrix} \right] \quad (6.5)$$

and

$$\vec{\Pi}_{mn2}(\rho, \psi) = \sqrt{\frac{2 - \delta_{0n}}{\pi}} \frac{1}{a J_{m-1}(x_{mn})} \left[\hat{\rho} J'_m \left(\frac{x_{mn}}{a} \rho \right) \begin{Bmatrix} \cos m\psi \\ \sin m\psi \end{Bmatrix} - \hat{\psi} \frac{m}{\frac{x_{mn}}{a} \rho} J_m \left(\frac{x_{mn}}{a} \rho \right) \begin{Bmatrix} \sin m\psi \\ -\cos m\psi \end{Bmatrix} \right] \quad (6.6)$$

where the prime superscript represents differential notation, a is the radius of the circular aperture, (ρ, ψ, z) are the cylindrical coordinates system used, $l = 1$ or 2 denotes TE or TM mode, respectively; J_m is the Bessel function of the first kind with order m , x_{mn} is the n th zero of $J_m(x)$ and x'_{mn} is the n th zero of $J'_m(x)$, δ_{0n} equals 1 for $n = 0$ and δ_{0n} equals 0 for $n \geq 1$. Assuming that the impedances looking into the quantum well region from $z = 0^-$ plane are equal to that of bulk GaAs, the modal impedances η_{pqr}^d and η_{pqr} for TE and TM waves on both sides of the grating can be easily derived. Employing method of moments, a set of linear algebraic equation with the mode coefficients W_{mnl} as unknowns can be obtained [59]

$$[Y_{mnl}^{MNL}] [W_{mnl}] = [I_{mnl}] \quad (6.7)$$

where

$$Y_{mnl}^{MNL} = \sum_{p,q} \sum_{\tau=1}^2 \left(\frac{1}{\eta_{pqr}^d} + \frac{1}{\eta_{pqr}} \right) C_{pqr}^{MNL*} C_{pqr}^{mnl},$$

and

$$C_{pqr}^{mnl} = \int_0^{2\pi} \int_0^a \vec{\Phi}_{pqr}^*(x, y) \cdot \vec{\Pi}_{mnl}(\rho, \phi) \rho d\rho d\phi \quad (6.8)$$

Both Y_{mnl}^{MNL} and C_{pqr}^{mnl} depend on grating geometry, and I_{mnl} is the matrix depending on incident waves. A principal difficulty in calculating C_{pqr}^{mnl} by numerical integral is the limitation of CPU time. To solve this, a closed-form analytical expression of the vector function inner product C_{pqr}^{mnl} is found in Appendix A. The higher-order TM reflection coefficients R_{pq2} are given by Eq. (3.11). The normalized power \mathcal{P}_{pq2} associated with TM reflected wave diffracted into the given order (p, q) is given by Eq. (2.14). Since R_{pqr} is a function of λ/g for a given h , the normalized power \mathcal{P}_{pq2} is, also a function of λ/g . The angle between the electric field vector of the higher-order TM reflected modes $R_{pq2}\vec{\Phi}_{pq2}$ and the \hat{z} direction is defined as absorption angle γ_{pq2} , and the cosine of this angle depends on the order of diffraction and the normalized wavelength s ($= \lambda/g$), which is given by

$$\cos \gamma_{pq2} = \frac{s}{n_r} \sqrt{p^2 + q^2} \quad \text{for square symmetry}$$

$$= \frac{s}{n_r} \frac{2}{\sqrt{3}} \sqrt{p^2 + q^2 - pq} \quad \text{for hexagonal symmetry} \quad (6.9)$$

where n_r is the refractive index of the detector medium, and $n_r = 3.25$ for GaAs at 77 K.

6.3 Results and Discussion

In typical computations, the lowest 52 waveguide modes and 5000 Floquet modes with $2\pi/g\sqrt{p^2 + q^2} \leq 25k$ were included. The addition of more higher-order modes made no noticeable change in the transmission or reflection coefficients, which demonstrates the accuracy of the numerical results. The problem under consideration here is a unit power density EM wave impinges normally onto the 2-D metal grating, as shown in Fig. 6.1(c). The effective coupling of IR radiation into the QWIP is due to nonzerth-order reflected TM Floquet modes, because the TE Floquet modes have an absorption angle $\gamma = 90^\circ$ and the evanescent modes produce no photo-signal in intersubband absorption [17,60]. In order to develop the generalized relationship of the 2-D circular aperture metal grating coupler for QWIP, two normalized grating parameters, $s = \lambda/g$ and $h = a/g$, were employed to facilitate illustration.

6.3.1 Square Symmetry Grating Structure

Figure 6.2 shows the first universal plot, which illustrates the normalized total power of the first-order TM diffracted waves $R_{012}\tilde{\Phi}_{012}$, $R_{0-12}\tilde{\Phi}_{0-12}$, $R_{-102}\tilde{\Phi}_{-102}$ and $R_{102}\tilde{\Phi}_{102}$ as a function of s for different values of h . The first-order diffracted waves become propagating when the wavelength of the IR radiation in GaAs is smaller than the grating period, i.e., $s = \lambda/g < 3.25$. Within the spectral range in Fig. 6.2, only (0,0) order transmitted waves $T_{00i}\tilde{\Phi}_{00i}$ ($i = 1, 2$) might be found in the far field, and all the other higher-order transmitted waves were evanescent modes because the wavelength in the air side is much greater than g . In addition, the square symmetry arrangement makes the grating indistinguishable between x and y directions. The total normalized power of the first-order diffracted waves generated

by x and y components of the incident waves remains the same for different incident polarizations. In other words, the coupling of the grating is polarization independent. The second-order diffracted waves are excited by the grating when $s < 2.298$ with a total power about 50% smaller than that of the first-order diffracted waves. Figure 6.3 illustrates the normalized total power of the second-order TM diffracted components $(\pm 1, 1)$ and $(\pm 1, -1)$ as a function of s for various values of h . A comparison of Figs. 6.2 and 6.3 reveals that the grating which excites a larger power of the first-order diffracted waves will prohibit that of the second-order diffracted waves.

During the grating fabrication, the grating period g is certainly invariant while the aperture radius a may be varied. Take this into consideration, a figure relates the total power of the first-order diffracted waves to $h = a/g$ within the most effective coupling regime $2.8 \leq s \leq 3.2$ is plotted in Fig. 6.4. From the figure, it is noted that the coupling of grating with aperture ratio $a/g = 0.36$ not only is insensitive to the variation of aperture radius but also maximizes the normalized diffracted power \mathcal{P}_{eff} , which implies that $a/g = 0.36$ is the optimum aperture radius for the square symmetry metal grating.

6.3.2 Hexagonal Symmetry Grating Structure

In the next set of figures, namely Figs. 6.5, 6.6, we have the same incident conditions as in Figs. 6.2, 6.4 but the grating has the hexagonal symmetry arrangement. Figure 6.5 shows the universal plot illustrating the normalized total power of the first-order TM diffracted waves as a function of s for different values of h . The six first-order diffracted waves $(\pm 1, 0)$, $(0, \pm 1)$ and $(\pm 1, \pm 1)$ begin to propagate at $s/3.25 = \sqrt{3}/2$. The six second-order TM diffracted waves $(\mp 1, \pm 1)$, $(\pm 1, \pm 2)$ and $(\pm 2, 1)$ propagate only for $s < 1.625$ with a total power about one tenth of that of the first-order diffracted waves. It should be noted that the total power of each order diffracted waves is independent of incident polarization. The figure relates the total power of the first-order diffracted waves to h within the most effective coupling

regime $2.4 \leq s \leq 2.7$ is plotted in Fig. 6.6. The optimum normalized radius for the hexagonal symmetry metal grating is obviously $a/g = 0.31$.

6.3.3 Comparison between Experiment and Theory

By comparing Figs. 6.2 and 6.5 it is found that a maximum coupling efficiency of square symmetry grating is about 1.08 times larger than that of hexagonal symmetry grating. on the other hand, the latter has a 1.44 times wider available bandwidth (i.e., the band between the normalized wavelength at which the first and second diffracted waves begin to propagate) than that of the former.

The grating coupled GaAs QWIP used in present analysis is composed of 20-period GaAs multiquantum well superlattice, having a well width of 40\AA , a dopant density $1.2 \times 10^{18} \text{ cm}^{-3}$, and a undoped 480\AA barrier of $\text{Al}_{0.25}\text{Ga}_{0.75}\text{As}$. In this QWIP, the peak absorption wavelength is $10 \mu\text{m}$ and the photocurrent through the QWIP is generated by the 2-D electrons move in the continuous band in the direction perpendicular to the quantum well layers. The circular aperture mesh metal grating coupler used in our experiment has the square symmetry arrangement as discussed in Section 6.3.1. For effective coupling, the period of the grating is selected so that the QWIP absorption band falls in the region between $s = 2.298$ and $s = 3.25$ by using the first-order TM diffracted waves. Figure 6.7 shows the coupling characteristic curve for the 2-D square symmetry grating with $g = 3.3\mu\text{m}$, $a = 1\mu\text{m}$, or $a/g = 0.6$, which was obtained by multiplying the grating period $g = 3.3\mu\text{m}$ to the abscissa of curve $a/g = 0.6$ in Fig. 6.2. The cut-off wavelength is $10.725\mu\text{m}$ for this grating coupler and $9\text{-}10.6 \mu\text{m}$ is the most effective coupling regime. The calculated responsivity R_I for the QWIP is given by

$$R_I = [\mathcal{P}_{eff}(1 - e^{-\alpha l})] g_o \frac{\lambda}{1.24} \quad (6.10)$$

where \mathcal{P}_{eff} is the effective coupling power of the IR radiation; l is the total length of the doped quantum wells, and the terms in the square brackets is the expression of quantum efficiency η . In present case, \mathcal{P}_{eff} is the normalized total power of the

first-order TM diffracted waves, and $l = (40\text{\AA}/\text{period}) \times (20 \text{ periods}) = 800\text{\AA}$. The optical gain $g_o = 0.603$ at bias $V_b = -1\text{V}$ (mesa top negative) is estimated using the 45° edge-illuminated detector. The intersubband absorption constant is calculated by [10]

$$\alpha = \cos^2 \gamma \frac{|M|^2}{137n_r} \frac{\hbar\omega kT}{\sqrt{E_0 + \hbar\omega}} \left(\frac{2m_b}{\hbar^2} \right)^{3/2} \ln \left[\frac{1 + e^{(E_F - E_0)/kT}}{1 + e^{(E_F - E_0 - \hbar\omega)/kT}} \right] \quad (6.11)$$

where γ is the absorption angle given in Eq. 6.9 or Fig. 6.7, n_r is the bulk refractive index, ω is the angular frequency of photons, m_b is the effective mass in the AlGaAs barriers, E_0 is the ground state energy level in the quantum well, M is the envelop matrix element, and a 60% conduction band split is assumed [93]. The calculated responsivity for the grating coupled QWIP with $g = 3.3\mu\text{m}$ and $a = 1\mu\text{m}$ is shown as a solid line in Fig. 6.8, and the measured responsivity corresponding to this QWIP is shown by the square dots in curve (a) of Fig. 6.8. In this figure, the grating coupled QWIP with $a/g = 1\mu\text{m}/3.3\mu\text{m}$ has a quantum efficiency of 17.1% at $\lambda = 10.2\mu\text{m}$, which is 2.7 times higher than that of the 45° angle edge-illuminated detector. Besides, an excellent agreement between the theoretical calculations and the measured values of the responsivity for curve (a) of Fig. 6.8. In order to facilitate comparison, the measured responsivity for the grating coupled QWIP with $g = 4\mu\text{m}$ and $a = 1.1\mu\text{m}$ is also shown in Fig. 6.8 and labeled as curve (b). The responsivity for curve (b) is considerably lower than that of curve (a) at $10.2\mu\text{m}$ wavelength. This is due to the fact that using grating parameters $a/g = 1.1\mu\text{m}/4\mu\text{m}$ the grating coupling peak will shift to $12.6\mu\text{m}$ wavelength, which falls beyond the absorption band of this QWIP. In other words, the grating with $2.298 \leq s \leq 3.25$ covering the QWIP absorption band is a more effective IR detector coupler. In fact, by choosing an optimum grating coupler parameters with $g = 3.3\mu\text{m}$, $a = 1.2\mu\text{m}$ (i.e., $a/g = 0.36$), further increase in the responsivity at $10\mu\text{m}$ wavelength can be expected.

6.4 Conclusion

In conclusion, we have performed a numerical simulation and experimental analysis of spectral responsivity for a 2-D circular aperture mesh metal grating coupled GaAs QWIP. The total power and diffracted angle of the higher-order TM diffracted waves are shown to be related to two normalized parameters, namely, $s = \lambda/g$ and $h = a/g$, which are functions of wavelength and grating dimensions. The optimum grating period and aperture radius can be determined for any specific infrared spectrum by scaling the normalized parameters of the universal curves developed. The responsivity for such a grating coupled QWIP can also be calculated from these universal charts.

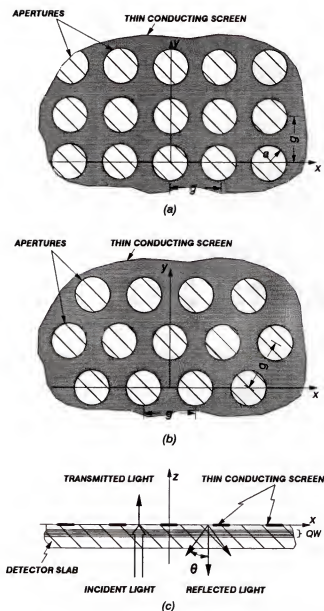


Figure 6.1 Top view of circular apertures mesh metal grating coupler with (a) square symmetry, and (b) hexagonal symmetry arrangement. (c) Side view showing the geometry of back illumination. Where g is the grating period and a is the radius of the circular aperture.

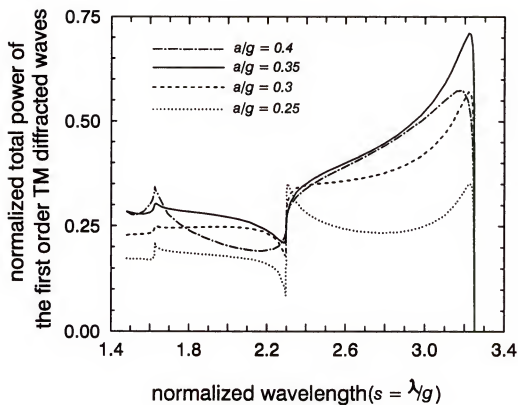


Figure 6.2 Normalized total power of the first-order diffracted waves of a square symmetry grating versus normalized wavelength s for different values of h .

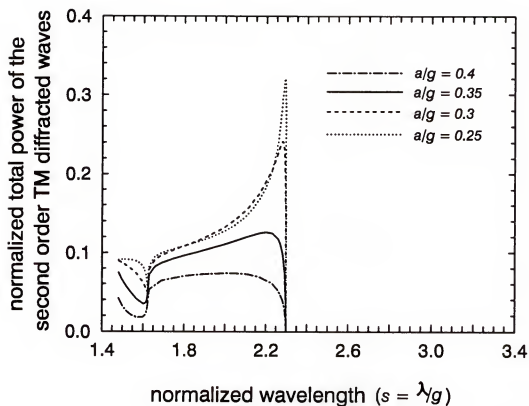


Figure 6.3 Normalized total power of the second-order diffracted waves of a square symmetry grating as a function of s for different values of h .

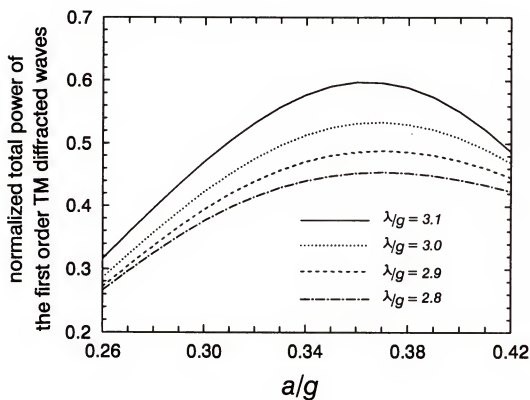


Figure 6.4 Total power of the first order diffracted waves versus a/g for a square symmetry metal grating coupler at different values of normalized wavelength s .

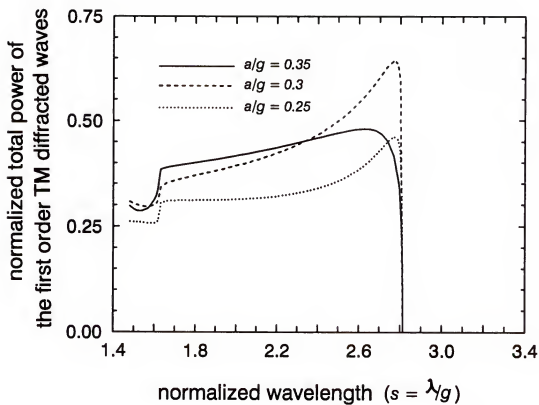


Figure 6.5 Normalized total power of the first-order diffracted waves of a hexagonal symmetry grating versus normalized wavelength s for different values of h .

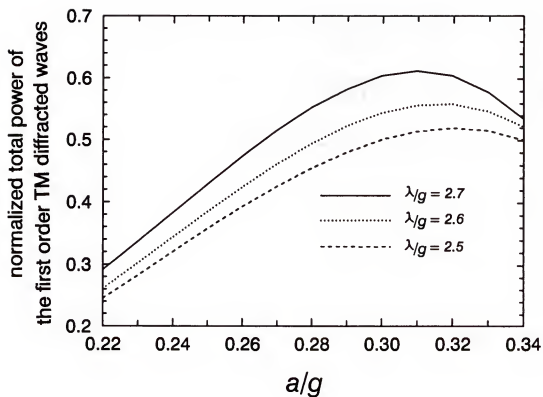


Figure 6.6 Total power of the first order diffracted waves versus a/g for a hexagonal symmetry metal grating coupler at different values of normalized wavelength s .

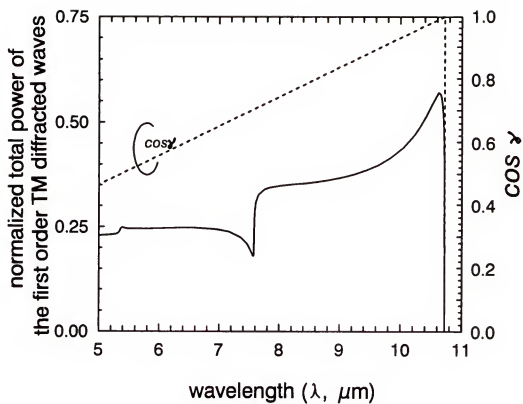


Figure 6.7 Coupling characteristic curve for the 2-D square symmetry metal grating with parameters $g = 3.3\mu\text{m}$, and $a = 2.0\mu\text{m}$.

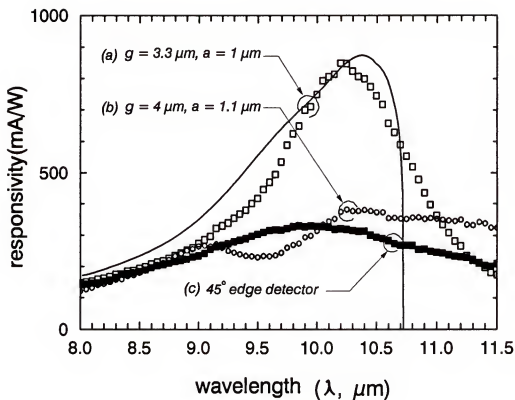


Figure 6.8 Spectral responsivity of the bound-to-continuum QWIP under various coupling scheme at bias voltage $V_b = -1\text{V}$; (a) square symmetry grating with $g = 3.3\mu\text{m}$, $a = 1\mu\text{m}$, (b) square symmetry grating with $g = 4\mu\text{m}$, $a = 1.1\mu\text{m}$, and (c) 45° polish edge.

CHAPTER 7

DESIGN OF AN OPTIMUM PERFORMANCE BTM QWIP

7.1 Introduction

Recent work on quantum well infrared photodetectors (QWIP) has demonstrated conclusively that these detectors can be implemented in wide band-gap materials as a result of the use of intraband processes rather than interband processes [94]. The quantum well structures involving such a low-energy transitions utilized for direct long-wavelength photon detection leads to both low-voltage operation and possible superior performance over comparable photodetectors based on conventional interband concept [95]. The potential advantages for GaAs QWIPs over conventional HgCdTe detectors in the long-wavelength infrared spectral region (LWIR, 8-14 μm) include more mature materials growth and processing technology with greater uniformity, larger substrate area available and well-developed passivation skills, possibility of monolithic integration with GaAs CCDs and signal processing electronics (and even Si electronics with GaAs on Si growth [83]), better thermal stability, radiation hardness, and inherent high speed with advantages for ranging. Several of these attributes are particularly desirable for large area image arrays. A detailed understanding in the design procedure of GaAs/AlGaAs quantum well detectors is, however, necessary, since the principle of this type of detector is easy to extend to other wide bandgap materials system such as InGaAs/InAlAs and Si/SiGe [82,84,96]. The former is capable of covering the complete medium wave infrared band (MWIR, 3-5 μm). By using the latter, more straightforward integration of signal processing functions could be achieved by silicon-based technology.

In this chapter, we describe a theoretical and experimental study of the procedures for optimizing the performance of a BTM QWIP. The effects of the design parameters in QWIP performance including barrier height, barrier width, quantum well doping concentration, quantum well period, and waveguide layer thickness are discussed. The results provide intuitive and quantitative approaches to improve the performance of bound-to-miniband (BTM) GaAs QWIPs.

7.2 General Consideration of a BTM QWIP

The ability to control the IR spectral bandwidth by varying the quantum well parameters is a key feature for the QWIP devices. The bound-to-continuum (BTC) and BTM transition QWIPs are the two QWIP structures which have been developed for the LWIR focal plane arrays applications. By varying the well width and compositionally controlled barrier height, the response wavelengths of the intersubband transitions in these QWIPs can be readily changed over a wide range of MWIR and LWIR spectrum. Although the structures are quite different, the operation of BTC QWIP is very similar to that of a BTM QWIP [79]. The infrared radiation is absorbed in the doped quantum wells, exciting an electron from the highly populated ground state and transporting via the miniband or continuum states until it is collected at the electrodes or recaptured into another quantum well. The main difference in the operation of these two types of detectors is that the transport occurs in the high-mobility continuum state above the barriers for the BTC QWIP, while transport is via the global miniband states inside the quantum well for the BTM QWIPs.

The use of superlattice barrier layer in a BTM QWIP increases the barrier height and forms a miniband inside the quantum well. This could lead to a significant reduction of the thermionic emission dark current over the barrier, and hence permit the raising of operation temperature for the QWIP. Higher temperature operation is desirable for practical applications of BTM QWIP in LWIR detection and focal plane arrays. In a BTM QWIP, the superlattice barriers can be made thin to allow the

formation of low-lying minibands corresponding to long wavelength, and, to facilitate the transport of carriers through the superlattice. Under small bias voltage, the photocurrent is mainly attributed to the tunneling between wells and can be controlled by varying the barrier thickness of the superlattice well, i.e., thin and high barriers allow us broadband detection with lower dark current. It is also worth noting that for photoconductive detectors, the absorption spectrum is found to be much broader for BTC than for BTM transitions [98,99]. As a result, the absorption constant of the former is significant smaller than that of the latter.

7.2.1 Barrier Height and $\text{Al}_x\text{Ga}_{1-x}\text{As}$ Composition

To reduce the dark current of a QWIP, a higher barrier height is needed for the quantum well. For $\text{GaAs}/\text{Al}_x\text{Ga}_{1-x}\text{As}$ BTM QWIPs, this can be achieved by choosing the aluminum composition x to be 0.38, which would yield a barrier height of 283 meV for the GaAs quantum well. The well width is determined so that there are two subband levels in the quantum well with energy separation equals to the photon energy corresponding to an intersubband transition peak wavelength of around $10\mu\text{m}$ after taking the exchange energy into consideration [61,62]. The structure described here and illustrated in Fig. 7.1 is thus composed of 93\AA GaAs quantum wells with two bound-state located at E_{W1} , $E_{W2} = 35,140$ meV above the conduction band edge of GaAs quantum well, respectively.

7.2.2 Superlattice Barrier Width

By using a short period superlattice of $\text{Al}_{0.38}\text{Ga}_{0.62}\text{As}/\text{GaAs}$ as barrier layer for the BTM QWIP, the width of superlattice well is determined so that only one bound-state exists in the superlattice well, which overlaps with the second bound-state of the quantum wells and creates a global miniband for carrier transport. A well width of 28\AA for the GaAs superlattice well meets this requirement. The spectral response bandwidth depends on the barrier width of the superlattice wells [32]. For example, for a $2\mu\text{m}$ FWHM absorption bandwidth, the barrier width of the superlattice well

is chosen to be equal to 49\AA , and a miniband width of 19 meV width is obtained for such a BTM QWIP.

A dramatic improvement in the QWIP performance is achieved by increasing the total barrier width from $l_b = 300\text{\AA}$ to 500\AA [34]. This is due to a strong reduction in thermally assisted tunneling, which leads to a large reduction in dark current. Further increase of barrier width gives virtually the same detectivity D^* [28]. Since the reduction in tunneling due to the thicker barriers (reduce dark current I_D) is partially compensated by the necessity of using higher bias voltage (increase I_D) to increase gain. For this reason, seven periods $\text{Al}_{0.38}\text{Ga}_{0.62}\text{As}(49\text{\AA})/\text{GaAs}(28\text{\AA})$ superlattice barrier layer is chosen as the optimum value, which yields a total superlattice barrier width of 511 \AA .

7.2.3 Doping Concentration in the Quantum Well

The detectivity of a QWIP is nearly constant over a broad doping concentration ($N_D = 10^{16}$ to 10^{18} cm^{-3}) range in the quantum well [28]. The fabrication of large area QWIP arrays can take advantage of this doping independent, since it implies that D^* will remain highly uniform across a large 2-D array even the doping varies across the wafer (for MBE growth, it is about 1%). On the other hand, filling of the charge storage wells in the multiplexer circuit by the dark current must be avoided, specially for large 2-D arrays. Therefore, it is advantageous to lower the doping concentration in the quantum well, which has essentially the same detectivity but substantially lowers dark current. However, the absorption intensity is directly proportional to N_D [32], lowering the doping will also reduce the absorption constant. a compromised doping concentration of $N_D = 7 \times 10^{17}\text{ cm}^{-3}$ is chosen for optimum performance. In the calculation of exchange energy [61,62], a ground state levels shifted downward from the conventional noninteracting state by 16 meV was found.

7.3 Quantum Well Period

Based on the photocarrier gain mechanism [100,101], the photocurrent gain g in a QWIP can be written as

$$g = \frac{L}{l} = \frac{L}{Nl_w + (N+1)l_b} \propto \frac{1}{N}, \quad (7.1)$$

where L is the hot-carrier recapture mean free path, l is the length of the multiquantum well region, l_w is the width of a single quantum well, l_b is the barrier width of the superlattice barrier, and N is the period of multiquantum wells. It is worth noting that a study by Stelle *et al.* [102] on a set of standard GaAs QWIPs with 4, 8, 16, and 32 quantum wells also found g is inversely proportional to N as predicted by Eq. (7.1). Increasing N in quantum well structure produces two opposing effects (i) the quantum efficiency η can be enhanced by increases N (larger l), since the absorption path increase, and (ii) reducing l can increase the gain be increased substantially, since there is a decrease in retrapping of photo-electrons into downstream wells. Therefore it is useful to study the effect of quantum well period on the responsivity, dark current, and detectivity of BTM QWIP. In this section we study the performance characteristics versus quantum well period for three step-BTM QWIPs composed of 20, 15, and 4 quantum well periods, labeled 20PD, 15PD and 4PD, respectively.

The 20PD multiquantum well structures consist of 101 \AA n-doped $\text{In}_{0.07}\text{Ga}_{0.93}\text{As}$ quantum wells with doping concentration $N_D = 1.4 \times 10^{18} \text{ cm}^{-3}$ and 5-period undoped $\text{Al}_{0.4}\text{Ga}_{0.6}\text{As}(30\text{ \AA})/\text{GaAs}(59\text{ \AA})$ superlattice barriers. The 15PD and 4PD QWIPs were obtained by etching the 20PD QWIP down to the sixteenth and fifth well region followed by AuGe/Ni/Au films deposition to form ohmic contacts. The dark current versus voltage characteristics at 77 K for these samples are shown in Fig. 7.2. Since the dark current in these detectors depends on the applied electric field [103] (i.e., the voltage drop per period), the bias voltage V_b needs to be converted to unit of electric field to take into account the number of barriers in each detector. For this reason, the bias voltage for the 20PD, 15PD and 4PD QWIPs are in the ratio of 21 : 16 : 5.

In present studies the spectral photoresponse was measured with a global, a 7-

15 μ m optical filter, grating monochromator, and a chopper lock-in amplifier system. The spectral responsivity of the three detectors, measured at 77 K and the same bias field (0.1 V/period) are shown in Fig. 7.3. It is interesting to note that the peak spectral responsivity for the 4PD, 15PD and 20PD QWIPs are almost identical which occurs at $\lambda_p = 10.5\mu$ m. The responsivity determined by comparison with a calibrated pyroelectric detector were found to be $R_I(4PD) = 0.38$ A/W (at $V_b = 0.5$ V), $R_I(15PD) = 0.41$ A/W (at $V_b = 1.6$ V), and $R_I(20PD) = 0.33$ A/W (at $V_b = 2.1$ V). The noise current i_n in these detectors was measured at $V_b = 0.1$ V/period. It is shown that i_n is limited by the shot noise of the dark current given by [100]

$$i_n = \sqrt{4eI_Dg\Delta f} \quad (7.2)$$

where Δf is the noise bandwidth. Combining the noise measurement and the dark current shown in Fig. 7.2 allows the experimental determination of gain as $g(4PD) = 1.211$, $g(15PD) = 0.196$ and $g(20PD) = 0.103$ at $V_b = 0.1$ V/period, respectively. To relate the responsivity R_I to quantum well period N , R_I is written by

$$R_I = \eta g \frac{\lambda}{1.24} = k_1 \frac{1 - e^{\alpha l_w N}}{N l_w + (N + 1) l_b} \quad (7.3)$$

where k_1 is a constant of N , α is the absorption constant, the numerator is proportional to quantum efficiency η , and the denominator is equal to the length of the multiquantum well region. The absorption constant is determined by measured responsivity, gain and those equations given in Reference 32. The calculated responsivity versus quantum well period N curves for the three step-BTM QWIPs is shown in Fig. 7.4. In this figure, the experimental data are labeled by discrete points; dashed line are the calculated curves. Similar to Eq. (7.3), the detectivity D^* can be expressed as

$$D^* = \frac{R_I}{i_n} \sqrt{A_d \Delta f} = k_2 \frac{1 - e^{\alpha l_w N}}{\sqrt{N l_w + (N + 1) l_b}} \quad (7.4)$$

where k_2 is constant of N and A_d is the detector area. The calculated and measured detectivity versus periods N are also shown in Fig. 7.4. The differences between

measured data and theoretical prediction can attributed to the uncertainty in etching process in the 4PD and 15PD formation. The exact etching depth is very difficultly to be determined by using the simple DEKTAK IIA depth profile measurements, which has an error range about $\pm 300\text{\AA}$ corresponding to one quantum well period. Nevertheless, the theoretical predictions has the same trend as those obtained directly from the measurements. Although the responsivity of the 4PD QWIP is larger than that of the 20PD QWIP, the noise in Eq. (7.2) is increased by the square root of the gain \sqrt{g} and the detectivity D^* is reduced by this same factor. As shown in Fig. 7.4, the optimization periods of this step-BTM QWIP is 20 periods, further increasing the period N has little effect on D^* . By this same procedure, the optimum period of the QWIP design in Section 7.2 is found to be 20.

7.4 Blocking Barrier and Dark Current

Using a 450\AA $\text{Al}_{0.16}\text{Ga}_{0.84}\text{As}$ layer adjacent to the end of superlattice barrier can effectively block undesirable tunneling carriers [104,105]. The quantum wells and the blocking layers are sandwiched between heavily doped GaAs contact layers. The doping concentration of the contact layer $N_D = 1.0 \times 10^{18} \text{ cm}^{-3}$ is a suitable density for ohmic contact formation. The blocking layer was designed so that the top of the barrier is lower than the bottom of the first excited-state, but much higher than the top of quantum well ground-state to block the flow of electrons (dark current) from the ground-state to the collector contact layer. This idea of employing such a blocking layer in a quantum well IR detector first appeared in the work by Coon *et al.* [106]. The performance improvement by the blocking layer can be seen from the reduction of electron transmission coefficient near the ground-state as shown in Fig. 7.5. The completed quantum well active region of the optimum designed GaAs BTM QWIP is thus shown in Fig. 7.1. The dark current density can be calculated by [103]

$$J = \frac{4\pi q m^* kT}{h^3} \int_0^\infty |T_r|^2 \ln \left[\frac{1 + e^{(E_F - E)/kT}}{1 + e^{(E_F - E - qV_b)/kT}} \right] dE \quad (7.5)$$

where V_b is the bias voltage across one period of the superlattice barrier, E is the electron energy, E_F is the Fermi level and T_r is the transmission coefficient. The dark current for the BTM QWIP of parameters given in Fig. 7.5 with blocking barriers is estimated to be below 10^{-6} A for bias voltage less than 0.4 V at $T = 83$ K.

7.5 Waveguide Structure

Using a 2-D planar metal grating can greatly enhances the intersubband absorption in QWIP under normal incident illumination. A further increase in the coupling quantum efficiency can be obtained by using a slab waveguide geometry QWIP. This structure is particularly effective for application where the total number of quantum wells is small [101]. In such a structure, the whole QWIP behaves as an optical waveguide, as shown in Fig. 7.6. The waves diffracted by the grating are confined in the transverse direction and guided along the longitudinal direction to let radiation pass the quantum well stack several times. The waveguide is formed by adding an internal reflecting layer beneath the QWIP active region to reflect the unabsorbed radiation back into the quantum well stack. The cladding layer and the top cap layer are positioned on each side of the quantum well stack. Aluminum arsenide of refractive index $n = 2.76$ is an adequate choice as a cladding layer of GaAs BTM QWIPs.

In this section we performed a numerical analysis of GaAs/AlGaAs grown infrared waveguide by using multi-slab waveguide mode theory [107]. For simplicity, we neglect the radiation loss by the metal grating and treat the waveguide without grating on top. As shown in Fig. 7.6, the index profile of the waveguide is assumed to be invariant in the direction of propagation, \hat{x} , which can be written as

$$\epsilon(y, z) = \epsilon_0 n^2(y, z) \quad (7.6)$$

where ϵ_0 is the permittivity of free space and $n(y, z)$ is the refractive index profile.

The electromagnetic field of the guided mode in the waveguide is expressed as

$$\vec{E}(x, y, z) = \vec{E}^0(y, z)e^{-j\beta x}$$

$$\vec{H}(x, y, z) = \vec{H}^0(y, z)e^{-j\beta x}$$

where the time dependence $e^{j\omega t}$ was omitted and β is the propagating constant of the mode. Due to the planar geometry of the waveguide QWIP, the guided fields are confined only to one direction, say \hat{z} , and are independent of the direction, \hat{y} , thus

$$\frac{\partial \vec{E}^0(y, z)}{\partial y} = \frac{\partial \vec{H}^0(y, z)}{\partial y} = 0$$

Besides, the planar waveguide supports two kinds of guided modes: TE mode has zero longitudinal electric field ($E_x = 0$), and TM mode has zero longitudinal magnetic field ($H_x = 0$). The field solution of TE modes are readily obtained by the field of TM modes according to the concept of duality,

$$\vec{E} \longrightarrow \vec{H} \quad \vec{H} \longrightarrow -\vec{E}$$

$$\epsilon \longrightarrow \mu \quad \mu \longrightarrow \epsilon$$

However, only TM modes cause intersubband absorption and are of major interest, therefore, the following discussion is focused on TM modes. First, we separate Maxwell equation into transversal component and longitudinal component as

$$\nabla_t \times \vec{E}^0(y, z) + j\omega\mu\vec{H}^0(y, z) = j\beta\hat{x} \times \vec{E}_t^0(y, z)$$

$$\nabla_t \times \vec{H}^0(y, z) - j\omega\epsilon\vec{E}^0(y, z) = j\beta\hat{x} \times \vec{H}_t^0(y, z)$$

There exists three field components H_y^0, E_x^0 and E_z^0 for the TM modes. After a comparison of components in three directions, the above two equations can be expressed in the following forms

$$\begin{aligned} x : \quad & \frac{\partial H_y^0}{\partial z} = j\omega\epsilon E_x^0 \\ y : \quad & \frac{\partial E_x^0}{\partial z} + j\beta E_z^0 = j\omega\mu H_y^0 \\ z : \quad & \beta H_y^0 = \omega\epsilon E_z^0 \end{aligned} \tag{7.7}$$

Setting $\mathcal{H} = H_y^0$ and $\mathcal{E} = \omega \epsilon_0 \epsilon_r E_x^0$ we have

$$\begin{aligned}\frac{d\mathcal{H}}{dz} &= j\mathcal{E} \\ \frac{d\mathcal{E}}{dz} &= -j(\beta^2 - n^2 k_0^2)\mathcal{H}\end{aligned}$$

where k_0 is free space wavenumber. Both \mathcal{H} and \mathcal{E} are scalar wave solution and obey the transverse wave equation

$$\mathcal{H}''(z) = (\beta^2 - n^2 k_0^2)\mathcal{H}(z) \quad (7.8)$$

The general solution of \mathcal{H} and \mathcal{E} are

$$\begin{aligned}\mathcal{H}(z) &= Ae^{j\gamma z} + Be^{-j\gamma z} \\ \mathcal{E}(z) &= \gamma Ae^{j\gamma z} - \gamma Be^{-j\gamma z}\end{aligned} \quad (7.9)$$

where A and B are constant of z , and

$$\gamma^2 = n^2 k_0^2 - \beta^2 \quad (7.10)$$

For one film, three-layer planar waveguide, we can solve the wave equation by setting the initial condition

$$\mathcal{H}_0 = \mathcal{H}(0)$$

$$\mathcal{E}_0 = \mathcal{E}(0)$$

at $z = 0$ and taking $\mathcal{H}(z)$ and $\mathcal{E}(z)/\epsilon_r(z)$ as continuous quantities in the \hat{z} direction, The result is a matrix expression as following

$$\begin{pmatrix} \mathcal{H} \\ \mathcal{E} \end{pmatrix} = M_1 \begin{pmatrix} \mathcal{H}_0 \\ \mathcal{E}_0 \end{pmatrix} \quad (7.11)$$

where

$$M_1 = \begin{pmatrix} \cos \gamma z & \frac{j\epsilon_r}{\gamma} \sin \gamma z \\ \frac{j\gamma}{\epsilon_r} \sin \gamma z & \cos \gamma z \end{pmatrix} \quad (7.12)$$

is the characteristic matrix. Extending this concept to m-layer waveguide with width d_i of each layer and

$$M_i = \begin{pmatrix} \cos \gamma_i d_i & \frac{z_{i1}}{\gamma_i} \sin \gamma_i d_i \\ \frac{z_{i1}}{\epsilon_i} \sin \gamma_i d_i & \cos \gamma_i d_i \end{pmatrix} \quad (7.13)$$

of each characteristic matrix, where $i = 1, \dots, m-2$, the characteristic equation of the QWIP waveguide system can be obtained by

$$\begin{pmatrix} \mathcal{H} \\ \mathcal{E} \end{pmatrix} = M_{m-2}|_{d_{m-2}} \cdots M_1|_{d_1} \begin{pmatrix} \mathcal{H}_0 \\ \mathcal{E}_0 \end{pmatrix}$$

For a guided mode, the electromagnetic fields in the substrate layer are evanescent wave and have the form

$$\mathcal{H}_s(z) = A e^{\alpha_s z}$$

$$\mathcal{E}_s(z) = -j\alpha_s A e^{\alpha_s z}$$

Similar to the electromagnetic field in the cap layer, thus

$$\mathcal{H}_c(z) = B e^{-\alpha_c(z-d_{m-2})}$$

$$\mathcal{E}_c(z) = j\alpha_c B e^{-\alpha_c(z-d_{m-2})}$$

where α_s and α_c are real number. The final matrix expression is given by

$$\begin{pmatrix} B \\ j\alpha_c B \end{pmatrix} = \begin{pmatrix} m_{11} & m_{12} \\ m_{21} & m_{22} \end{pmatrix} \begin{pmatrix} A \\ -j\alpha_s A \end{pmatrix} \quad (7.14)$$

and the dispersion relation for a multilayer slab waveguide used to solve the propagating constant β is

$$j(\alpha_c m_{11} + \alpha_s m_{22}) = m_{21} - \alpha_s \alpha_c m_{12} \quad (7.15)$$

The active region of the BTM QWIP under analysis has 20 period quantum wells with an intersubband absorption peak at 10 μm wavelength as shown in Fig. 7.1. The refractive index of GaAs, $\text{Al}_{0.38}\text{Ga}_{0.62}\text{As}$ and $\text{Al}_{0.16}\text{Ga}_{0.84}\text{As}$ were taken to be 3.25, 3.13 and 2.76, respectively [108,109]. Three parameters need to be determined are the thickness of the two contact layers and waveguide cladding layer. By adjusting

the width of cap and bottom contact layers, the position of maximum electric field intensity of the guided mode in the waveguide can be shifted. Figure 7.7 shows the electric field distribution of $10\text{ }\mu\text{m}$ guided wave propagating in the waveguide QWIP. From the figure, the cap layer must be thicker than the bottom contact layer to draw the unbalanced field distribution to its maximum field intensity occurring in the QWIP active region. The combination of $1.2\text{ }\mu\text{m}$ GaAs cap layer and $0.5\text{ }\mu\text{m}$ bottom contact layer would yield a much better performance than that of the combination of $0.5\text{ }\mu\text{m}$ cap layer and $1.0\text{ }\mu\text{m}$ bottom contact layer. The optimum widths of contact layers are thus determined.

The thickness of waveguide cladding layer was chosen to minimize total layer thickness without inducing excessive radiative mode leakage. From the present analysis, the cladding layer thickness to make the field dropping down to 10 % of its maximum intensity at the interface of quantum well/AlAs cladding layer is a reasonable thickness to ensure the residual waveguide loss within QWIP absorption band to be very small. From Fig. 7.7, a minimum $4\text{ }\mu\text{m}$ cladding layer is chosen to meet this requirement. Using the analysis of Section 7.3, the relative D^* versus quantum well period of the GaAs BTM QWIP with waveguide structure of parameters determined in Fig. 7.5 is shown in Fig. 7.8. From the figure, a detectivity maximum is observed at $N = 18$ for QWIP with waveguide, while, the maximum detectivity for QWIP without waveguide requires N larger than 40.

7.6 Conclusion

We have performed a theoretical and experiment study on the effects of device structure and parameters on the performance of the GaAs BTM QWIP. A BTM QWIP has the advantages over BTC QWIP in that it can effectively suppress the dark current as well as increase the absorption constant significantly by narrowing the absorption band. Since the dark current is controlled mainly by the barrier height, by adding a selective blocking layer the dark current can be further reduced. The doping

concentration of the quantum well has little effect on the QWIP detectivity. On the other hand, the detectivity can be improved by using a large number of quantum wells in the QWIP. From the present study, a quantum well period of 20 is the optimum period for the BTM QWIP with doping concentration of $5 \times 10^{17} \text{ cm}^{-3}$. Adding a $4 \text{ }\mu\text{m}$ AlAs cladding layer beneath the QWIP active region can greatly increase the coupling quantum efficiency. Increasing the width of the top contact layer to $1.2 \text{ }\mu\text{m}$ and decrease the bottom contact layer to $0.5 \text{ }\mu\text{m}$ ensures a maximum field intensity of IR radiation traveling in the QWIP active region. Using the optimized parameters described in this chapter, the D^* of the BTM QWIP can be increased by at least a factor of 2 over that of step-BTM QWIP without waveguide design and parameter optimization.

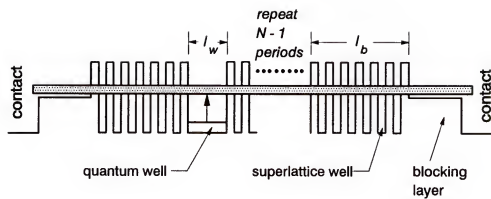


Figure 7.1 The energy band diagram of an N period BTM QWIP with quantum well width l_w , superlattice barrier width l_b and dark current blocking layers.

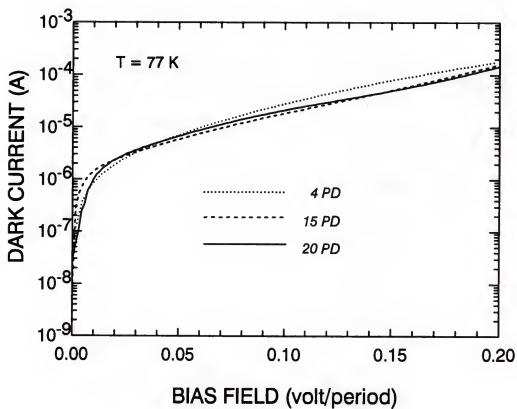


Figure 7.2 Dark current versus bias field for the 20PD, 15PD, and 4PD BTM QWIP of 208 μm square mesa measured at 77 K.

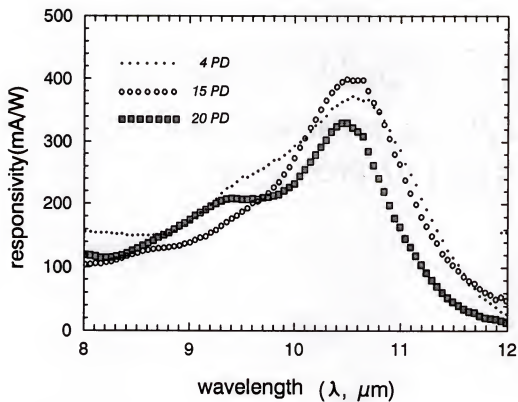


Figure 7.3 Spectral responsivity for the 20PD, 15PD, and 4PD QWIP measured at $V_b = -0.1$ V/period.

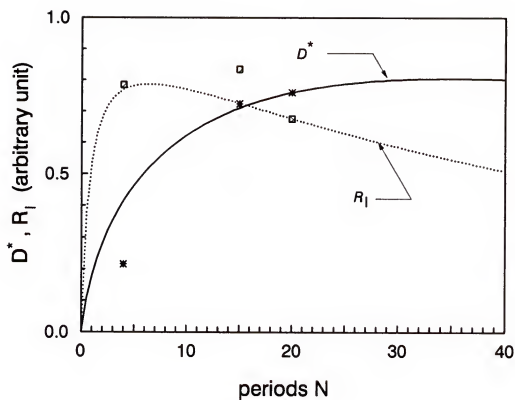


Figure 7.4 A comparison of the calculated and measured relative responsivity R_I and detectivity D^* versus quantum well period N for different period QWIPs without waveguide geometry, where the result of 20PD sample is taken as a perfect match point of theoretical calculations and measurements.

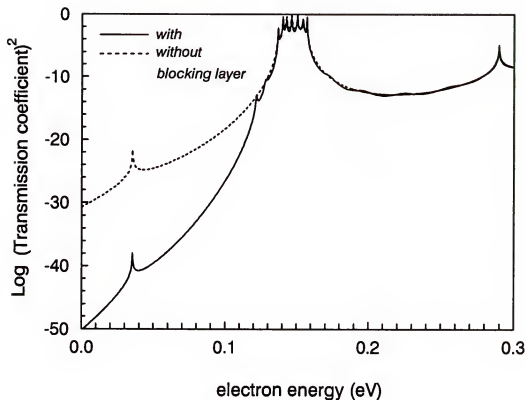


Figure 7.5 Calculated transmission coefficient $T_r^*T_r$ versus the electron potential energy E (eV) through the superlattice barrier. The QWIP consists of 20 periods $N_D = 7 \times 10^{17} \text{ cm}^{-3}$ doped quantum wells of 93 \AA . The barrier layer on each side of the quantum well consists of 6 period undoped GaAs (28 \AA)/ $\text{Al}_{0.38}\text{Ga}_{0.62}\text{As}$ (49 \AA) superlattice.

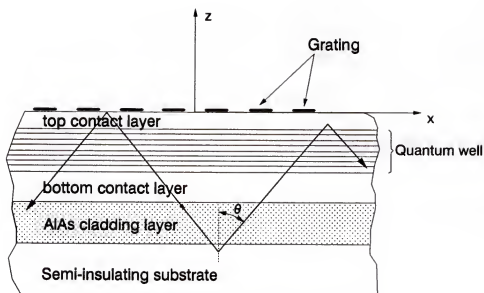


Figure 7.6 Side view of a waveguide geometry QWIP shows the wave propagating in the QWIP structure.

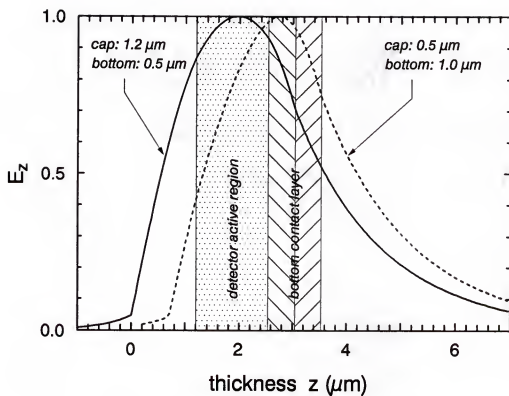


Figure 7.7 The electric field distribution of 10 μm wavelength guided wave versus the z axis for two sets of different thickness of cap and bottom contact layers.

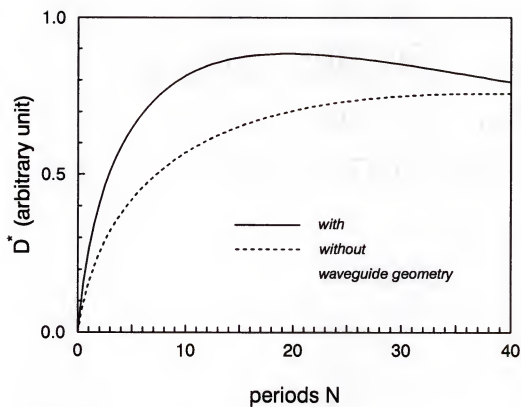


Figure 7.8 The theoretical prediction of detectivity D^* versus quantum well period N for the BTM QWIPs with and without waveguide geometry of parameters given in Fig. 7.4.

CHAPTER 8

SUMMARY

The GaAs QWIP becomes a very promising candidate for long wavelength infrared detection due to the mature and highly uniform III-V growth and processing technologies. In the detector image applications, an effective grating coupler is needed for coupling the normal incident infrared light into the n-doped quantum wells. In this work, we present three structures of 2-D planar metal grating couplers for QWIPs. The exclusive advantages of such grating couplers are (a) the coupling is independent of light polarization, (b) it is easy to fabricate by simple metal deposition. The first structure presented is the reflection square dot metal grating with a coupling efficiency of 20%. To improve the coupling efficiency, a 2-D square aperture metal grating is employed, which offers a higher efficiency up to 70%. That is, 70% normal incident infrared light can be transferred to TM mode for QWIP absorption. In the third structure, the 2-D circular aperture metal grating is introduced to avoid the difficulties encountered in grating fabrication, which achieves a 70% high coupling efficiency, too. In addition to the square symmetry arrangement required in the first two grating structures, the circular aperture metal grating provides one more hexagonal symmetry arrangement with a wider coupling bandwidth. In each of the developed structure, the optical properties of the metal grating were studied. The influences of grating shape and dimensions on the grating coupling efficiency is also discussed. The universal plots based on two normalized parameters λ/g and a/g offer an excellent design tool for determining the optimum grating dimensions.

A simple approach by separating grating coupling and QWIP absorption is de-

veloped to analyze the grating coupled QWIPs. The theory for grating diffraction relies on the modal expansion technique and the method of moments. A grating of infinite extension and perfect conductor is assumed. The numerical calculations gives a near-exact description in the diffracted power and diffracted angle of the 2-D planar grating. The selection rules of intersubband transition proposed that the absorption constant is governed by the polarization direction of the light. Together with the the diffracted power density, the coupling quantum efficiency η versus wavelength may be calculated. The η is a evaluation of QWIP performance for thermal imaging applications.

The detector quantum efficiency can be further increased by the use of waveguide geometry. The width of cladding layers as well as top and bottom contact layer for a QWIP waveguide is calculated. A theoretical and experimental analysis for quantum well period is studied, too. The optimum period for a structure specified QWIP provides a economical way to improve QWIP detectivity. In addition to the absorption enhancement by grating, waveguide, and optimum period, another critical issue related to QWIP performance is the dark current. The suppression of dark current may be achieved by a higher superlattice barrier and a selective blocking layer.

Several works remain to be done in this area. The experimental results of grating coupled QWIP shows a strong reflection at the detector substrate-air interface, which suggests that an appropriate coating film on the detector back surface can greatly improve the optical coupling. By thinning the substrate to several microns to change the impedance in the incident side is another approach for coupling improvement. Combining the dark current suppression and coupling improvement, the high sensitivity, large area QWIP FPA can be expected for a few years to come.

REFERENCES

- [1] K. W. Goossen and S. A. Lyon, "Performance aspects of a quantum-well detector," *J. Appl. Phys.*, vol. 63, pp. 5149-5153, 1988.
- [2] B. F. Levine, "Comment on 'Performance limitations of GaAs/AlGaAs infrared superlattices'," *Appl. Phys. Lett.*, vol. 56, pp. 2354-2355, 1990.
- [3] J. S. Smith, L. C. Chiu, S. Margalit, and A. Yariv, "A new infrared detector using electron emission from multiple quantum wells," *J. Vac. Sci. Technol.*, vol. B1, pp. 376-378, 1983.
- [4] B. F. Levine, S. D. Gunapala, and M. Hong, "Infrared intersubband photoinduced charge polarization in asymmetrical quantum wells," *Appl. Phys. Lett.*, vol. 59, pp. 1969-1971, 1991.
- [5] K. Brennan and Y. Wang, "Analysis of the two-dimensional dark currents in quantum well devices," *Appl. Phys. Lett.*, vol. 57, pp. 1337-1339, 1990.
- [6] F. L. Serzhenko and V. D. Shadrin, "Theory of photoelectric and threshold characteristics of photodetectors made of GaAs-AlGaAs multilayer quantum-well structures," *Sov. Phys. Semicond.*, vol. 25, pp. 953-958, 1991.
- [7] B. F. Levine, C. G. Bethea, K. K. Choi, J. Walker, and R. J. Malik, "Bound-to-extended state absorption GaAs Superlattice transport infrared detectors," *J. Appl. Phys.*, vol. 64, pp. 1591-1593, 1988.
- [8] B. F. Levine, C. G. Bethea, G. Hasnain, J. Walker, and R. J. Malik, "High-detectivity $D^* = 1.0 \times 10^{10}$ cm $\sqrt{\text{Hz}}/\text{W}$ GaAs/AlGaAs multi-quantum well $\lambda = 8.3\mu\text{m}$ infrared detector," *Appl. Phys. Lett.*, vol. 53, pp. 296-298, 1988.
- [9] E. Rosencher, E. Martinet, E. Böckenhoff, Ph. Bois, S. Delaitre, and J. P. Hirtz, "Normal incidence parallel intraband photoconductivity in GaAs/AlGaAs multi-quantum wells," *Appl. Phys. Lett.*, vol. 58, pp. 2589-2591, 1991.
- [10] Z. Ikončić, V. Milanović, and D. Tjapkin, "Bound-free intraband absorption in GaAs-Al_xGa_{1-x}As semiconductor quantum wells," *Appl. Phys. Lett.*, vol. 54, pp. 247-249, 1989.
- [11] C. P. Lee, K. H. Chang, and K. L. Tsai, "Quantum well infrared photodetectors with bi-periodic grating couplers," *Appl. Phys. Lett.*, vol. 61, pp. 2437-2439, 1992.

- [12] B. D. McCombe, R. T. Holm, and D. E. Schafer, "Frequency domain studies of intersubband optical transitions in Si inversion layers," *Solid State Commun.*, vol. 32, pp. 603-608, 1979.
- [13] D. C. Tsui, S. J. Allen, Jr., R. A. Lorgan, A. Kamgar, and S. N. Coppersmith, "High frequency conductivity in silicon inversion layers: drude relaxation, 2D plasmons and minigaps in surface superlattice," *Surf. Sci.*, vol. 73, pp. 419-433, 1978.
- [14] D. Heitmann and U. Mackens, "Grating-coupler-induced intersubband resonances in electron inversion layers of silicon," *Phys. Rev. B*, vol. 33, pp. 8269-8282, 1986.
- [15] K. W. Goossen and S. A. Lyon, "Grating enhanced quantum well detector," *Appl. Phys. Lett.*, vol. 47, pp. 1257-1259, 1985.
- [16] K. W. Goossen, S. A. Lyon, and K. Alavi, "Photovoltaic quantum well infrared detector," *Appl. Phys. Lett.*, vol. 52, pp. 1701-1703, 1988.
- [17] K. W. Goossen and S. A. Lyon, "Grating enhancement of quantum well detector response," *Appl. Phys. Lett.*, vol. 53, pp. 1027-1029, 1988.
- [18] G. Hasnain, B. F. Levin, C. G. Bethea, R. A. Logan, J. Walker, and R. J. Malik, "GaAs/AlGaAs multiquantum well infrared detector using etched gratings," *Appl. Phys. Lett.*, vol. 54, pp. 2515-2517, 1989.
- [19] L. S. Yu and S. S. Li, "A metal grating coupled bound-to-miniband transition GaAs multiquantum well/superlattice infrared detector," *Appl. Phys. Lett.*, vol. 59, pp. 1332-1334, 1991.
- [20] L. S. Yu, S. S. Li, and Y. H. Wang, "A study of the coupling efficiency versus grating periodicity in a normal incident GaAs/AlGaAs multiquantum well infrared detector," *J. Appl. Phys.*, vol. 72, pp. 2105-2109, 1992.
- [21] W. J. Li, B. D. McCombe, F. A. Chamber, G. P. Devane, J. Ralston, and G. Wicks, "Grating-coupler-induced intersubband transitions in semiconductor multiple quantum wells," *Surf. Sci.*, vol. 228, pp. 164-167, 1990.
- [22] W. J. Li and B. D. McCombe, "Coupling efficiency of metallic gratings for excitation of intersubband transitions in quantum-well structures," *J. Appl. Phys.*, vol. 71, pp. 1038-1040, 1992.
- [23] A. Köck, E. Gornik, G. Abstreiter, G. Böhm, M. Walther, and G. Weimann, "Double wavelength selective GaAs/AlGaAs infrared detector device," *Appl. Phys. Lett.*, vol. 60, pp. 2011-2013, 1992.
- [24] J. Y. Andersson, L. Lundqvist, and Z. F. Paska, "Quantum efficiency enhancement of AlGaAs/GaAs quantum well infrared detectors using a waveguide with a grating coupler," *Appl. Phys. Lett.*, vol. 58, pp. 2264-2266, 1991.

- [25] J. Y. Andersson, L. Lundqvist, and Z. F. Paska, "Near-unity quantum efficiency of AlGaAs/GaAs quantum well infrared detectors using a waveguide with a doubly periodic grating coupler," *Appl. Phys. Lett.*, vol. 59, pp. 857-859, 1991.
- [26] J. Y. Andersson and L. Lundqvist, "Grating-coupled quantum-well infrared detectors: Theory and performance," *J. Appl. Phys.*, vol. 71, pp. 3600-3610, 1992.
- [27] L. Lundqvist, J. Y. Andersson, Z. F. Paska, J. Borglind, and D. Haga, "Efficiency of grating coupled AlGaAs/GaAs quantum well infrared detectors," *Appl. Phys. Lett.*, vol. 63, pp. 3361-3363, 1993.
- [28] B. F. Levine, "Quantum-well infrared photodetectors," *J. Appl. Phys.*, vol. 74, pp. R1-R81, 1993.
- [29] E. Yablonovitch and G. D. Cody, "Intensity enhancement in textured optical sheets for solar cells," *IEEE Trans. Electron Devices*, vol. ED-29, pp. 300-305, 1982.
- [30] R. F. Harrington, "Matrix methods for field problems," *Proc. IEEE*, vol. 55, pp. 136-149, 1967.
- [31] L. S. Yu, Y. H. Wang, S. S. Li, and P. Ho, "Low dark current step-bound-to-miniband transition InGaAs/GaAs/AlGaAs multiquantum-well infrared detector," *Appl. Phys. Lett.*, vol. 60, pp. 992-994, 1992.
- [32] D. D. Coon, R. P. G. Karunasiri, and L. Z. Liu, "Narrow band infrared detection in multiquantum well structures," *Appl. Phys. Lett.*, vol. 47, pp. 289-291, 1985.
- [33] B. F. Levine, K. K. Choi, C. G. Bethea, J. Walker, and R. J. Malik, "New 10 μ m infrared detector using intersubband absorption in resonant tunneling GaAlAs superlattices," *Appl. Phys. Lett.*, vol. 50, pp. 1092-1094, 1987.
- [34] B. F. Levine, C. G. Bethea, G. Hasnain, V. O. Shen, E. Pelve, and P. R. Abbott, "High sensitivity low dark current 10 μ m GaAs quantum well infrared photodetectors," *Appl. Phys. Lett.*, vol. 56, pp. 851-853, 1990.
- [35] S. D. Gunapala, B. F. Levine, D. Ritter, R. Hamm, and M. B. Panish, "InGaAs/InP long wavelength quantum well infrared photodetectors," *Appl. Phys. Lett.*, vol. 58, pp. 2024-2026, 1991.
- [36] F. Stern, "Dispersion of the index of refraction near the absorption edge of semiconductors", *Phys. Rev.*, vol. 133, pp. A1653-1659, 1964.
- [37] F. Stern, "Calculated energy levels and optical absorption in n-type Si accumulation layers at low temperature," *Phys. Rev. Lett.*, vol. 33, pp. 960-963, 1974.

- [38] S. J. Allen, Jr., D. C. Tsui, and B. Vinter, "On the absorption of infrared radiation by electrons in semiconductor inversion layers," *Solid State Commun.*, vol. 20, pp. 425-428, 1976.
- [39] L. C. West and S. J. Eglash, "First observation of an extremely large-dipole infrared transition within the conduction band of a GaAs quantum well," *Appl. Phys. Lett.*, vol. 46, pp. 1156-1158, 1985.
- [40] Z. Ikonić, V. Milanović, D. Tjapkin, "Effective-mass-mismatch-intersubband absorption line broadening in semiconductor quantum wells," *Phys. Rev. B*, vol. 37, pp. 3097-3100, 1988.
- [41] M. Zalužny, "Bound-free intraband absorption line shape in quantum-well structures," *Solid State Commun.* (Britain), vol. 79, pp. 1013-1016, 1991.
- [42] B. F. Levine, R. J. Malik, J. Walker, K. K. Choi, C. G. Bethea, D. A. Kleinman, and J. M. Vandenberg, "Strong 8.2 μm infrared intersubband absorption in doped GaAs/AlAs quantum well waveguides," *Appl. Phys. Lett.*, vol. 50, pp. 273-275, 1987.
- [43] R. Petit, editor, *Electromagnetic Theory of Gratings*, (Spring Verlag Berlin Heidelberg, New York, 1980), pp. 239.
- [44] R. C. Compton, P. C. McPhedran, G. N. Derrick, and L. C. Botten, "Diffraction properties of bandpass grid," *Infrared Phys.*, vol. 23, pp. 239-245, 1983.
- [45] R. C. McPhedran and D. Maystre, "On the theory and solar application of inductive grids," *Appl. Phys.*, vol. 14, pp. 1-20, 1977.
- [46] L. C. Botten, "A new formalism for transmission gratings," *Optica Acta*, vol. 25, pp. 481-499, 1978.
- [47] C. C. Chen, "Scattering by a two-dimensional periodic arrays of conducting plates," *IEEE Trans. Antennas Propagat.*, vol. AP-18, pp. 660-665, 1970.
- [48] B. F. Levine, C. G. Bethea, K. K. Choi, and R. J. Malik, "Tunneling lifetime broadening of the quantum well intersubband photoconductivity spectrum," *Appl. Phys. Lett.*, vol. 53, pp. 231-233, 1988.
- [49] M. O. Manasreh, F. Szmulowicz, D. W. Fisher, K. R. Evans, and C. E. Stutz, "Intersubband infrared absorption in a GaAs/Al_{0.3}Ga_{0.7}As quantum well structure," *Appl. Phys. Lett.*, vol. 57, pp. 1790-1792, 1990.
- [50] Z. Zussman, B. F. Levine, J. M. Kuo, and J. de Jong, "Extended long-wavelength $\lambda = 11\text{-}15\ \mu\text{m}$ GaAs/Al_xGa_{1-x}As quantum-well infrared photodetectors," *J. Appl. Phys.*, vol. 70, pp. 5101-5107, 1991.
- [51] P. K. Cheo, *Fiber Optics and Optoelectronics*, 2nd ed. (Prentice Hall, Englewood Cliffs, New Jersey, 1990), pp. 370.

- [52] Y. H. Wang, S. S. Li, and P. Ho, "Voltage-tunable dual mode operation In-GaAs/InAlAs quantum well infrared photodetector for narrow- and broadband detection at $10\mu\text{m}$," *Appl. Phys. Lett.*, vol. 62, pp. 621-623, 1993.
- [53] S. D. Gunapala, B. F. Levine, L. Pfeiffer, and K. West, "Dependence of the performance of GaAs/AlGaAs quantum well infrared photodetectors on doping and bias," *J. Appl. Phys.*, vol. 69, pp. 6517-6520, 1991.
- [54] K. K. Choi, M. Dutta, P. G. Newman, and M. L. Saunder, " $10\mu\text{m}$ infrared hot-electron transistors," *Appl. Phys. Lett.*, vol. 57, pp. 1348-1350, 1990.
- [55] B. F. Levine, C. G. Bethea, V. O. Shen, and R. J. Malik, "Tunable long wavelength detectors using graded barrier quantum wells grown by electron beam source molecular beam epitaxy," *Appl. Phys. Lett.*, vol. 57, pp. 383-385, 1990.
- [56] K. M. S. V. Bandara, J.-W. Choe, and M. H. Francombe, "GaAs/AlGaAs superlattice miniband detector with $14.5\mu\text{m}$ peak response," *Appl. Phys. Lett.*, vol. 60, pp. 3022-3024, 1992.
- [57] C. G. Bethea, B. F. Levine, V. O. Shen, R. R. Abbott, and S. J. Hseih, " $10\mu\text{m}$ GaAs/AlGaAs multiquantum well scanned array infrared imaging camera," *IEEE Trans. Electron Devices*, vol. ED-38, pp. 1118-1123, 1991.
- [58] R. P. G. Karunasiri and K. L. Wang, "Infrared absorption in parabolic multi-quantum well structures," *Superlatt. Micros.*, vol. 4, pp. 661-663, 1988.
- [59] C. C. Chen, "Transmission through a conducting Screen perforated periodically with apertures," *IEEE Trans. Microwave Theory Tech.*, vol. MTT-18, pp. 627-632, 1970.
- [60] D. Cui, Z. Chen, Y. Zhou, H. Lu, Y. Xie, and G. Yang, "Quantum well infrared detector with grating enhancement," *Infrared Phys.*, vol. 32, pp. 53-56, 1991.
- [61] K. M. S. V. Bandara, D. D. Coon, and Byungsung O, "Exchange interactions in quantum well subbands," *Appl. Phys. Lett.*, vol. 53, pp. 1931-1933, 1988.
- [62] J.-W. Choe, Byungsung O, K. M. S. V. Bandara, and D. D. Coon, "Exchange interaction effects in quantum well infrared detectors and absorbers," *Appl. Phys. Lett.*, vol. 56, pp. 1679-1681, 1990.
- [63] I. Gravé, A. Shakouri, N. Kuze, and A. Yariv, "Voltage-controlled tunable GaAs/AlGaAs multistack quantum well infrared detector," *Appl. Phys. Lett.*, vol. 60, pp. 2362-2364, 1992.
- [64] E. Martinet, F. Luc, E. Rosencher, Ph. Bois, and S. Delaitre, "Electrical tunability of infrared detectors using compositionally asymmetric GaAs/AlGaAs multiquantum wells," *Appl. Phys. Lett.*, vol. 60, pp. 895-897, 1992.

- [65] K. K. Choi, L. Fotiadis, M. Taysing-Lara, and W. Chang, "Infrared absorption and photoconductive gain of quantum well infrared photodetectors," *Appl. Phys. Lett.*, vol. 60, pp. 592-594, 1992.
- [66] L. J. Kozlowski, G. M. William, G. J. Sullivan, C. W. Farley, R. J. Anderson, J. Chen, D. T. Cheung, W. E. Tennant, and R. E. DeWames, "LWIR 128×128 GaAs/AlGaAs multiple quantum well hybrid focal plane array," *IEEE Trans. Electron Devices*, vol. ED-38, pp. 1118-1123, 1991.
- [67] B. F. Levine, S. D. Gunapala, and R. T. Kopf, "Photovoltaic GaAs quantum well infrared detectors at 4.2μm using indirect Al_xGa_{1-x} barriers," *Appl. Phys. Lett.*, vol. 58, pp. 1551-1553, 1991.
- [68] E. Rosencher, E. Martinet, F. Luc. Ph. Bois, and E. Böckenhoff, "Discrepancies between photocurrent and absorption spectroscopies in intersubband photoionization from GaAs/AlGaAs multiquantum wells," *Appl. Phys. Lett.*, vol. 59, pp. 3255-3257, 1991.
- [69] M. J. Kane, M. T. Emeny, N. Apsley, C. R. Whitehouse and D. Lee, "Inter-sub-band absorption in GaAs/AlGaAs single quantum well," *Semicond. Sci. Technol.*, vol. 3, pp. 722-725, 1988.
- [70] Z. Ikonić, V. Milanović, D. Tjapkin, "Resonant second harmonic generation by a semiconductor quantum well in electric field," *IEEE J. Quantum Electron.*, vol. QE-25, pp. 54-59, 1989.
- [71] M. M. Fejer, S. J. B. Yoo, R. L. Byer, A. Harwit, and J. S. Harris, "Observation of extremely large quadratic susceptibility at 9.6-10.8μm in electric-field-biased AlGaAs quantum wells," *Phys. Rev. Lett.*, vol. 62, pp. 1041-1044, 1989.
- [72] J. M. Mooney, F. D. Shepherd, W. S. Ewing, J. E. Murguire, and J. Silverman, "Responsivity nonuniformity limited performance of infrared staring cameras," *Opt. Eng.*, vol. 28, pp. 1151-1161, 1989.
- [73] J. Leo and B. Movaghar, "Intersubband optical absorption in a biased superlattice," *J. Appl. Phys.*, vol. 65, pp. 5019-5023, 1989.
- [74] V. D. Shadrin and F. L. Serzhenko, "The theory of multiple quantum-well GaAs-AlGaAs infrared detectors," *Infrared Phys.*, vol. 33, pp. 345-357, 1992.
- [75] S. R. Andrew and B. A. Miller, "Experimental and theoretical studies of the performance of quantum-well infrared photodetectors," *J. Appl. Phys.*, vol. 70, pp. 993-1003, 1991.
- [76] H. Asai and Y. Kawamura, "Intersubband absorption in high strained In-GaAs/InAlAs multiquantum wells," *Appl. Phys. Lett.*, vol. 56, pp. 746-748, 1990.

- [77] K. Kheng, M. Ramsteiner, H. Schneider, J. D. Ralston, F. Fuchs, and P. Koidl, "Two-color GaAs/(AlGa)As quantum well infrared detector with voltage-tunable spectral sensitivity at 3-5 and 8-12 μ m," *Appl. Phys. Lett.*, vol. 61, pp. 666-668, 1992.
- [78] G. Landgren, S. G. Andersson, J. Y. Andersson, L. Samuelsson, P. Silverberg, and P. Tolkien, "Novel reactor design for large area uniformity of abrupt heterojunction structures," *J. Cryst. Growth.*, vol. 77, pp. 67-72, 1986.
- [79] D. D. Coon and R. P. G. Karunasiri, "New mode of IR detection using quantum wells," *Appl. Phys. Lett.*, vol. 45, pp. 649-651, 1984.
- [80] I. J. Fritz, "Energy levels of finite-depth quantum wells in an electric field," *J. Appl. Phys.*, vol. 61, pp. 2273-2276, 1987.
- [81] K. K. Choi, B. F. Levine, C. G. Bethea, J. Walker, and R. J. Malik, "Photoexcited coherent tunneling in a double-barrier superlattice," *Phys. Rev. Lett.*, vol. 21, pp. 2459-2461, 1987.
- [82] K. K. Choi, L. Fotiadis, M. Taysing-Lara, and W. Chang "High detectivity InGaAs base infrared hot-electron transistor," *Appl. Phys. Lett.*, vol. 59, pp. 3303-3305, 1991.
- [83] Y. J. Mii, R. P. G. Karunasiri, and K. L. Wang, "Electrical and optical properties of GaAs/AlGaAs multiple quantum wells grown on Si substrates," *Appl. Phys. Lett.*, vol. 53, pp. 2050-2052, 1988.
- [84] R. P. G. Karunasiri, J. S. Park, and K. L. Wang, "Si_{1-x}Ge_x/Si multiple quantum well infrared detector," *Appl. Phys. Lett.*, vol. 59, pp. 2588-2590, 1991.
- [85] C. G. Bethea, B. F. Levine, M. T. Asom, R. E. Leibenguth, J. W. Stayt, K. G. Glogovsky, R. A. Morgan, J. D. Blackwell and W. J. Parrish, "Long wavelength infrared 128 \times 128 Al_xGa_{1-x}As/GaAs quantum well infrared camera and imaging system," *IEEE Trans. Electron Devices*, vol. ED-40, pp. 1957-1963, 1993.
- [86] M. J. Kane, M. T. Emeny, N. Apsley, C. R. Whitehouse, and D. Lee, "Inter-subband absorption and infrared modulation in GaAs/AlGaAs single quantum wells," *Superlatt. Micros.*, vol. 5, pp. 587-589, 1989.
- [87] M. J. Kane and N. Apsley, "Waveguide and surface plasmon coupled infrared devices using semiconductor quantum wells," *J. de Physique*, vol. C5, pp. 545-548, 1987.
- [88] Y.-C. Wang and S. S. Li, "A numerical analysis of the double periodic reflection metal grating for QWIP," *J. Appl. Phys.*, vol. 74, pp. 2192-2196, 1993.

- [89] Y.-C. Wang and S. S. Li, "Design of a 2-D square mesh metal grating coupler for a miniband transport GaAs QWIP," *J. Appl. Phys.*, vol. 75, pp. 582-587, 1994.
- [90] C. C. Chen, "Diffraction of electromagnetic waves by a conducting screen perforated periodically with circular holes," *IEEE Trans. Microwave Theory Tech.*, vol. MTT-19, 475-481 (1971).
- [91] N. Amitay and V. Galindo, "The analysis of circular waveguide phased-arrays," *Bell Syst. Tech. J.*, Vol. 47, pp. 1903-1932, 1968.
- [92] N. Marcuvitz, editor, *Waveguide Handbook*, (McGraw-Hill, New York, 1951), pp. 66.
- [93] D. A. B. Miller, D. S. Chemla, T. C. Damen, A. C. Gossard, W. Weigmann, T. H. Wood, and C. A. Burrus, "Effective field dependence of optical absorption near the band-gap of quantum well structures," *Phys. Rev. B*, vol. 32, pp. 1043-1047, 1985.
- [94] S. D. Gunapala, B. F. Levine, and Naresh Chand, "Bound to continuum miniband long wavelength GaAs/Al_xGa_{1-x}As photodetectors," *J. Appl. Phys.*, vol. 70, pp. 305-308, 1991.
- [95] L. C. Chiu, J. S. Smith, S. Margalit, A. Yariv, and A. Y. Cho, "Application of internal photoemission from quantum-well and heterojunction superlattices to infrared photodetectors," *Infrared Phys.*, vol. 23, pp. 93-97, 1983.
- [96] Y. Rajakarunanyake and T. C. McGill, "Intersubband absorption in Si_{1-x}Ge_x/Si superlattices for long wavelength infrared detectors," *J. Vac. Sci. Technol. B*, vol. 8, pp 929-935 (1990).
- [97] H. C. Liu, "Dependence of absorption spectrum and responsivity on the upper state position in quantum well intersubband photodetectors," *J. Appl. Phys.*, vol. 73, 3062-3067, (1993).
- [98] G. Hasnain, B. F. Levine, C. G. Bethea, R. G. Abbott, and S. J. Hsieh, "Measurement of intersubband absorption in multiquantum well structures with monolithically integrated photodetectors," *J. Appl. Phys.*, vol. 67, 4361-4363, (1990).
- [99] A. G. Steele, H. C. Liu, M. Buchanan, and Z. R. Wasilewski, "Importance of the upper state position in the performance of quantum well intersubband infrared detectors," *Appl. Phys. Lett.*, vol. 59, 3625-3627, (1991).
- [100] A. Rose, *Concepts in Photoconductivity and Allied Problems*, (Interscience, New York, 1963).

- [101] G. Hasnain, B. F. Levine, S. Gunapala, and Naresh Chand, "Large photoconductive gain in quantum well infrared photodetectors," *Appl. Phys. Lett.*, vol. 57, pp. 608-610, (1990).
- [102] A. G. Steele, H. C. Liu, M. Buchanan, and Z. R. Wasilewski, "Influence of the number of wells in the performance of multiple quantum well intersubband infrared detectors," *J. Appl. Phys.*, vol. 72, pp. 1062-1-64, 1992.
- [103] S. S. Li, M. Y. Chuang and L. S. Yu, "Current conduction in bound-to-miniband transition III-V multiquantum well/superlattice infrared photodetectors," *Semicond. Sci. Technol.*, vol. 8, pp. 406-411, 1993.
- [104] A. Kastalsky, T. Duffield, S. J. Allen, and J. Harbison, "Photovoltaic detection of infrared light in GaAs/AlGaAs superlattice," *Appl. Phys. Lett.*, vol. 52, 1320-1322, (1988).
- [105] C. S. Wu, C. P. Wen, R. N. Sato, M. Hu, C. W. Tu, J. Zhang, L. D. Flesner, Le Pham, and D. S. Nayer, "Novel GaAs/AlGaAs multiquantum-well Schottky-junction device and its photovoltaic LWIR detection," *IEEE Trans. Electron. Devices*, vol. ED-39, 234-241, 1992.
- [106] D. D. Coon, R. P. G. Karunasiri and H. C. Liu, "Fast response quantum well photodetectors," *J. Appl. Phys.*, vol. 60, 2636-2638, 1986.
- [107] T. Taimir, editor, *Guided Wave Optoelectronics*, (Springer-Verlag Berlin Heidelberg, New York, 1988), pp. 43.
- [108] M. A. Fromowitz, "Refractive index of $\text{Ga}_{1-x}\text{Al}_x\text{As}$," *Solid State Commun.*, vol. 15, pp. 59-63, 1974.
- [109] J. Zorootchi and J. K. Butler, "Refractive index of n-type gallium arsenide," *J. Appl. Phys.*, vol. 44, pp. 3697-3699, 1973.

APPENDIX A
COMPLETE FORM OF INNER PRODUCT OF
FLOQUET MODES AND WAVEGUIDE MODES

(i) For the case of $m \neq 0$

$$C_{pq1}^{mn1} = -G \left(\frac{1}{(k \sin \theta_{pq})^2 - (\frac{x'_{mn}}{a})^2} \right) \frac{\sqrt{2\pi} x'_{mn} j^{m-1}}{J_m(x'_{mn}) \sqrt{(x'_{mn})^2 - m^2}} \begin{Bmatrix} \cos m \phi_{pq} \\ \sin m \phi_{pq} \end{Bmatrix} \\ \left\{ \frac{x'_{mn}}{a} J_m(x'_{mn}) [J_{m+1}(k \sin \theta_{pq} a) + J_{m-1}(k \sin \theta_{pq} a)] \right\} \quad (A.1)$$

$$C_{pq2}^{mn1} = -G \left(\frac{1}{(k \sin \theta_{pq})^2 - (\frac{x'_{mn}}{a})^2} \right) \frac{\sqrt{2\pi} x'_{mn} j^{m-1}}{\sqrt{(x'_{mn})^2 - m^2}} \begin{Bmatrix} \sin m \phi_{pq} \\ -\cos m \phi_{pq} \end{Bmatrix} \\ \left\{ \frac{x'_{mn}}{a} [J_{m+1}(k \sin \theta_{pq} a) - J_{m-1}(k \sin \theta_{pq} a)] - k \sin \theta_{pq} J_m(k \sin \theta_{pq} a) \frac{2m}{x'_{mn}} \right\} \quad (A.2)$$

$$C_{pq2}^{mn2} = G \left(\frac{1}{(k \sin \theta_{pq})^2 - (\frac{x'_{mn}}{a})^2} \right) \frac{\sqrt{2\pi} j^{m-1}}{J_{m-1}(x_{mn})} \begin{Bmatrix} \cos m \phi_{pq} \\ \sin m \phi_{pq} \end{Bmatrix} \\ k \sin \theta_{pq} \{ J_m(k \sin \theta_{pq} a) [J_{m-1}(x_{mn}) - J_{m+1}(x_{mn})] \} \quad (A.3)$$

$$C_{pq1}^{mn2} = 0 \quad (A.4)$$

where G is the normalized factor as given in Eq. (2).

(ii) For the case of $m = 0$

$$C_{pq1}^{0n1} = G \left(\frac{1}{(k \sin \theta_{pq})^2 - (\frac{x'_{0n}}{a})^2} \right) \frac{2\sqrt{\pi} j}{J_0(x'_{0n})} \\ \left[\frac{x'_{0n}}{a} J_0(x'_{0n}) J_1(k \sin \theta_{pq} a) - k \sin \theta_{pq} J_0(k \sin \theta_{pq} a) J_1(x'_{0n}) \right] \quad (A.5)$$

$$C_{pq1}^{0n2} = C_{pq2}^{0n1} = 0 \quad (\text{A.6})$$

$$C_{pq2}^{0n2} = G \left(\frac{1}{(k \sin \theta_{pq})^2 - \left(\frac{x_{0n}}{a} \right)^2} \right) 2\sqrt{\pi} j [k \sin \theta_{pq} J_0(k \sin \theta_{pq} a)] \quad (\text{A.7})$$

BIOGRAPHICAL SKETCH

Yeong-Cheng Wang was born in Tainan, Taiwan, R.O.C., on May 10, 1960. He received the B.S. degree in the Department of Civil Engineering and M.S. degree in the Graduate Institute of Electrical Engineering from National Taiwan University in 1984 and 1989, respectively.

From July 1984 to May 1986 he fulfilled his military service as a platoon commander in Corps of Engineering, Chinese Army. In that period, he gained lots of experiences in building construction. From June 1986 to August 1987, he worked in the area of telecommunication and IBM PC hardware design. From September 1987 to June 1989 he was a research assistant in the Microwave Technology Laboratory at National Taiwan University. His research topic was on the applications of coupled-mode theory for parallel waveguide system. After graduating from the university, he became a lecturer in the Oriental Institute of Technology from August 1989 to July 1990.

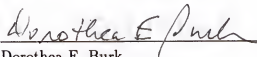
Since August 1990 he has been working toward the Ph.D. degree in the Department of Electrical Engineering in the University of Florida. From August 1991 to April 1994 he was a research assistant in the semiconductor material and device characterization laboratory at the University of Florida. His research topic is on the development of high efficiency two-dimensional grating coupler for multiquantum well detectors.

I certify that I have read this study and that in my opinion it conforms to acceptable standards of scholarly presentation and is fully adequate, in scope and quality, as a dissertation for the degree of Doctor of Philosophy.



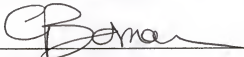
Sheng S. Li, Chairman
Professor of Electrical Engineering

I certify that I have read this study and that in my opinion it conforms to acceptable standards of scholarly presentation and is fully adequate, in scope and quality, as a dissertation for the degree of Doctor of Philosophy.



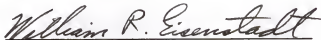
Dorothea E. Burk
Professor of Electrical Engineering

I certify that I have read this study and that in my opinion it conforms to acceptable standards of scholarly presentation and is fully adequate, in scope and quality, as a dissertation for the degree of Doctor of Philosophy.



Gijs Bosman
Professor of Electrical Engineering

I certify that I have read this study and that in my opinion it conforms to acceptable standards of scholarly presentation and is fully adequate, in scope and quality, as a dissertation for the degree of Doctor of Philosophy.



William R. Eisenstadt
Associate Professor of Electrical
Engineering

I certify that I have read this study and that in my opinion it conforms to acceptable standards of scholarly presentation and is fully adequate, in scope and quality, as a dissertation for the degree of Doctor of Philosophy.



Chen-Chi Hsu
Professor of Aerospace Engineering,
Mechanics & Engineering Science

This dissertation was submitted to the Graduate Faculty of the College of Engineering and to the Graduate School and was accepted as partial fulfillment of the requirements for the degree of Doctor of Philosophy.

April 1994



Winfred M. Phillips
Dean, College of Engineering

Karen A. Holbrook
Dean, Graduate School